Delft University of Technology

Elongated particles in fluidized beds
From lab-scale experiments to constitutive models

Mahajan, Vinay

DOI
10.4233/uuid:7760f5ad-958e-4f18-8a1c-d35ae63e9c44

Publication date
2019

Document Version
Final published version

Citation (APA)
Mahajan, V. (2019). *Elongated particles in fluidized beds: From lab-scale experiments to constitutive models*. [Dissertation (TU Delft), Delft University of Technology]. https://doi.org/10.4233/uuid:7760f5ad-958e-4f18-8a1c-d35ae63e9c44

Important note
To cite this publication, please use the final published version (if applicable).
Please check the document version above.

Copyright
Other than for strictly personal use, it is not permitted to download, forward or distribute the text or part of it, without the consent of the author(s) and/or copyright holder(s), unless the work is under an open content license such as Creative Commons.

Takedown policy
Please contact us and provide details if you believe this document breaches copyrights.
We will remove access to the work immediately and investigate your claim.

This work is downloaded from Delft University of Technology.
For technical reasons the number of authors shown on this cover page is limited to a maximum of 10.

Elongated particles in fluidized beds

From lab-scale experiments to constitutive models

Elongated particles in fluidized beds

From lab-scale experiments to constitutive models

Dissertation

for the purpose of obtaining the degree of doctor
at Delft University of Technology
by the authority of the Rector Magnificus, prof.dr.ir. T.H.J.J. van der Hagen,
chair of the Board for Doctorates
to be defended publicly on
Tuesday 29 October 2019 at 12:30 hour

by

Vinay Vilas Mahajan

Master of Science in Process Engineering, Eindhoven University of Technology,
the Netherlands

born in Nagpur, India

This dissertation has been approved by the

Promotor: Prof. dr. ir. J. T. Padding
Copromotor: Dr. ir. B. Eral

Composition of the doctoral committee:

Rector Magnificus,	Chairperson
Prof. dr. ir. J. T. Padding	Delft University of Technology
Dr. ir. B. Eral	Delft University of Technology
Independent members:	
assoz. univ.-prof. dr. S. Pirker	Johannes Kepler University Linz
Prof. dr. D. van der Meer	University of Twente
Prof. dr. A. Thornton	University of Twente
Prof. dr. ir. N. G. Deen	Eindhoven University of Technology
Prof. dr. ir. J. R. van Ommen	Delft University of Technology
Prof. dr. ir. W. de Jong	Delft University of Technology, reserve member

Keywords: CFD-DEM, non-spherical particles, fluidized beds, experiments, constitutive model

Printed by: Ridderprint BV

Cover designed by: V. Rajurkar

Copyright © 2019 by V.V. Mahajan
ISBN 978-94-6375-618-1

An electronic version of this dissertation is available at

`http://repository.tudelft.nl/`.

To my parents and sister, for their profound love

Summary

Gas-solid fluidized beds are widely used in various industries due to their favourable mixing, and mass and heat transfer characteristics. Fluid catalytic cracking, polymerization, drying, and granulation are a few examples of their applications. In recent years, there has been increased application of fluidized beds in biomass gasification and clean energy production. Fluidization has been extensively studied, experimentally, theoretically and numerically, in the past. However, most of these studies focused on spherical particles while in practice granules are rarely spherical. Particle shape can have a significant effect on fluidization characteristics. It is therefore important to study the effect of particle shape on fluidization behavior in detail.

One of the main reasons we still do not completely understand the fluidization phenomenon is because of complex hydrodynamic interactions and its large separation of scales. Industrial fluidized bed reactors of tens of meters in diameter can have hydrodynamic scales varying from micrometers to meters. Experimental setups of such large size are extremely expensive and therefore not practical. On the other hand, theoretical and empirical correlations are not accurate for scale-up and are rarely available for non-spherical particle shapes. Because of this, we need a different approach. One that takes advantage of experimental measurements and numerical simulations. The tasks are divided into three parts based on scales, each focusing on a particular aspect : DNS (direct numerical simulation), CFD-DEM (computational fluid dynamics - discrete element model) and TFM (two fluid model) or MP-PIC (multi-phase - particle in cell). In this thesis, the focus is on CFD-DEM modelling, a 'bridge' that connects the DNS and TFM/MP-PIC models.

First, the fluidized bed is experimentally studied. The fluidization of spherocylindrical (rod-like) Geldart D particles of aspect ratio 4 is investigated. Pressure drop and optical measurement methods (Digital Image Analysis, Particle Image Velocimetry, Particle Tracking Velocimetry) are employed to measure bed height, particle orientation, particle circulation, stacking, and coordination number. The commonly used empirical and theoretical correlations to determine the pressure drop across a bed of non-spherical particles are compared to experiments. Experimental observations and measurements show that rod-like particles are prone to interlocking and channeling behavior. Well above the minimum fluidization velocity, vigorous bubbling fluidization is observed, with groups of interlocked particles moving upwards, breaking up, being thrown high in the freeboard region and slowly raining down as dispersed phase. At high fluidization velocity, a circulation pattern develops with particles moving up through the center and down at the walls. Particles tend to orient themselves along the flow direction.

Numerical models are used to study non-spherical fluidization behaviour in detail. A crucial step in the development of the numerical model is a detailed validation with experimental data. The validated model can then be used with confidence for further understanding non-spherical fluidization. The results obtained from CFD-DEM modelling are compared with detailed experiments. The numerical modelling strategy for rod-like particles is presented, including the DEM contact detection algorithm and an accurate voidage calculation algorithm. The non-spherical single particle drag model of Hölzer and Sommerfeld (2008) is compared with a DNS drag model for spherocylindrical particles developed in-house. Two new voidage correction models are proposed and results are compared with the Di Felice (1994) model. The pressure drop, bed height, particle orientation, particle circulation, stacking of particles and coordination number obtained from simulations are compared with experiments. Similar to experiments, simulations show that rod-like particles are prone to interlocking behaviour. The importance of hydrodynamic torque and multi-particle drag in CFD-DEM modelling of non-spherical particles is demonstrated through these results.

To be able to simulate industrial scale fluidized beds with billions of particles, coarse grained models (TFM or MP-PIC) are used. These models do not explicitly solve for particle collisions, thereby bypassing the most expensive step. Instead, these models require particle stress closures to account for particle-particle interactions. Closures based on kinetic theory are specifically developed for spherical particles. Additionally, the particles studied in this work are characterized by high particle Stokes and Reynolds numbers. The rheology of suspensions of such high-inertia (or granular) non-spherical particles is rarely investigated. The validated CFD-DEM model can now be used to understand the rheology and subsequently develop stress closures.

We subject the inertial rod-like particles of aspect ratio 4 to shear flow and initially investigate the effect of surrounding fluid on particle-particle interaction. In particular, the effect of fluid medium (air, water) against dry frictionless granular simulations on the developed stresses is assessed. CFD-DEM simulations are performed for a periodic shear box for a range of shear rates and volume fractions of particles. The dependence of rheological properties like shear stress, normal stress difference, pressure and relative viscosity on volume fraction, shear rate, granular temperature and the particle orientation are discussed. These results provide insight into the macroscopic rheology of suspensions of rods and demonstrate that the effect of particle shape and surrounding fluid cannot be completely ignored. Air as a fluid medium shows similar scaling as compared to dry granular simulations, but the stress values are generally lower. A drastic change in both scaling and values for water as fluid medium is observed. In all cases, the rods show strong alignment in the direction of shear.

In the last part of this work, the rheology of the same high-inertia elongated particles is investigated as a function of particle friction as well as shear rate and volume fraction. The rheology of rod-like particle flows in the dense regime is found to depend on friction coefficient as well as a critical volume fraction. In the dilute regime, the rheology is found to depend largely on the granular temperature of particles.

Finally, constitutive equations for collisional stress and collisional pressure, applicable to a large range of volume fractions and shear rates are proposed. These constitutive relations for rod-like particles have the same form as for spheres but with modified parameters. The methodology for the development of accurate collisional stress closure is demonstrated. These closures are specific to particle shape and micro-mechanical properties, while also taking into account the effect of the surrounding fluid.

Samenvatting

Gas-vast gefluïdiseerde bedden worden veel gebruikt in de industrie vanwege hun goede menggedrag en goede massa- en warmteoverdrachtskarakteristieken. Fluid catalytic cracking, polymerisatie, drogen en granulatie zijn een paar voorbeelden van de toepassingen. In recente jaren worden wervelbedden steeds meer toegepast in biomassa gasificatie en schone energieproductie. Fluïdisatie is in het verleden intensief bestudeerd, zowel experimenteel, theoretisch als numeriek. De meeste van deze studies richtten zich echter op ronde deeltjes, terwijl in de praktijk de deeltjes zelden rond zijn. Deeltjesvorm kan een significant effect hebben op fluïdisatiekarakteristieken. Het is daarom belangrijk om het effect van deeltjesvorm op het fluïdisatiegedrag in detail te bestuderen.

Een van de belangrijkste redenen waarom we de fluïdisatieverschijnselen nog steeds niet volledig begrijpen, is vanwege de complexe hydrodynamische interacties en de grote scheiding van schalen. Industriële wervelbedreactoren met een diameter van tientallen meters kunnen hydrodynamische schalen hebben die variëren van micrometers tot meters. Experimentele opstellingen van zo'n groot formaat zijn extreem duur en daarom niet praktisch. Aan de andere kant zijn theoretische en empirische correlaties niet nauwkeurig voor opschaling en zijn ze zelden beschikbaar voor niet-ronde deeltjesvormen. Daarom hebben we een andere aanpak nodig. E'en die profiteert van experimentele metingen en numerieke simulaties. De taken zijn verdeeld in drie delen op basis van schaal, elk gericht op een specifiek aspect: DNS (directe numerieke simulaties), CFD-DEM (computational fluid dynamics - discreet element model) en TFM (two fluid model) of MP-PIC (multi-phase - particle in cell). In dit proefschrift ligt de nadruk op CFD-DEM-modellering, een 'brug' die de DNS- en TFM / MP-PIC-modellen verbindt.

Eerst is het wervelbed experimenteel bestudeerd. De fluïdisatie van sferocylindrische (staafachtige) Geldart D-deeltjes met lengte-diameterverhouding 4 is onderzocht. Drukval en optische meetmethoden (Digital Image Analysis, Particle Image Velocimetry, Particle Tracking Velocimetry) zijn gebruikt om bedhoogte, deeltjesoriëntatie, deeltjescirculatie, deeltjespakking en -coördinatiegetal te meten. De algemeen gebruikte empirische en theoretische correlaties om de drukval over een bed van niet-ronde deeltjes te bepalen, zijn vergeleken met experimenten. Experimentele observaties en metingen tonen aan dat staafachtige deeltjes vatbaar zijn voor entanglement en vorming van kanalen. Ruim boven de minimale fluïdisatiesnelheid is krachtige fluïdisatie waargenomen, met groepen van onderling geëntanglede deeltjes die naar boven bewegen, uiteenvallen, hoog boven het bed worden gegooid en langzaam naar beneden regenen als een gedispergeerde fase. Bij hoge fluïdisatiesnelheid ontwikkelt zich een circulatiepatroon met deeltjes die door het midden omhoog en langs de wanden naar beneden bewegen. Deeltjes hebben de neiging zich in de stroomrichting te oriënteren.

Numerieke modellen zijn gebruikt om niet-bolvormig fluïdisatiegedrag in detail te bestuderen. Een cruciale stap in de ontwikkeling van het numerieke model is een gedetailleerde validatie met experimentele data. Het gevalideerde model kan vervolgens met vertrouwen worden gebruikt voor een beter begrip van niet-ronde fluïdisatie. De resultaten verkregen uit CFD-DEM-simulaties zijn vergeleken met gedetailleerde experimenten. De numerieke modelleringsstrategie voor staafachtige deeltjes is gepresenteerd, inclusief het DEM-contactdetectie-algoritme en een nauwkeurig algoritme voor het berekenen van de lege ruimte. Het niet-ronde wrijvings-model met één deeltje van Hölzer en Sommerfeld (2008) is vergeleken met een intern ontwikkeld wrijvingsmodel voor sferocylindrische deeltjes. Twee nieuwe correctiemodellen voor het effect van naburige deeltjes zijn voorgesteld en de resultaten zijn vergeleken met het Di Felice (1994) model. De drukval, bedhoogte, deeltjesoriëntatie, deeltjescirculatie, deeltjespakking en coördinatiegetal verkregen uit simulaties zijn vergeleken met experimenten. Vergelijkbaar met experimenten, tonen simulaties aan dat staafachtige deeltjes vatbaar zijn voor entanglement gedrag. Het belang van hydrodynamisch koppel en wrijving door naburige deeltjes bij CFD-DEM-modellering van niet-ronde deeltjes is door deze resultaten aangetoond.

Om gefluïdiseerde bedden op industriële schaal met miljarden deeltjes te kunnen simuleren, worden grofkorrelige modellen (TFM of MP-PIC) gebruikt. Deze modellen lossen niet expliciet de deeltjesbotsingen op en omzeilen daarmee de duurste stap. In plaats daarvan vereisen deze modellen sluitingsrelateis voor de deeltjesstress om rekening te houden met de interacties tussen de deeltjes. Sluitingsrelaties op basis van kinetische theorie zijn specifiek ontwikkeld voor bolvormige deeltjes. Bovendien worden de in dit werk bestudeerde deeltjes gekenmerkt door hoge Stokes en Reynolds-getallen. De reologie van suspensies van dergelijke niet-bolvormige deeltjes met een hoge inertia (granulaire deeltjes) wordt zelden onderzocht. Het gevalideerde CFD-DEM-model kan nu worden gebruikt om de reologie te begrijpen en vervolgens stress-sluitingsrelaties te ontwikkelen.

We onderwerpen de staafachtige deeltjes met lengte-diameterverhouding 4 aan een afschuifstroming en onderzoeken in eerste instantie het effect van het omringende gas of vloeistof op de interactie tussen de deeltjes. In het bijzonder is het effect van het medium (lucht, water) op de ontwikkelde deeltjes-stress beoordeeld. CFD-DEM-simulaties zijn uitgevoerd voor een periodiek systeeem voor een reeks afschuifsnelheden en volumefracties van deeltjes. De afhankelijkheid van reologische eigenschappen, zoals schuifspanning, normaal spanningsverschil, druk en relatieve viscositeit van volumefractie, afschuifsnelheid, granulaire temperatuur en de deeltjesoriëntatie zijn besproken. Deze resultaten geven inzicht in de macroscopische reologie van suspensies van staven en tonen aan dat het effect van deeltjesvorm en omringende vloeistof niet volledig kan worden genegeerd. Lucht als medium vertoont vergelijkbare schaling in vergelijking met droge granulaire simulaties, maar de stresswaarden zijn over het algemeen lager. Een drastische verandering in zowel schaling als waarden zijn waargenomen voor water als medium. In alle gevallen vertonen de staven een sterke uitlijning in de richting van afschuiving.

In het laatste deel van dit werk is de reologie van dezelfde staafvormige deeltjes onderzocht als functie van de deeltjeswrijving evenals afschuifsnelheid en volumefractie. De reologie van staafachtige deeltjesstromen in het dichte regime blijkt afhankelijk te zijn van de wrijvingscoëfficiënt evenals een kritische volumefractie. In het verdunde regime blijkt de reologie grotendeels afhankelijk te zijn van de granulaire temperatuur van de deeltjes.

Tenslotte zijn constitutieve vergelijkingen voor botsings-stress en botsings-druk voorgesteld, toepasbaar op een groot aantal volumefracties en afschuifsnelheden. Deze constitutieve relaties voor staafachtige deeltjes hebben dezelfde vorm als voor bollen maar met gemodificeerde parameters. De methodiek voor de ontwikkeling van nauwkeurige sluitingsrelaties van botsings-stress is aangetoond. Deze sluitingen zijn specifiek voor de deeltjesvorm en micromechanische eigenschappen, maar houden ook rekening met het effect van het omringende medium.

Contents

Summary **vii**

Samenvatting **xi**

List of Figures **xix**

List of Tables **xxiii**

1 Introduction **1**
- 1.1 Fluidized beds 1
- 1.2 Research objective 3
- 1.3 Thesis outline 4

2 Experimental Measurements **5**
- 2.1 Introduction 5
- 2.2 Experimental setup 6
  - 2.2.1 Pressure drop measurements 9
  - 2.2.2 Digital Image Analysis 12
  - 2.2.3 Particle Image Velocimetry 15
  - 2.2.4 Particle Tracking Velocimetry 21
- 2.3 Results and discussion 22
  - 2.3.1 Fluidization regimes 22
  - 2.3.2 Pressure drop 24
  - 2.3.3 Bed height 25
  - 2.3.4 Spherical particles 26
  - 2.3.5 Pressure drop correlations 27
  - 2.3.6 Pressure drop Fourier analysis 28

2.3.7 Void fraction and mass flux 30
2.3.8 Particle orientation 34
2.3.9 Particle coalignment 35
2.3.10 Particle coordination number 36
2.4 Conclusions and outlook 38

3 CFD-DEM Model 41
3.1 Introduction 41
3.2 Model framework 43
3.3 Discrete Element Method 43
3.3.1 Contact model 44
3.3.2 Contact parameters 48
3.3.3 Neighbour list 52
3.4 Computational Fluid Dynamics 54
3.4.1 Flow solver 54
3.5 Gas-particle coupling 54
3.5.1 Single particle drag models 55
3.5.2 Voidage correction models 57
3.5.3 Void fraction calculation 60

4 Model Validation 63
4.1 Introduction 63
4.2 Simulation setup 64
4.3 Results and discussion 65
4.3.1 Fluidization behaviour 65
4.3.2 Pressure drop and bed height 66
4.3.3 Mass flux 70
4.3.4 Particle orientation 71
4.3.5 Particle coalignment 75
4.3.6 Particle coordination number 75
4.4 Conclusions and outlook 79

5 Rheology of inertial rods: effect of fluid medium 81
5.1 Introduction 81
5.2 Model framework 85
5.3 Stress measurements 85
5.4 Model verification 90
5.5 Results and discussion 92
5.5.1 Granular temperature and pressure 93
5.5.2 Collisional and streaming shear stress 97

5.5.3 Apparent friction and viscosity 100
5.5.4 Normal stress 105
5.5.5 Flow alignment angle 106
5.6 Conclusions and outlook 109

6 Constitutive models for collisional stress: effect of particle friction 111
6.1 Introduction 111
6.2 Simulation setup 114
6.3 Results and discussion 116
6.3.1 Granular temperature and pressure 116
6.3.2 Collisional stress 118
6.3.3 Formulation of constitutive equations 119
6.4 Conclusions and outlook 128

7 Conclusion and outlook 131

References 137

List of Publications 149

Acknowledgements 151

Curriculum Vitae 153

List of Figures

1.1 Biomass pellets used in fluidized bed 2
1.2 Multiscale modelling scheme 3
2.1 Representation of the experimental set-ups. 7
2.2 Geometry of the spherocylinderical particles 8
2.3 Demonstration of the bed height detection algorithm 12
2.4 DIA procedure for orientation detection 13
2.5 Algorithm for detection of particle orientation 14
2.6 Average velocity profile from PIV 16
2.7 Relative deviation from mean velocity 16
2.8 Demonstration of the void fraction calculation 18
2.9 Correlation of 2D and 3D solid volume fraction 19
2.10 Demonstration of the void fraction calculation 20
2.11 An example of PTV procedure 21
2.12 Examples of the different fluidization regimes observed in the large bed . . 23
2.13 Measured pressure drop and bed height 24
2.14 Determination of the minimum fluidization velocity (U_{mf}). 25
2.15 Normalized pressure drop and bed expansion 26
2.16 Pressure drop spherical particles 27
2.17 Relative error of all pressure drop correlations 28
2.18 Power spectrum of pressure drop 29
2.19 Particle velocity and mass flux results from experiments 31
2.20 Mass flux profiles at different flow rates 32
2.21 Mass flux profiles at different flow rates 33
2.22 Probability Density Function (PDF) of the particle orientation 34
2.23 An example of particle coalignment 35
2.24 Spatial autocorrelation results for the large bed 36

2.25 Average particle coordination number 37
3.1 A schematic representation of two particles in contact. 46
3.2 Particle-plate collision experiment 50
3.3 Measured coefficients of restitution for different angles 51
3.4 The setup used for determination of the static coefficient of friction. 51
3.5 Determination of the coefficient of friction 52
3.6 Multi-sphere neighbourlist building method 53
3.7 Single particle drag coefficient as a function of Reynolds number 56
3.8 Voidage correction factor as a function of void fraction and Reynolds number 59
3.9 A comparison of drag coefficients for different drag models 60
3.10 Example of volume fraction calculation 61
4.1 Schematic representation of setup 64
4.2 A simulation snapshot of fluidized bed 66
4.3 Comparison of the pressure drop 67
4.4 Comparison of the pressure drop 68
4.5 Comparison of the bed height 68
4.6 Comparison of the bed height 69
4.7 Particle velocity and mass flux 70
4.8 Particle velocity and mass flux 72
4.9 Probability Density Function (PDF) of the particle orientation 73
4.10 Probability Density Function (PDF) of the particle orientation 74
4.11 Spatial autocorrelation of the orientation 76
4.12 An example snapshot of particle coordination number 77
4.13 Average particle coordination number versus average vertical velocity . . . 78
4.14 Average particle coordination number versus average vertical velocity . . . 78
5.1 Snapshot of simulation setup 86
5.2 Timestep δt_p versus coefficient of restitution 87
5.3 Particle granular temperature and pressure (sphere) 91
5.4 Particle collisional and streaming stress (sphere) 92
5.5 Particle granular temperature and pressure (dry) 94
5.6 Particle granular temperature and pressure (air) 95
5.7 Particle granular temperature and pressure (water) 96
5.8 Particle collisional and streaming stress 98
5.9 Particle collisional and streaming stress 99
5.10 Particle collisional and streaming stress 100
5.11 Apparent friction coefficient μ_s and total suspension viscosity η_s 102
5.12 Apparent friction coefficient μ_s and total suspension viscosity η_s 103
5.13 Apparent friction coefficient μ_s and total suspension viscosity η_s 104
5.14 Particle normal stress ratios 107

5.15 Steady state flow alignment angle 108
5.16 Configuration of particles at steady state 108
6.1 Probability distribution function (PDF) of shear rate 115
6.2 Granular temperature and collisional pressure 116
6.3 Dimensionless pressure for different coefficient of friction 118
6.4 Collisional stress as a function of solids volume fraction 118
6.5 Collisional stress for different coefficient of friction 119
6.6 Fit for scaled pressure versus scaled shear rate 121
6.7 Fit for apparent friction coefficient versus inertial number 121
6.8 Dimensionless collisional shear viscosity versus volume fractions 123
6.9 Fit for collisional viscosity 123
6.10 Fit for scaled dimensionless granular temperature 124
6.11 Collisional stress closure prediction 126
6.12 Particle orientation for different coefficient of friction 127
7.1 The research road-map 131

List of Tables

2.1 Dimensions of the set-up and particles 8
2.2 Correlations used to compare with the acquired pressure drop data. 9
2.3 Parameters for the Reichelt and Allen equations 11
2.4 Coefficient of determination for the pressure drop correlations. 30

3.1 Review of DEM contact detection methods. 45
3.2 Equations for the contact model. 48
3.3 Expressions describing the contact parameters 49
3.4 The coefficients for the Sanjeevi drag correlation 56
3.5 Expressions of drag force used for voidage correction. 58

4.1 Simulation parameters. 65

5.1 Range of dimensionless numbers for the simulations in this work. 84
5.2 Simulation parameters. 88

6.1 Simulation parameters. 115

Chapter 1

Introduction

1.1 Fluidized beds

Gas-solid fluidized beds are widely employed in various industries due to their favourable mixing, mass and heat transfer characteristics. Fluid catalytic cracking, polymerization, drying and granulation are a few examples of their applications. In recent years, there has been increased application of fluidized beds in biomass gasification and clean energy production. Therefore, understanding of complex dense gas-solid flows is important. At present, the design and scale-up of fluidized bed equipment is still mostly a fully empirical process, due to our limited insight into the fundamentals of dense gas-particle flows (Wachem and Almstedt, 2003) and high costs involved in industrial scale experiments.

The main obstacle for a fundamental understanding is the large separation of relevant scales in such systems: the largest flow stuctures can be of the order of meters, yet these structures are directly influenced by details of the particle-particle collisions, particle-wall collisions and particle-gas interactions which take place on the scale of millimeters or even micrometers (Li and Kuipers, 2003). This makes it extremely difficult and challenging to predict the nature of the large-scale heterogeneous structures which play a crucial role in the mass and heat exchange rates in the fluidized bed equipment - in other words, they dictate the overall equipment performance.

Consequently, experimental, theoretical and numerical studies have been used to describe the properties of fluidized beds (Deen et al., 2007; Goldschmidt et al., 2003; Jong et al., 2012). However, almost all research has been conducted using nearly spherical particles because of their geometrical simplicity. In industry, particles are rarely perfectly spherical. An important example is the production of hydrogen and syngas from biomass in fluidized bed gasifiers. The biomass is milled and often processed into pellets before being fed to the gasifier, resulting in elongated particles of aspect ratio three to five and occasionally upto 12, as shown in Figure 1.1.

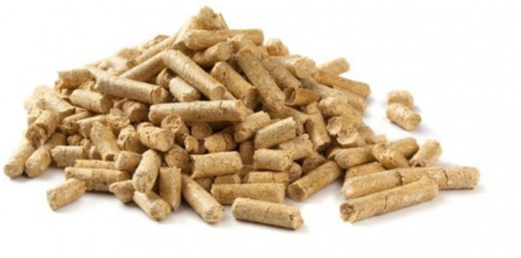

Figure 1.1: Biomass pellets used in fluidized bed gasifier (Indiamart, 2019).

The dynamics of such non-spherical particles can be very different and more complex as compared to spherical particles. These particles experience anisotropic drag (Zastawny et al., 2012; Hölzer and Sommerfeld, 2008; Zhou et al., 2011a) and anisotropic collisions, both of which depend on local spatial distribution and degree of alignment of neighbouring particles and the proximity of internal or external walls. Knowledge about the influence of particle shape is therefore essential, for example, for reactor design and optimization.

Contrary to industrial scale experiments, computer models are inexpensive and can aid the design process of fluidized bed equipment. Given the limited computing resources and the number of (millimeter-sized) particles in a 10 meter high reactor O(10^{10}), it is clear that one has to resort to coarse-grained models, in which the exchange of mass, momentum and heat between the phases is modelled in an effective way.

Figure 1.2 shows a graphical representation of the modelling strategy for an industrial scale fluidized bed containing elongated particles. In the direct numerical simulation (DNS) model, the gas flow is solved on a grid much smaller than the size of the particles, so the flow around and between the particles is fully resolved. It does not rely on any closures for the exchange of mass, momentum or energy between the solid and the gas phase. In the discrete particle model (DPM), the gas flow is solved on a grid larger than the size of the particles; particle-gas interactions are modelled in an effective way, via closures for the translational and rotational drag forces. The particle-particle and particle-wall collisions are treated by a deterministic contact model. The continuum particle model (CPM), recently developed by Verma and Padding, is similar to the DPM model, only now the particle collisions are treated implicitly, with forces and torques de-

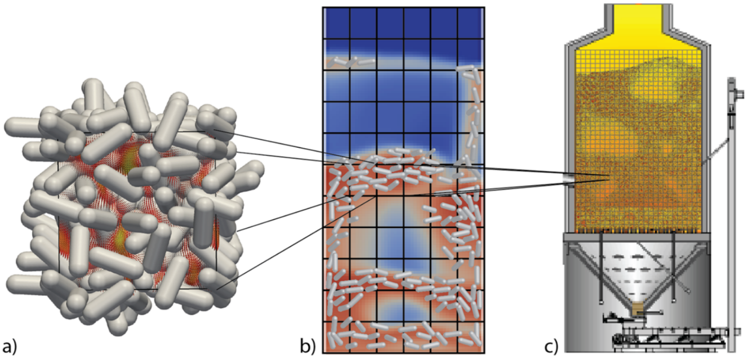

Figure 1.2: Graphic representation of the multiscale modelling scheme for an industrial scale fluidized bed containing elongated particles. The three levels of description of the gas-solid flow are : a) The direct numerical simulation (DNS) model, b) the discrete particle model (DPM) and c) The continuum particle model (CPM).

rived from particle stresses which depend on the translational and orientational particle distribution and velocities, allowing for simulation of large system sizes.

1.2 Research objective

In the current work, we make a first step by focusing on multiscale modelling of momentum transfer in dense fluidized systems containing elongated axisymmetric particles (simplified shape compared to particles shown in Figure 1.1). Such particles are relatively simple, yet many of the fundamental problems linked to anisotropic drag and collisions already appear. The main goals of this work are :

- To present a CFD-DEM model for accurate modelling of spherocylinder particles in fluidized beds : use of an accurate particle collision detection algorithm, drag correlation and volume fraction calculation technique.
- To study lab scale experiments : use of pressure sensors, particle image velocimetry, particle tracking velocimetry and digital image analysis in a quasi-2D fluidized bed to understand the macro and micro-scale behaviour.
- To compare simulations one to one with experiments : validate the drag relations obtained from the DNS simulations and assess the ability of the CFD-DEM model to predict the formation of heterogeneous structures and voids.
- To determine a functional description of the particle stress tensor under relevant conditions of volume fraction and rate of deformation : compare with kinetic the-

ory for spherical particles and propose new constitutive equations for elongated particles while accounting for the effect of interstitial fluid.

1.3 Thesis outline

The thesis can be divided into three parts. Part one consists of lab scale experiments and measurements. In part two, the simulation model is described in detail and validation is done one to one with the experiments. In part three, the simulation model is used to measure stresses and develop constitutive equations.

Chapter 2 introduces the experimental setup, the measurement techniques and the measurements made for a number of parameters for two lab scale pseudo-2D fluidized beds.

Chapters 3 and 4 together make part two. Chapter 3 describes the CFD-DEM model in detail, including the contact model for spherocylinder particles, the volume fraction measurement and the drag models. The predictions of simulations are validated with experiments in Chapter 4.

The last part consists of Chapters 5 and 6. In Chapter 5, we perform measurements to understand the rheology of frictionless rod-like particle flows while focussing on the effect of the interstitial fluid medium. In chapter 6, we study the effect of friction coefficient for flow of granular rods in air as a fluid medium and propose constitutive equations for particle collisional stress and collisional pressure.

In Chapter 7, the general conclusions and outlook are given.

Chapter 2

Experimental Measurements

2.1 Introduction

Non-spherical particle fluidization has been gaining interest in recent years as a field of research. However, the focus has mainly been on numerical approaches, with experimental results being available, but scarce (Zhong et al., 2016). Among the earliest researchers in this field, Liu and Litster (1991) found that non-spherical particles tend to spout, forming high fountains. Liu et al. (2008) also conducted experiments and observed poor fluidizing quality as compared to spherical particles. Zhong et al. (2009) were among the first to present an experimental study on expansion ratio and pressure drop for rod-like particles. Vollmari et al. (2015) conducted research on the pressure drop and flow regime transitions of a variety of irregularly shaped particles. They found that as particles become more non-spherical, they are harder to fluidize and therefore require higher gas inlet velocities. For very elongated particles, channelling is observed instead of smooth fluidization (Vollmari, Jasevičius, and Kruggel-Emden, 2016).

Looking more on micro-scale, Cai, Li, and Yuan (2012) studied experimentally the orientation of cylindrical particles in a circulating fluidized bed and found the axes of cylindrical particles aligned upright during fluidization. Very recently, Boyce et al. (2016) studied gas, particle velocity and void fraction for fluidization of Kidney-bean-like particles via magnetic resonance imaging (MRI). A number of other experimental techniques like Magnetic Particle Tracking (MPT), Positron Emission Particle Tracking (PEPT) and Radioactive Particle Tracking (RPT) have also been used to study such sys-

---

This chapter is based on **Mahajan, V. V.**, Padding, J. T., Nijssen, T. M., Buist, K. A. and Kuipers, J. A. M., *Non-spherical particles in a pseudo-2D fluidized bed: Experimental study*, AIChE Journal **64**, 1573-1590 (2018).

tems (Buist et al., 2014; Chaouki, Larachi, and Duduković, 1997; Yang et al., 2007). These techniques can be effectively used to study the behaviour of particles in the bulk region of the bed. However, these techniques allow for tracking of single or few tracer particles for which quantities are then temporally averaged to get the general behaviour of particles in the bed. This does not allow for investigation of the collective motion of particles.

Co-fluidization of multiple particle shapes has been investigated as well (Shao et al., 2013). Studies on mixing and segregation have shown that differently shaped particles can separate when fluidized, even when their volume and density are similar (Escudie et al., 2006). Experimental studies indicate that sphericity alone is not sufficient to describe the effect of particle shape on fluidization behaviour. Multiple shape factors have been proposed to quantify this influence, such as the Zingg factor (Liu et al., 2008), the cross-wise and length-wise sphericity (Hölzer and Sommerfeld, 2008) and the aspect ratio (Gabitto and Tsouris, 2008). Correlations for drag force, pressure drop and flow-regime transitions based on the aforementioned shape factors were developed, with variable results. Even more so than experimental studies, numerical methods are employed to study non-spherical particle fluidization (Vollmari, Jasevičius, and Kruggel-Emden, 2016).

To further our understanding of such systems, in this chapter the fluidization of spherocylinder shaped particles is investigated using an experimental approach. In a pseudo-2D fluidized bed filled with spherocylindrical particles, pressure drop and bed expansion is measured as a function of the gas flow rate. Digital Image Analysis (DIA), Particle Image Velocimetry (PIV) and Particle Tracking Velocimetry (PTV) are used to determine particle coalignment, orientation, circulation patterns, coordination number and local particle dynamics in the bed. We also demonstrate with experiments the difference in fluidization behaviour for rod-like particles as compared to volume equivalent spheres.

2.2 Experimental setup

Experiments are conducted on two different scales with similar set-ups, in order to confirm that the observed behaviour is truly dictated by particle shape, not particle size. The set-ups are shown schematically in Figure 2.1, and specifications are given in Table 2.1. A pseudo-2D fluidized bed with a glass front wall is used. Flow distributors are used to guarantee a flat gas velocity profile entering the bed. A differential pressure sensor (MPX5050DP) is attached at the bottom of the beds to measure pressure drop.

The beds are filled with spherocylindrical particles (schematically shown in Figure

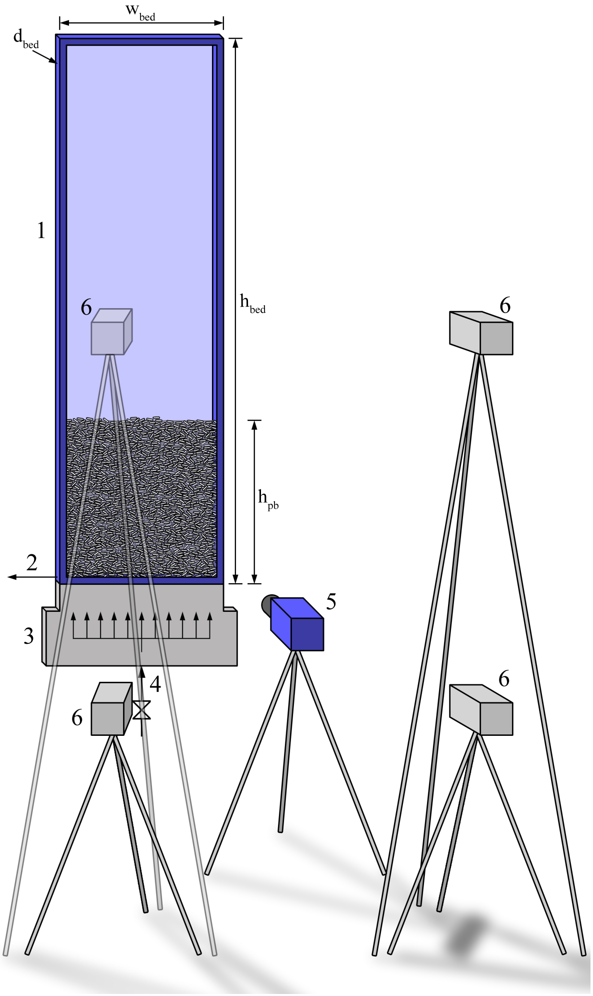

Figure 2.1: Representation of the experimental set-ups. The pseudo-2D fluidized bed (1) is filled to a packed bed height of approximately the bed width. Gas enters through the valve (4). A flow distributor (3) is used to guarantee a flat gas velocity profile entering the bed. Pressure measurements are taken at the bottom of the bed. The camera (5) is positioned in front of the bed, and surrounded by 4 lights (6). Dimensions are given in Table 2.1.

2.2) up to a packed bed height of approximately the bed width. Particle dimensions are given in Table 2.1. The particles are made of Alumide, a composite material of nylon and aluminium dust which is a high strength, low density material. The particles are produced using Selective Laser Sintering (SLS), a 3D-printing method. This technique allows for the inexpensive production of small particles, while still maintaining well-defined shape specifications. A number of independent size measurements were performed for a number of randomly selected particles. We found little or no variation in size (less than 0.1 mm differences). The particle density was measured by weighing 1000 particles using a VWR LPW-713i balance. The resulting measured density was 1395 kg/m^3.

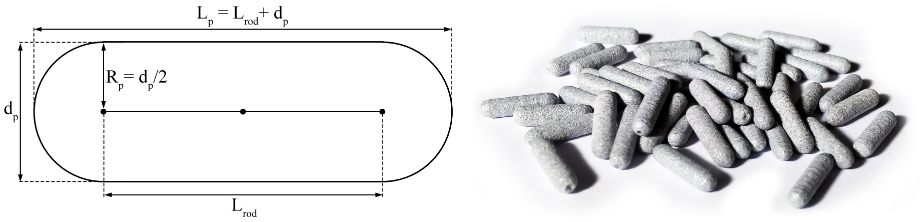

Figure 2.2: Geometry of the spherocylinderical particles (left) and 3D-printed particles (right). Dimensions are given in Table 2.1.

A Dantec Dynamics FlowSense EO 16M camera was used to capture images of the bed for DIA and PIV. Double frame images with a 2.0 ms interval were acquired at a rate of 3.0 Hz. 4 LED lights arranged around the camera were used to illuminate the bed (Figure 2.1). These lights were set to illuminate the bed for 200 μs for every frame taken.

Table 2.1: Dimensions of the set-ups (Figure 2.1) and spherocylindrical particles (Figure 2.2).

Property		Small scale	Large scale
Bed height	h_{bed}	0.5 m	1.0 m
Bed width	w_{bed}	0.1 m	0.3 m
Bed depth	d_{bed}	0.014 m	0.05 m
Packed bed height	h_{pb}	0.1 m	0.3 m
Particle length	L_p	$6.0 \cdot 10^{-3}$ m	$12.0 \cdot 10^{-3}$ m
Rod length	L_{rod}	$4.5 \cdot 10^{-3}$ m	$9.0 \cdot 10^{-3}$ m
Particle diameter	d_p	$1.5 \cdot 10^{-3}$ m	$3.0 \cdot 10^{-3}$ m
Volume equivalent spherical diameter	d_e	$2.6 \cdot 10^{-3}$ m	$5.3 \cdot 10^{-3}$ m
Bed weight	M_{bed}	0.11 kg	3.51 kg

2.2.1 Pressure drop measurements

Pressure measurements are taken using the differential pressure sensor attached to the bottom of each bed (see Figure 2.1), at a frequency of 100 Hz. The pressure drop results are compared with correlations found in literature. These correlations are listed in Table 2.2. For comparison, measurements in the packed bed regime at increasing gas velocity will be used, which are not subject to channelling. The bed porosity is calculated from the measured bed height (Section 2.2.2) and weight of the bed.

Correlations 1 to 8 in Table 2.2 were developed for spherical particles. These can be applied to beds of non-spherical particles by replacing the particle diameter d_p with the surface volume equivalent diameter d_{SV}, (Eq. 2.1, where V_p and A_p are respectively the particle volume and surface area). The Ergun equation already takes into account the viscous and kinetic pressure losses. Multiple adaptations of the Ergun equation take into account (Table 2.2,#2-8) wall effects by use of the hydraulic diameter D (Eq. 2.2). The correlation developed by Gibilaro, 2001 includes a correction term for beds with a high void fraction.

$$d_{SV} = 6\frac{V_p}{A_p} \tag{2.1}$$

$$D = \frac{2d_{bed}\, w_{bed}}{d_{bed} + w_{bed}} \tag{2.2}$$

Table 2.2: Correlations used to compare with the acquired pressure drop data.

#	Expression(s)	Author	Conditions
1	$\frac{\Delta P}{L} = 150\frac{(1-\epsilon)^2}{\epsilon^3}\frac{\eta g U_0}{d_p^2} + 1.75\frac{1-\epsilon}{\epsilon^3}\frac{\rho g U_0^2}{d_p}$	Ergun, 1952	$D/d_p \gg 10$
2	$\frac{\Delta P}{L} = 150\frac{(1-\epsilon)^2}{\epsilon^3}\frac{\eta g U_0}{d_p^2}M_{MH}^2 + 1.75\frac{1-\epsilon}{\epsilon^3}\frac{\rho g U_0^2}{d_p}M_{MH}$ $M_{MH} = 1 + \frac{4d_p}{6D(1-\epsilon)}$	Metha and Hawley, 1969	$7 < D/d_p < 91$
3	$\frac{\Delta P}{L} = 130\frac{(1-\epsilon)^2}{\epsilon^3}\frac{\eta g U_0}{d_p^2} + \frac{D/d_p}{2.28+0.335(D/d_p)}\frac{1-\epsilon}{\epsilon^3}\frac{\rho g U_0^2}{d_p}$	Foumeny et al., 1993	$3.23 < D/d_p < 23.8$
4	$\frac{\Delta P}{L} = K_1\frac{(1-\epsilon)^2}{\epsilon^3}\frac{\eta g U_0}{d_p^2}M^2 + 1.75\frac{1-\epsilon}{\epsilon^3}\frac{\rho g U_0^2}{d_p}\frac{M}{B_W}$ $B_W = \left(k_1(d_p/D)^2 + k_2\right)^2$	Reichelt, 1972	See Table 2.3

Table 2.2: Continued

#	Expression(s)	Author	Conditions
5	$\frac{\Delta P}{L} = 150\frac{(1-\epsilon)^2}{\epsilon^3}\frac{\eta_g U_0}{d_p^2}C_W^2 + 1.75\frac{1-\epsilon}{\epsilon^3}\frac{\rho_g U_0^2}{d_p}C_{Wi}$ $C_W = 1 + \frac{\pi d_p}{6D(1-\epsilon)}$; $C_{Wi} = 1 - \frac{\pi^2 d_p}{24D}\left(1 - \frac{d_p}{2D}\right)$	Liu and Masliyah, 1996	Unknown
6	$\frac{\Delta P}{L} = K_{1,Rai}\frac{(1-\epsilon)^2}{\epsilon^3}\frac{\eta_g U_0}{d_p^2} + K_{2,Rai}\frac{1-\epsilon}{\epsilon^3}\frac{\rho_g U_0^2}{d_p}$ $K_{1,Rai} = 103\left(\frac{\epsilon}{1-\epsilon}\right)^2\left(6(1-\epsilon) + \frac{80d_p}{D}\right)$ $K_{2,Rai} = 2.8\frac{\epsilon}{1-\epsilon}\left(1 - \frac{1.82d_p}{D}\right)^2$	Raichura, 1999	$5 < D/d_p < 50$
7	$\frac{\Delta P}{L} = 0.061\frac{1-\epsilon}{\epsilon^3}\left(\frac{D}{d_p}\right)^{0.2}(1000\mathrm{Re}_p^{-1}$ $+60\mathrm{Re}_p^{-0.5} + 12)\frac{\rho_g U_0^2}{d_p}$; $\mathrm{Re}_p = \frac{\rho_g U_0 d_p}{\eta_g}$	Montillet, Akkari, and Comiti, 2007	$3.8 < D/d_p < 14.5$
8	$\frac{\Delta P}{L} = \left(185 + 17\frac{\epsilon}{1-\epsilon}\left(\frac{D}{D-d_p}\right)^2\right)\frac{(1-\epsilon)^2}{\epsilon^2}\frac{\eta_g U_0}{d_p^2}$ $+\left(1.3\left(\frac{1-\epsilon}{\epsilon}\right)^{1/3} + 0.03\left(\frac{D}{D-d_p}\right)^2\right)\frac{1-\epsilon}{\epsilon^3}\frac{\rho_g U_0^2}{d_p}$	Cheng, 2011	$1.1 < D/d_p < 50.5$
9	$\frac{\Delta P}{L} = \left(18\frac{\eta_g}{\rho_g U_0 d_p} + 0.33\right)\frac{\rho_g U_0^2}{d_p}(1-\epsilon)\epsilon^{-4.8}$	Gibilaro, 2001	$0.4 \le \epsilon \le 1$
10	$\frac{\Delta P}{L} = \frac{150}{\phi^{3/2}}\frac{(1-\epsilon)^2}{\epsilon^2}\frac{\eta_g U_0}{d_p^2} + \frac{1.75}{\phi^{4/3}}\frac{1-\epsilon}{\epsilon^3}\frac{\rho_g U_0^2}{d_p}$	Nemec and Levec, 2005	$L_p/R_p \ge 1$
11	$\frac{\Delta P}{L} = \left(\frac{a}{\mathrm{Re}_{Duct}} + \frac{b}{\mathrm{Re}_{Duct}^c}\right)\rho_g\frac{U_0^2}{2}\frac{\sum A_p}{4\sum V_p}\frac{1-\epsilon}{\epsilon^3}$ $\mathrm{Re}_{Duct} = \frac{4\rho_g U_0}{\eta_g(1-\epsilon)}\frac{\sum V_p}{\sum A_p}$	Allen, Backstrom, and Kroger, 2013	See Table 2.3
12	$\frac{\Delta P}{L} = 4.466\mathrm{Re}_p^{-0.2}\phi^{0.696}\epsilon^{-2.945}e^{11.85(\log\phi)^2}$	Singh, Saini, and Saini, 2006	$1000 < \mathrm{Re} < 2700$

Correlations 10-12 were developed specifically for non-spherical particles. They include the sphericity ϕ (Eq. 2.3) or incorporate the particle volume and area directly. Correlation 12 by Singh, Saini, and Saini (2006) calls for the use of the volume equivalent diameter d_e (Eq. 2.4). Eisfeld and Schnitzlein (2001) reported coefficients for correlation 4 by Reichelt (1972) for non-spherical particles. These are given in Table

Table 2.3: Parameters for the Reichelt and Allen equations

Author	Parameters			Particle shape	Conditions
	K_1	k_1	k_2		
Reichelt, 1972	150	1.5	0.88	Spheres	$1.73 < D/d_p < 91$
Eisfeld and Schnitzlein, 2001	154	1.15	0.87	Spheres	$1.624 < D/d_p < 250$
	190	2.00	0.77	Cylinders	$1.624 < D/d_p < 250$
	155	1.42	0.83	All	$1.624 < D/d_p < 250$
	a	b	c		
Allen, Backstrom, and Kroger, 2013	240	10.8	0.1	Cubes	$\mathrm{Re} > 700$
	216	8.8	0.12	Cylinders	$\mathrm{Re} > 700$
	185	6.35	0.12	Rough spheres	$\mathrm{Re} > 700$
	150	3.25	0.15	Ellipsoids	$\mathrm{Re} > 700$

2.3, along with coefficients for correlation 11 by Allen, Backstrom, and Kroger (2013).

$$\phi = \frac{\pi^{\frac{1}{3}}(6V_p)^{\frac{2}{3}}}{A_p} = \frac{d_{SV}}{d_e} \tag{2.3}$$

$$d_e = \left(\frac{6}{\pi}V_p\right)^{\frac{1}{3}} \tag{2.4}$$

Fourier analysis

A fast Fourier transform (FFT) of the pressure drop signals converts it to a frequency domain from its time domain. We first apply a Hamming window function to the original pressure data to reduce spectral leakage. The squared amplitude of the resulting FFT is the power spectrum, which is routinely used to find dominant frequencies in the pressure signal (Trnka et al., 2000). These dominant frequencies can give an indication of the bubble frequency and associated particle mixing in the fluidized bed. This analysis is crucial in cases where visual measurement techniques cannot be employed such as in 3D opaque systems often encountered in industry. For this purpose, pressure measurements are taken at 100 hz for 10 minutes.

2.2.2 Digital Image Analysis

Bed height

In many studies, a threshold is applied to images to mark particle, bubble and freeboard areas (Busciglio et al., 2008; Goldschmidt et al., 2003; Shen, Johnsson, and Leckner, 2004). However, in this study a different approach is applied to the acquired images. In order to extract the bed height from images, the maximum intensity gradient along the height of the set-up is found. This method allows for improved particle detection in cases where contrast between the particles and the backplate is low. The procedure used in this study is described in detail below.

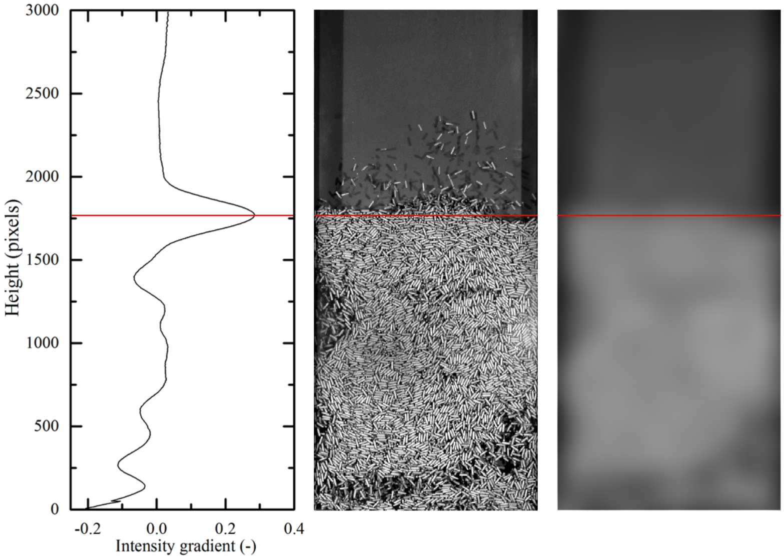

Figure 2.3: Demonstration of the bed height detection algorithm at $U_0 = 2.4$m/s. Left: intensity gradient. Middle: original image. Right: filtered image. Red lines indicate the detected bed height.

All image analysis techniques reported in this study use MATLAB® and the Image Processing Toolbox™. The brightness and contrast of the cropped image are automatically adjusted to obtain a more homogeneous illumination. Next, the image is blurred using a Gaussian filter. The average intensity of each row of pixels is calculated, and this curve is further smoothed. Its derivative is approximated by linear interpolation between adjacent points. The bed height is then defined by the height of maximum gradient. The algorithm is demonstrated in Figure 2.3. To verify the accuracy of the algorithm, sampled results were manually inspected at all flow rates.

Particle orientation

For spherical particles, the particle orientation is of no concern, and particle positions can be detected using a circle detection method, such as the Hough transform (Warr, Jacques, and Huntley, 1994). Very elongated (needle-like) particles can be represented as lines on images and a Hough transform for detecting lines can be applied (Duda and Hart, 1972). However, due to the intermediate aspect ratio of the particles used in this work, a different approach is needed. Hough transform methods for detecting ellipses have been developed, which can be used to detect the spherocylindrical particles (McLaughlin, 1998). However, finding 5 parameters per particle (x-position, y-position, major axis diameter, minor axis diameter and orientation), makes it very slow in processing the large images used in this study. Also correlation of all non-zero pixels in a 5-dimensional space, makes it very memory consuming. For these reasons, a new method to detect particle orientation has been devised.

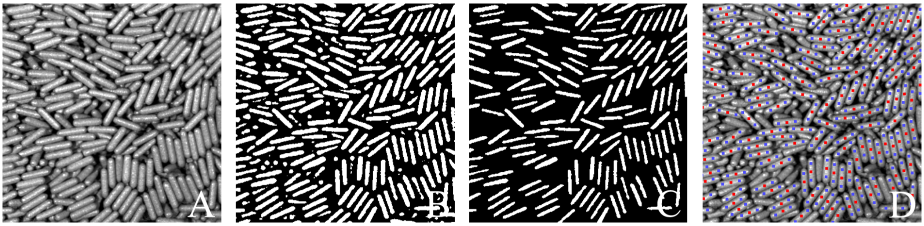

Figure 2.4: Example of the DIA procedure for orientation detection. The image is cropped and its brightness and contrast are adjusted (A). Next, a threshold is applied to remove the background particles (B). All parts too small or large are removed (C). The centre of mass of each particle is detected (D, red points). Lastly, the angle detection algorithm is applied (D, blue points).

The procedure for detecting the particles and their orientation is described below. An example is shown in Figure 2.4. These steps ensure that only individual particles lying parallel to the front wall are selected.

1. The cropped image (Figure 2.4-A) is imported and its brightness and contrast are adjusted.
2. An adaptive threshold is applied to separate the particles in the front plane from the surrounding shadows. (Figure 2.4-B)
3. The edges are smoothed and parts either too small or too large are removed. (Figure 2.4-C)
4. The particles are individually labelled and their centre of mass is determined using the `regionprops` function in the MATLAB® Image Processing Toolbox™. (Figure 2.4-D, red points)

5. The angle detection algorithm is applied. (Figure 2.4-D, blue points) This algorithm is described below and is visualized in Figure 2.5.
   (a) The aspect ratio of the particle is determined along two perpendicular axes. (Figure 2.5, top left)
   (b) The axes are rotated and the aspect ratio is determined at each angle. (Figure 2.5, top right)
   (c) The maximum aspect ratio is determined. The angle at which this occurs is taken as the particle angle. (Figure 2.5, bottom)

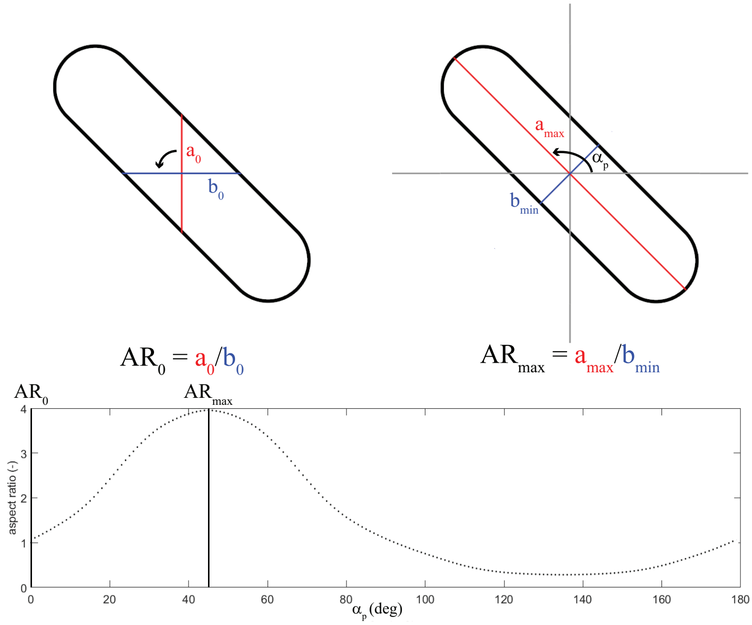

Figure 2.5: Algorithm for detection of particle orientation. Top left: the length and width of the particle are evaluated along two perpendicular axes. Top right: the axes are rotated around the centre of the particle. Bottom: the angle α_p that the rotating axis makes with the positive x-axis for maximum aspect ratio is extracted.

By manual inspection of images at all flow rates, it was estimated that approximately 90% of the particles oriented parallel to the front wall are detected by the algorithm. The efficiency of the angle detection is very high, >95% of the detected particles have their angle determined accurately. Multiple images at different flowrates were analyzed by hand and the results were compared with the algorithm results to confirm the detection accuracy. The efficiencies are equal for both beds because the entire setup and camera zoom is scaled with the particle size. The overall efficiency, the ratio of the particles with correct angles detected to the total number of particles in the bed is around 5%.

While this may appear low, it is an intrinsic limitation of optical analysis of an opaque bed where only the particles closest to the transparent wall are visible, and is almost impossible to improve significantly.

Particle coalignment

In order to quantify the particle coalignment, a spatial autocorrelation function is used. This function describes the alignment of a certain particle with another particle, separated by a distance r. The function definition is derived from the scalar product of the unit orientation vectors associated with each particle, and accounts for the symmetry of the particles. The autocorrelation function is defined by Eq. 2.5, where $C(r)$ denotes the correlation value at separation r, and $\alpha(r)$ signifies the in-plane orientation angle of a particle located distance r from the origin. Normalization is done assuming the particle orientation is non-correlated at infinite separation i.e. $\left\langle \cos^2(\alpha(0)-\alpha(\infty)) \right\rangle = 1/2$

$$C(r) = \frac{\left\langle \cos^2(\alpha(0)-\alpha(r)) \right\rangle - \left\langle \cos^2(\alpha(0)-\alpha(\infty)) \right\rangle}{\left\langle \cos^2(\alpha(0)-\alpha(0)) \right\rangle - \left\langle \cos^2(\alpha(0)-\alpha(\infty)) \right\rangle} = 2\left\langle \cos^2(\alpha(0)-\alpha(r)) \right\rangle - 1 \qquad (2.5)$$

In order to extract the correlation curve from experimental data, r is discretized into bins, up to the cut-off radius r_{cut} (set to 5 particle lengths). For each pair of particles with a separation smaller than r_{cut}, the correlation value is calculated and added to the mean in the associated bin. The analysis is performed for the entire height of the large bed. The bed is divided into three regions: < 2 L_p from the side wall, 2 L_p - 6 L_p from the side wall and > 6 L_p from the side wall. The correlation curves are calculated separately for each region. These boundaries are chosen such that the effect from the side walls can be assessed, while maintaining enough data in each region to obtain smooth curves.

2.2.3 Particle Image Velocimetry

PIV analysis was performed using LaVision DaVis 8.2.3 software. The multi-pass method was selected, using one pass with a 256 x 256 pixels interrogation cell and 50 % overlap, followed by 3 passes with a 128 x 128 pixels interrogation cell and 75 % overlap. As the maximum particle displacement between two frames is estimated at approximately 20 pixels, it is unlikely a particle will cross interrogation cell boundaries. Tests show that 3500 doubleframe images are sufficient to calculate time-averaged velocity profiles. See Figures 2.6 and 2.7.

At first glance, the averaged velocity profiles in Figure 2.6 may seem unphysical (net

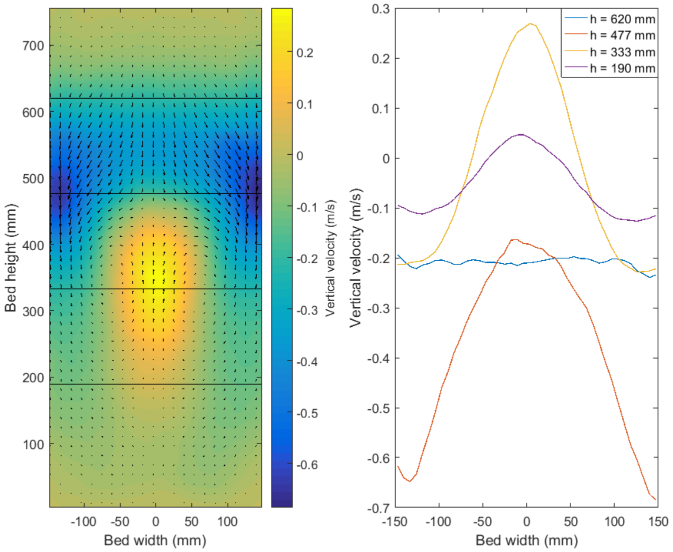

Figure 2.6: Left: measured average velocity profile at $U_0 = 1.6U_{mf}$, using 5000 doubleframe images. Vectors represent velocity magnitude and direction, colours represent vertical velocity magnitude. Right: Vertical velocity magnitude at different heights in the bed.

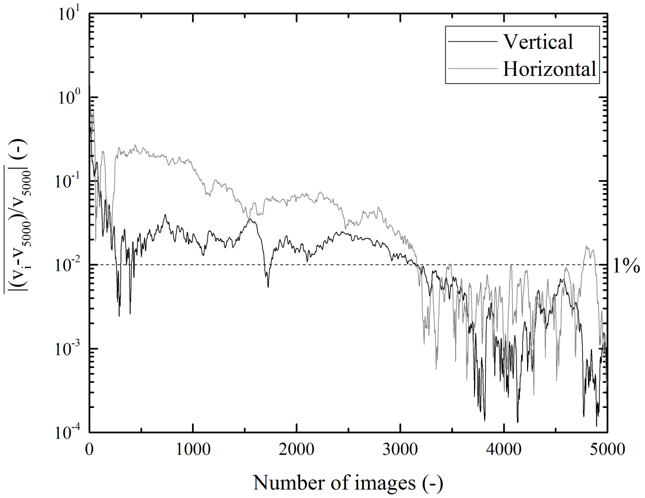

Figure 2.7: Relative deviation from mean velocity as a function of number of images taken. v_i represents the mean velocity calculated from i images.

negative velocity at h = 477 and 620 mm). However, this is a result of different times scales of the particles moving up and down. The particles move down over larger time scales (at higher average void fraction) than the particles moving up. Therefore, when cell-based velocities are averaged over a number of frames, without taking into account the actual void fraction, we find a net downward velocity. This is explained with a quantitative analysis of PTV measurements in Section 2.2.4 (Figure 2.25).

Void fraction calculation

In order to convert the velocity data obtained from PIV measurements to the mass flux, the local void fraction in the bed must be known. This is expressed by Eq. 2.6, where $\vec{\phi}_m$ is the local mass flux, $\vec{v}$ the particle velocity, ρ_p the particle density and ϵ the local void fraction.

$$\langle\vec{\phi}_m\rangle = \langle\vec{v}\rho_p(1-\epsilon)\rangle \tag{2.6}$$

First, the two-dimensional void fraction is obtained. Two commonly used approaches to obtain the 2D void fraction are to distinguish between the bubble phase and emulsion phase in the bed (Olaofe et al., 2013; Busciglio et al., 2008) or to correlate the average pixel intensity in an area with the local void fraction in that area (Buijtenen et al., 2011; Buist et al., 2014). However, both of these methods prove to have their own limitations. The fluidization behaviour of the Geldart D particles used in this study does not allow for formation of discrete distinguishable bubbles. Thus, the first method cannot be applied here. The latter method produces unsatisfactory results due to the low contrast between particles and background and the non-uniform lighting. Therefore, the latter method has been extended with a threshold-step, as described below.

1. The particles are separated from the background as reported in Section 2.2.2 (Steps 1-2).
2. The image is divided into grid cells of identical size as the PIV results.
3. The total area of the particle phase in each grid cell is calculated.
4. Particle pixel area is converted linearly to 2D solid volume fraction by use of the known total solid volume in the bed.

Next, the 2D void fraction is converted to the physical 3D void fraction. This is done using the method described by De Jong et al. (2012) and Buijtenen et al. (2011), which is expressed by Eq. 2.7. Here, B gives the location of the asymptote and A scales the curve. Because the 3D void fraction is a property not easily measured experimentally, CFD-DEM simulation data is used to find fitting parameters A and B. The simulation data

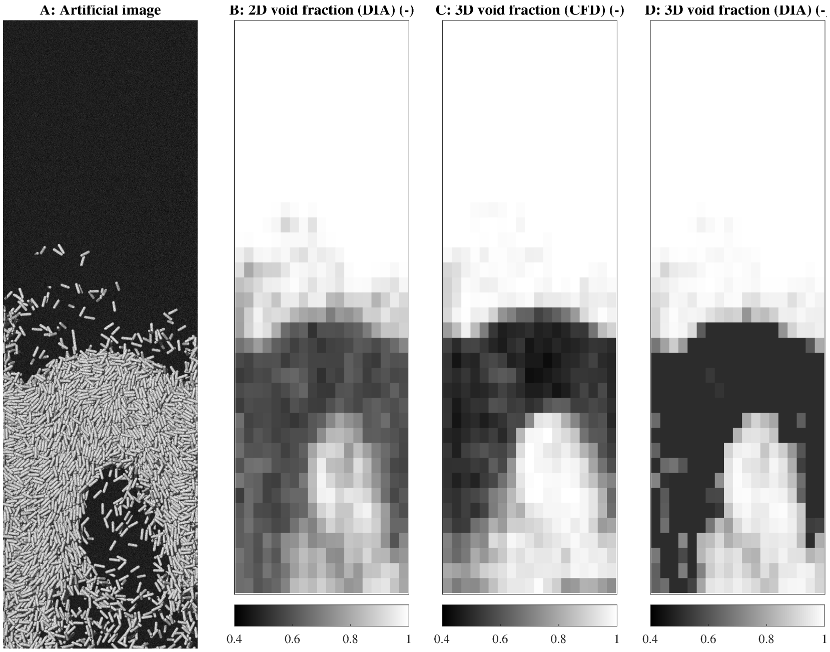

Figure 2.8: Demonstration of the void fraction calculation from artificial images. The artificial image (A) is generated to resemble experimental conditions as closely as possible. Using the image analysis algorithm, the 2D void fraction (B) is calculated, which is compared with the 3D void fraction from the CFD model (C). From this, the coefficients in Eq. 2.7 are fitted, resulting in the 3D void fraction from image analysis (D).

is used to create artificial images of the small set-up using OVITO© software (Stukowski, 2009). The lighting is adjusted to represent experimental conditions as closely as possible. The algorithm above is then used to obtain the 2D void fraction from these images, which can be compared to the physical 3D void fraction from the simulation results. A demonstration of this method is given in Figure 2.8.

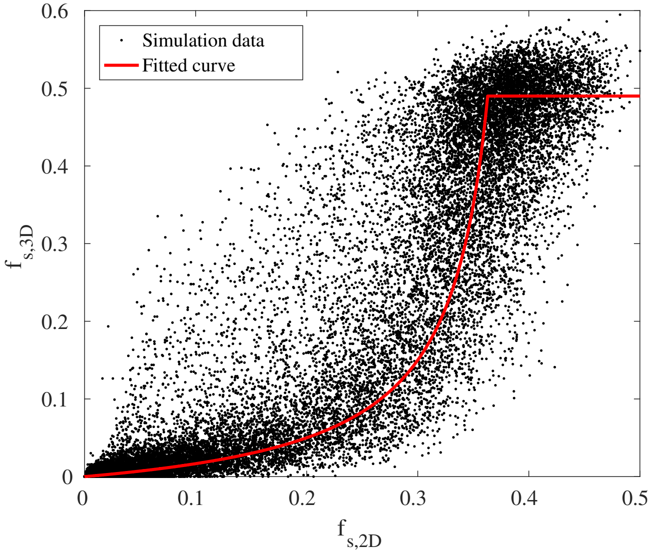

Figure 2.9: Correlation of 2D and 3D solid volume fraction. Points represent the simulation data, the line represents the fitted curve (Eq. 2.7). Parameters found are $A = 0.05$ and $B = 0.45$.

$$f_{s,3D} = \begin{cases} f_{s,3D,max} & \text{for } f_{s,3D} \geq f_{s,3D,max} \\ \dfrac{A_f f_{s,2D}}{B_f - f_{s,2D}} & \text{for } f_{s,3D} < f_{s,3D,max} \end{cases} \tag{2.7}$$

Non-linear curve fitting was used to obtain the values for A_f and B_f. The results from this fitting is shown in Figure 2.9. These were obtained using 190 artificial images from a simulation of the small bed at $U_0 = 2.6$ m/s. From the known packed bed height, it is found that $f_{s,3D,max} = 0.49$. The parameters found are $A_f = 0.05$ and $B_f = 0.45$. The value of A_f is adapted slightly for each image to ensure mass conservation. A demonstration of the algorithm is given in Figure 2.10.

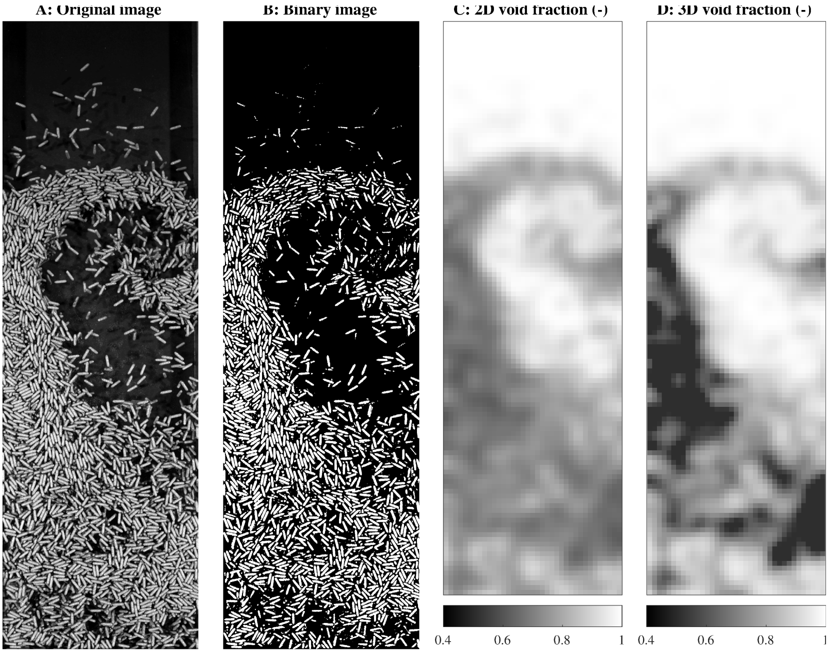
A: Original image
B: Binary image
C: 2D void fraction (-)
D: 3D void fraction (-)
0.4
0.6
0.8
1
0.4
0.6
0.8
1

Figure 2.10: Demonstration of the void fraction calculation on the small bed. The original image (A) is binarized (B). From the particle phase area, the 2D void fraction (C) is calculated, which is then converted to the 3D void fraction (D) according to Eq. 2.7.

2.2.4 Particle Tracking Velocimetry

To investigate the movement and orientation of individual particles, Particle Tracking Velocimetry (PTV) was used. In PTV the displacement of each individual particle is tracked, as opposed to PIV, where the average displacement of groups of particles is measured. For these measurements, a LaVision HighSpeedStar camera was used to capture a 15 × 15 cm area of the large bed. A frame rate of 500 Hz and a resolution of 1024 × 1024 pixels were used. This framerate was chosen such that the particle movement can be tracked accurately. In order to track the particles over multiple frames, a Nearest Neighbor Search interrogation strategy by Adrian and Westerweel (2011) was used. This algorithm is explained below. An example is shown in Figure 2.11.

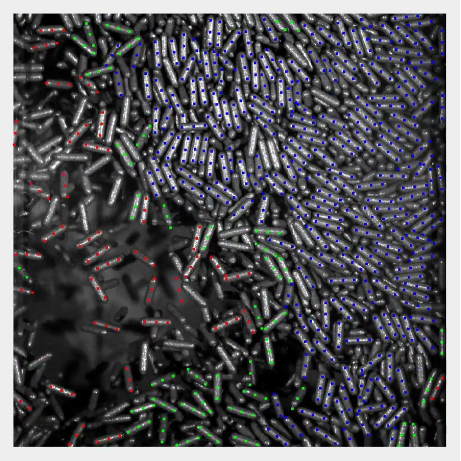

Figure 2.11: An example of PTV procedure showing coordination number indicated by color codes : blue(dense) with CN 9 or higher, green(medium) with CN from 5 to 8, red(dilute) having CN less than 5.

1. The position and orientation of the particles in the frame are analysed using the algorithm described in Section 2.2.2.
2. The distance between each particle in the current frame and each particle in the previous frame is calculated.
3. Pairs of particles with minimal displacement are given the same index.
4. Any possible conflicts where one particle is linked to multiple other particles due to a particle moving in or out of the frame are eliminated by selecting the pair with the smallest displacement.
5. Any particle in the current frame that is not linked to a particle in the previous frame is given a new index.

6. Steps 1 - 5 are repeated for all frames.
7. Paths shorter than 4 frames are removed from the data, as they are not suitable for analysis.
8. Using the camera resolution and frame rate, velocities are calculated from their displacement.
9. Based on its number of nearest neighbours, the coordination number (CN), defined as the number of neighbours within a radius of L_p, is calculated for each particle.
10. To account for walls, the CN is normalized using the area of the search area which lies inside the bed.

2.3 Results and discussion

In this section, results obtained from the aforementioned experimental techniques are presented. The results for particle orientation, particle co-ordination number and particle co-alignment are presented for the large particles (L_p = 12 mm).

2.3.1 Fluidization regimes

Over the range of gas velocities, the different fluidization regimes described below are observed. Examples of each regime are shown in Figure 2.12. Similar behaviour was observed by Kruggel-Emden and Vollmari (2016) for elongated cuboids of comparable dimensions as the large particles.

- Packed Bed (PB): At low flow rates, the particles are stationary. The gas passes through the voids between the particles without moving the bed. (Figure 2.12-A)

- Passive Channelling (PC): The gas flow creates paths free of particles. These channels are fairly stable and exist for multiple minutes. When the gas velocity is lowered back into the packed bed region, the channels remain. (Figure 2.12-B)

- Active Channelling (AC): Large amounts of particles are sucked into the channels and fountains are formed. The channels are wider compared to the passive channelling phase. They collapse rapidly and new paths are created continuously. As particles move up through the channels, there is a slow downward movement in the bulk phase. When the flow rate is increased, bubbles start moving through the channels. This regime is only observed for the large particles. One of the possible reasons for this is particle roughness which is relatively more pronounced for smaller particles. The smaller particles therefore need additional force to be pulled

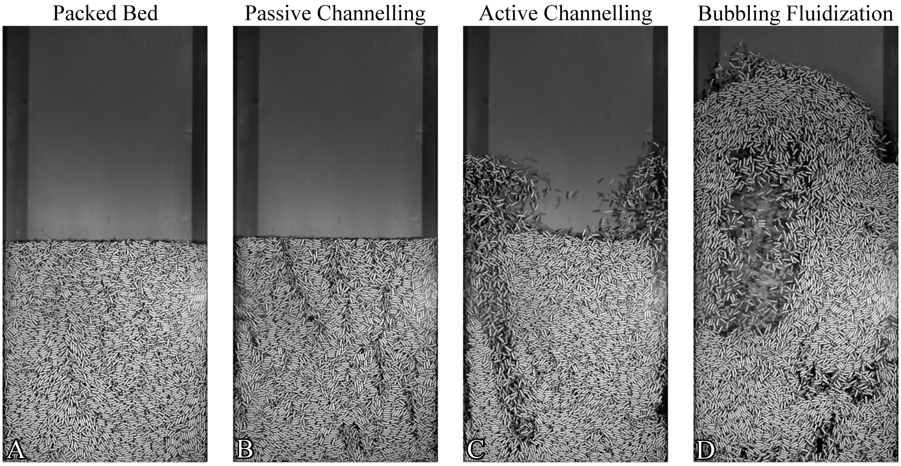

Figure 2.12: Examples of the different fluidization regimes observed in the large bed with increasing gas velocity. A: U_0 = 0 m/s, B: U_0 = 1.5 m/s. C: U_0 = 1.9 m/s, D: U_0 = 2.4 m/s.

from a relatively dense packing. (Figure 2.12-C)

- Bubbling Fluidization (BF): Bubbles form close to the distributor plate, which coalesce and move upward. When bubbles erupt at the surface, particles are thrown high into the freeboard region. At higher gas velocities, bubbles grow larger. In this state, the bed is very chaotic and unstable. Particles show interlocking behaviour, where they move in large packed groups. (Figure 2.12-D) In general, it is observed that normal bubbling patterns, as observed for spherical particles, are suppressed for non-spherical particles. The formation and relatively smooth passage of bubbles is inhibited due to particle entanglement, which leads to large internal particle stresses and difficulties for particles to move relative to each other.

A possible correlation can be observed between regimes observed for elongated particles and spherical particles with a high coefficient of friction or cohesive forces. Elongated particles are prone to channeling, similar to fluidization behaviour observed for Geldart C particles (Wang, Kwauk, and Li, 1998). In both cases, the particles under consideration have to overcome the resistance of surrounding relatively dense packing of particles to be able to move. Once the particles overcome this critical force with the help of fluid drag, the steady structure breaks. The surrounding particles are dragged with the fluid and follow the created flow path, which we term channeling. Thus, even though the physical origin for the observed channelling behaviour is different, entanglement versus cohesive forces, the effect is very similar.

2.3.2 Pressure drop

Results for the pressure drop measurements are shown in Figure 2.13 (A-B). Measurements were taken for 100 s at 100 Hz at both increasing and decreasing flow rate. Error bars indicate the standard deviation of the measurement, defined by Eq. 2.8, where S is the standard deviation and A is a series of N measurements, of which $\bar{A}$ is the mean value.

$$S = \sqrt{\frac{1}{N-1}\sum_{i=1}^{N}|A_i - \bar{A}|^2} \tag{2.8}$$

The minimum fluidization velocity (U_{mf}) was determined by the intersection of the static pressure drop and the packed bed pressure drop at decreasing flow rate, according to Kunii and Levenspiel (1991). This procedure is shown in Figure 2.14. Values of U_{mf} = 1.26 m/s (small particle) and U_{mf} = 1.70 m/s (large particle) were found.

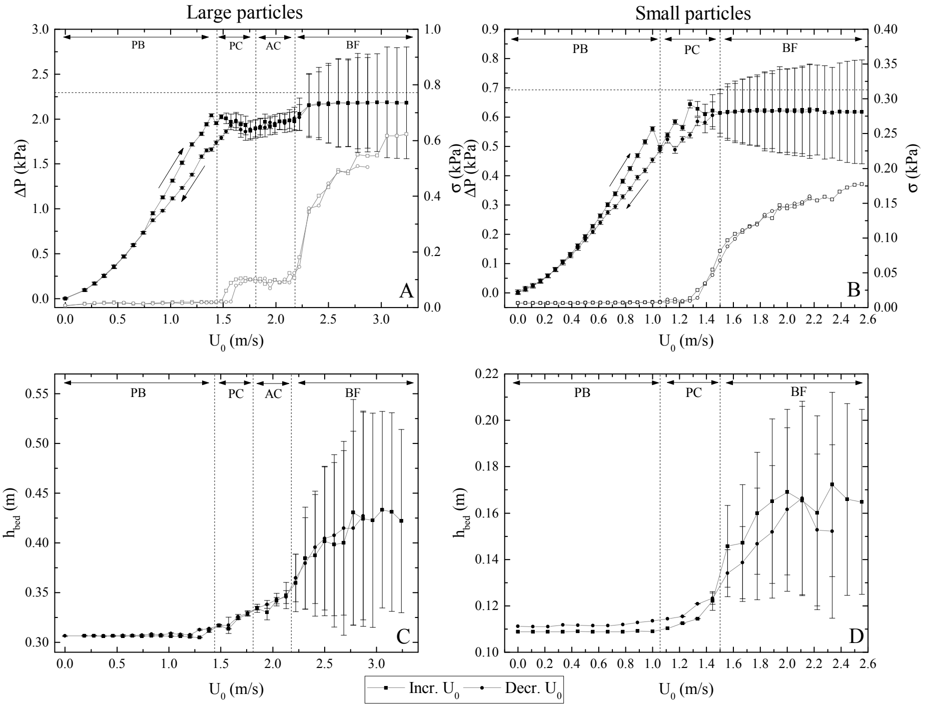

Figure 2.13: Measured pressure drop (A-B) and bed height (C-D) for the large (A-C) and small (B-D) particles. The open symbols represent standard deviation in pressure drop. Vertical dashed lines show the transition between fluidization regimes. Horizontal dashed lines show the static pressure drop (Eq. 2.9).

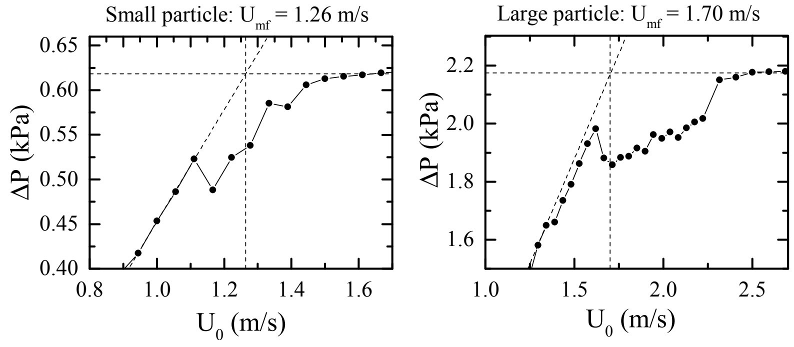

Figure 2.14: Determination of the minimum fluidization velocity (U_{mf}).

The pressure drop curves show a plateau at a value lower than the static pressure drop, indicating channelling (Geldart, 1986). In the channelling regimes, the pressure drop levels off, and pressure fluctuations start to occur. In the bubbling region, pressure drop increases and reaches a constant value (static pressure drop). There are very large pressure drop fluctuations, caused by the large bubbles in the system (Howard, 1983). The difference between the increasing and decreasing flow rate curves show that when gas velocity is lowered from the PC to PB regime, the channels remain, as indicated by the lower pressure drop.

$$\Delta P = \frac{g M_{bed}}{A} \tag{2.9}$$

The pressure drop caused by the weight of the bed is expressed by Eq. 2.9. This value is 5-10% higher than the measured static pressure drop. This indicates part of the particle weight is supported by the bed walls and bottom plate. As the small set-up is smaller relative to the particle size than the large bed, the difference is larger (Figure 2.13).

2.3.3 Bed height

Figure 2.13 (C-D) shows the measured bed height. The regimes shown in Figure 2.12 are also reflected in bed height measurements. From the onset of channelling, the bed slowly expands. In the bubbling fluidization regime, the bed height increases rapidly. It is also clear that at this high flow rate, the fluctuations in bed height become very strong. As the particles are in the Geldart D class, fluidization is very unstable (Geldart, 1973). There is no sharp, identifiable bed height. Instead, particles are thrown high into the freeboard region and form large bubbles, as shown in Figure 2.12-D.

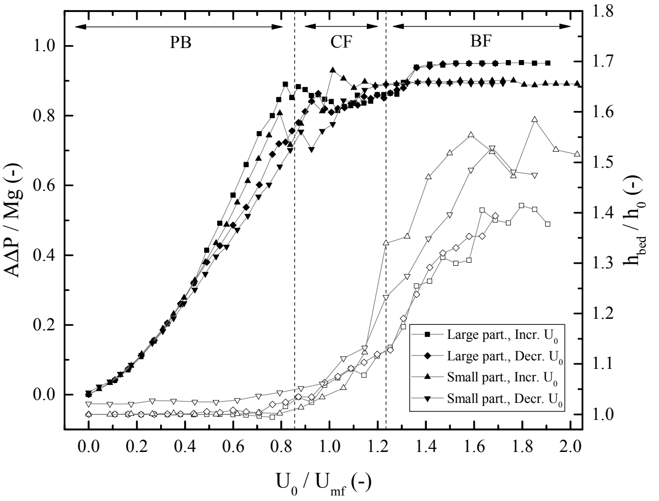

Figure 2.15: Normalized pressure drop and bed expansion as a function of normalized gas velocity for both particles sizes. Solid symbols represent pressure drop, open symbols show the bed expansion.

Figure 2.15 shows the normalized pressure drop and bed height as a function of normalized gas velocity for both large and small particles. It is clear from the plot that the behaviour of the particles is similar for both the particle sizes. This indicates that the particle behaviour is shape-induced.

2.3.4 Spherical particles

In order to compare the fluidization behaviour of the spherocylinders with that of spheres, the pressure drop over the small set-up filled with approx. 9500 spherical particles was measured. These particles were fabricated from the same Alumide material and are of equal volume as the small spherocylinders ($d_p = 2.6 \cdot 10^{-3}$ m). Results are shown in Figure 2.16.

For these particles no channelling is observed; at the minimum fluidization velocity of 1.04 m/s the bed immediately transfers from the packed bed to bubbling fluidization regime. This proves that the observed fluidization behaviour is caused by the particle shape, not by their material or size. When Figure 2.16 is compared to Figure 2.13, we find that the minimum fluidization velocity for spherical particles is lower compared to non-spherical particles (of equivalent volume). This is due to the fact that when the flowrate is lowered, non-spherical particles are prone to form channels. As the gas flowrate is further lowered, these channels remain to exist, therefore allowing a signifi-

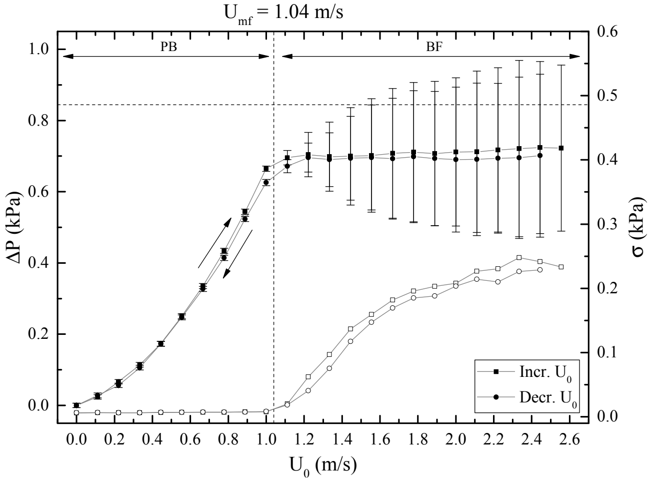

Figure 2.16: Pressure drop over the small set-up filled with spherical particles. Particles are of equal volume as the small spherocylinders. Open symbols indicate standard deviation of the pressure fluctuations. The horizontal dashed line represents total weight of the particles.

cant amount of gas to pass through. This leads to a higher U_{mf} compared to spherical particles.

2.3.5 Pressure drop correlations

The predictive quality of a correlation is expressed by its coefficient of determination, noted R^2 (Eq. 2.10, where y are the measured values for the non-spherical particles and f the predicted values).

$$R^2 \equiv 1 - \frac{\sum(y_i - f_i)^2}{\sum(y_i - \bar{y})^2} \tag{2.10}$$

Table 2.4 shows the R^2 for all correlations given in Table 2.2, when used to predict pressure drop over the large particle bed. It can be seen that the correlation of Montillet *et al.* (7) most accurately predicts the pressure drop in the packed bed regime, while the correlations by Ergun (1), Liu and Masliyah (5) and Eisfeld and Schnitzlein (4-3) perform satisfactory as well. Figure 2.17 shows the relative error (Eq. 2.11) of all correlations with $R^2 > 0.8$ as a function of the gas velocity.

$$\text{Error} = \frac{\Delta P_{pred} - \Delta P_{meas}}{\Delta P_{meas}} \cdot 100\% \tag{2.11}$$

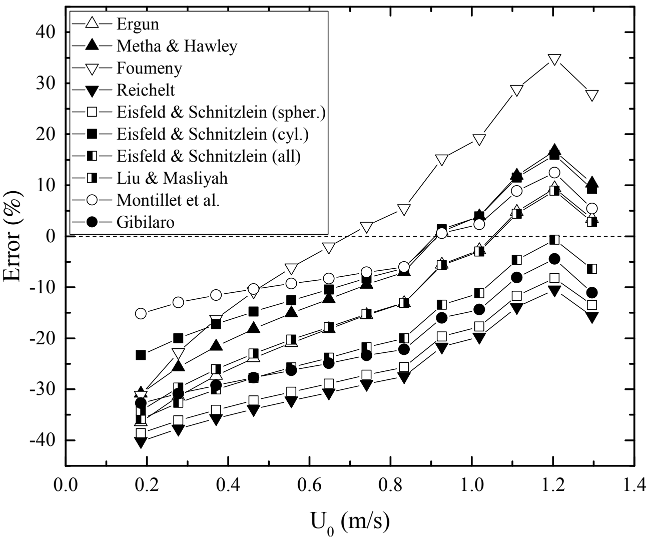

Figure 2.17: Relative error of all pressure drop correlations with $R^2 > 0.8$, as a function of superficial gas velocity.

Most correlations underestimate the pressure drop at low flow rates, and overestimate at higher flow rates. It is to be noted that the correlations have been developed for specific particle and setup specifications. For example, the correlation of Reichelt and Allensee in Table 2.3 is developed specific to spheres, cylinders, cubes etc. On the same hand, we use these correlations to measure pressure drop for a bed of spherocylindrical particles. Therefore, some correlations perform better than others.

It can also be seen that the error shows a positive trend with increasing gas velocity. At low velocity, all correlations under predict the pressure drop more than at higher velocity. At zero gas velocity, particles align with each other, forming very small spaces between them and increasing the pressure drop. Approaching the minimum fluidization velocity, particles slowly start aligning with the gas flow and form channels between them. This lowers the overall pressure drop. As the pressure drop correlations do not take these changing orientation effects into account, they under predict at low gas velocity and over predict at the higher gas velocities.

2.3.6 Pressure drop Fourier analysis

Figure 2.18 shows the FFT analysis of pressure drop for small particles and their volume equivalent spherical particles. The curves are smoothed using moving window averaging. It can be seen that the dominant frequency is around 3 Hz and slightly increasing

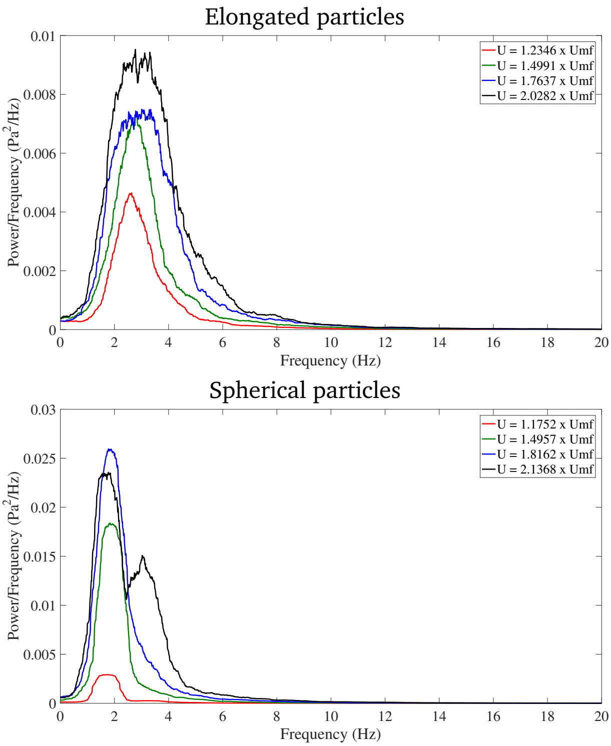

Figure 2.18: Power spectrum of pressure drop for small spherocylinder particles (top) and volume equivalent spherical particles (bottom) at different gas inlet velocities (U) shown as a function of minimum fluidization velocity (Umf). The curves are smoothed for clear representation.

Table 2.4: Coefficient of determination for the pressure drop correlations.

#	Author	R^2
1	Ergun	0.97
2	Metha & Hawley	0.96
3	Foumeny	0.81
4-1	Reichelt	0.88
4-2	Eisfeld & Schnitzlein (spheres)	0.90
4-3	Eisfeld & Schnitzlein (cylinders)	0.97
4-4	Eisfeld & Schnitzlein (all shapes)	0.95
5	Liu & Masliyah	0.97
6	Raichura *et al.*	0.38
7	Montillet *et al.*	0.98
8	Cheng	0.74
9	Gibilaro	0.93
10	Nemec & Levec	0.48
11-1	Allen *et al.* (cubes)	< 0
11-2	Allen *et al.* (cylinders)	< 0
11-3	Allen *et al.* (rough spheres)	0.62
11-4	Allen *et al.* (ellipsoids)	0.61
12	Singh *et al.*	< 0

with increasing gas velocity. This was also confirmed from visual observations of the bubble frequency in the bed.

It can also be seen that the peaks are sharper for spherical particles and broader for elongated particles. This indicates a clear preference towards bubble formation for spherical particles and more chaotic behaviour of non-spherical particles. Rod-like particles oppose the formation of bubbles. At high gas flowrates, for spherical particles we observed that bubbles erupt with varying intensity. Once a large intensity bubble has passed, a large volume of gas leaves the bed leading to small intensity bubbles. This is the reason we observe double peaks at higher gas flowrates for spherical particles.

2.3.7 Void fraction and mass flux

Figure 2.19 shows the velocity and mass flux profiles for the large bed at $U_0 = 3.24$ m/s. As can be seen, at a bed height of 600 mm the average particle velocity shows a net downward flow. However, when accounted for void fraction, the average mass flux profile shows net mass flux close to zero at different heights of the bed.Figure 2.20 shows a quantitative comparison of vertical mass flux for the small and large bed at one height.

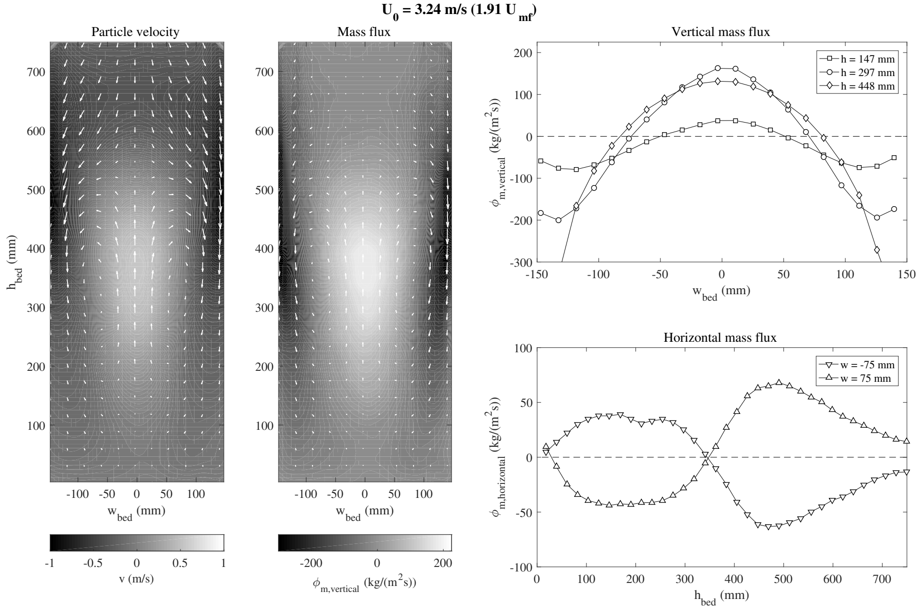

Figure 2.19: Particle velocity and mass flux results from experiments in the large set-up at U_0 = 3.24 m/s.

In Figure 2.21, mass flux profiles obtained from PIV in both the small and large setup are shown. These profiles show the transition from channelling to the vigorously bubbling fluidization state. At gas velocities just above the minimum fluidization velocity, solids circulation is dominated by channelling and particle raining. As the gas velocity progresses in the bubbling fluidization regime, the well-known circulation pattern emerges, where particles mainly move up through the centre and come down along the walls. This shows that, while their non-sphericity delays the fluidization of the spherocylindrical particles, at sufficiently high gas velocities solids circulation is qualitatively similar to that of beds of spherical particles.

Since the particles are circulating in a closed system, there should be zero net mass flux through each horizontal plane in the bed. However, from the obtained velocity profiles combined with solid volume fraction calculation via DIA, current results do not entirely follow this behaviour, especially for the large set-up. This is caused by the inaccuracy of the void fraction calculation; as the frontal area of the bed is very large, it is very challenging to obtain a uniform lighting. This results in discrepancies in the local void fraction, which reflect in the mass flux profile. As for the small bed it is much more straightforward to obtain a uniform lighting, the mass flux results are much more accurate. The discrepancy in mass flux can partly be also due to the comparatively large

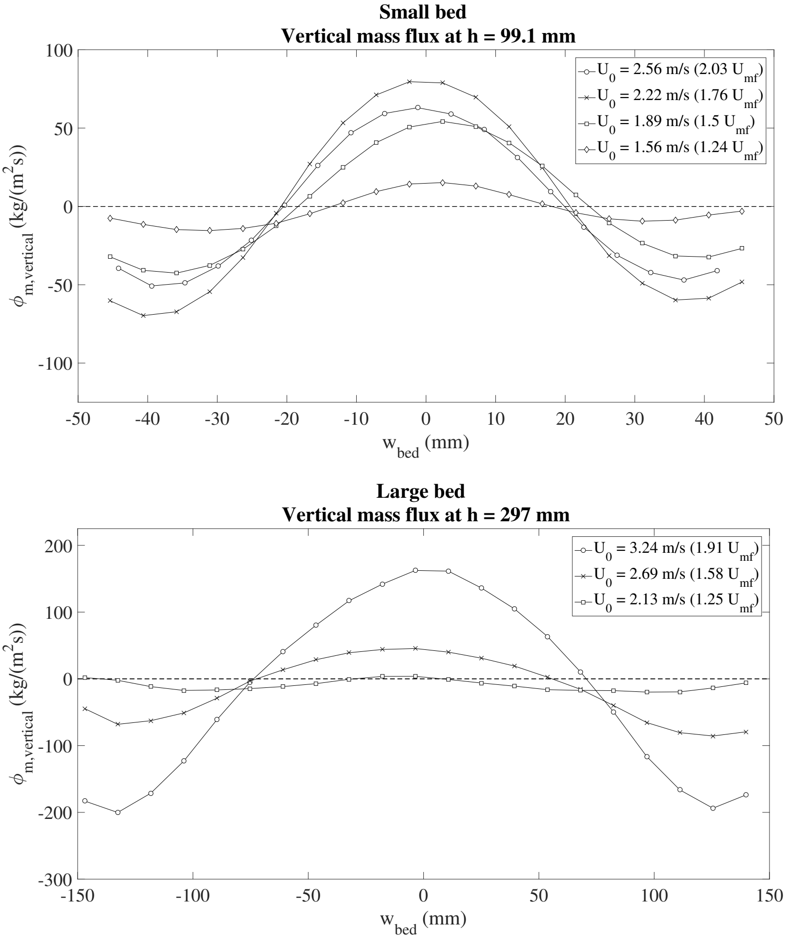

Figure 2.20: Mass flux profiles at different flow rates for the small bed (top) at height 99.1 mm and large bed (bottom) at height 297 mm.

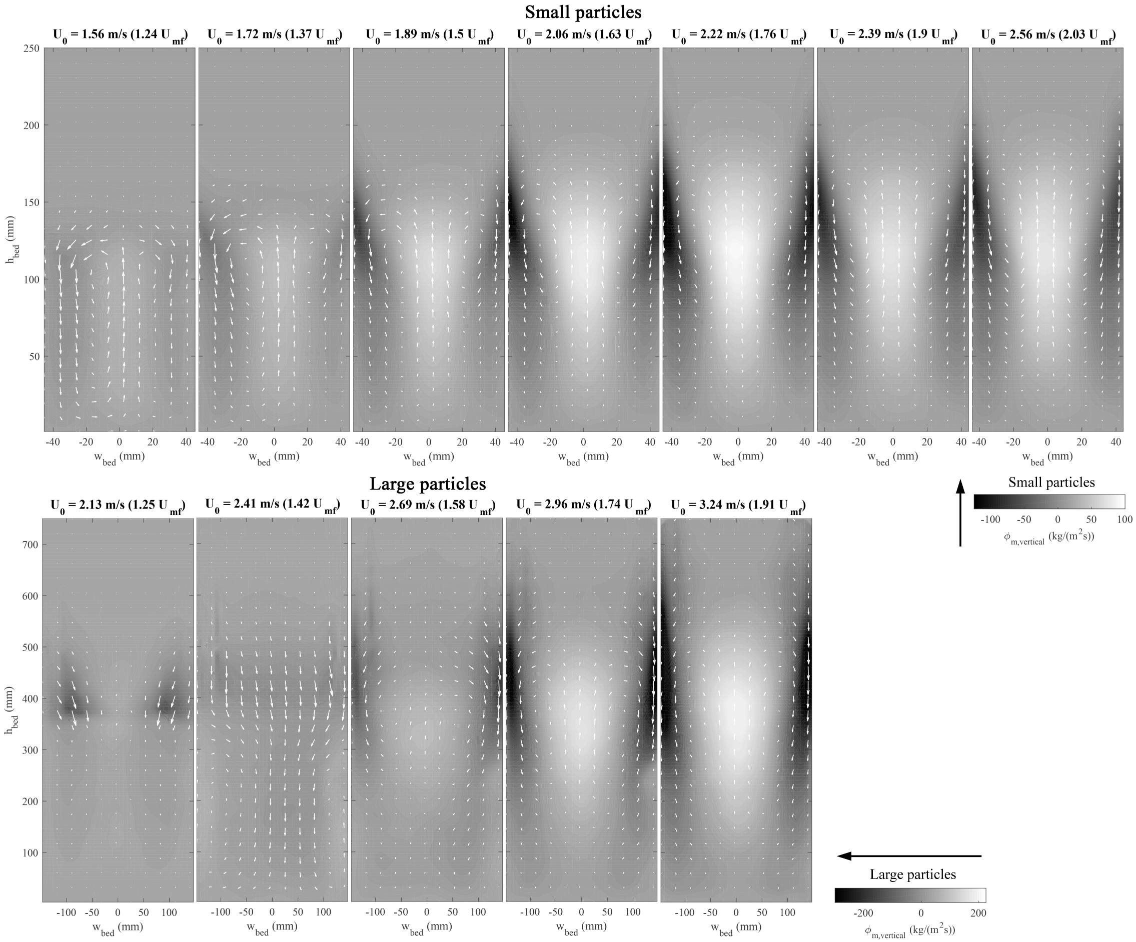

Figure 2.21: Mass flux profiles at different flow rates for the small (top) and large (bottom) particles. Arrows represent mass flux magnitude and direction. Background colour represent vertical massflux magnitude, indicated by the colour bars. Note that the vector length scale is not consistent between figures.

bed depth while the optical techniques we employ limit measurements to the frontal portion of the bed.

2.3.8 Particle orientation

Figure 2.22 (top) shows the Probability Density Function (PDF) for the particle orientation in the large set-up at different flow rates. The PDF is given by Eq. 4.1, where $N_p(\alpha)$ is the number of particles at angle α.

$$PDF(\alpha) = \frac{N_p(\alpha)}{\int_{-90}^{90} N_p(\alpha)d\alpha} \tag{2.12}$$

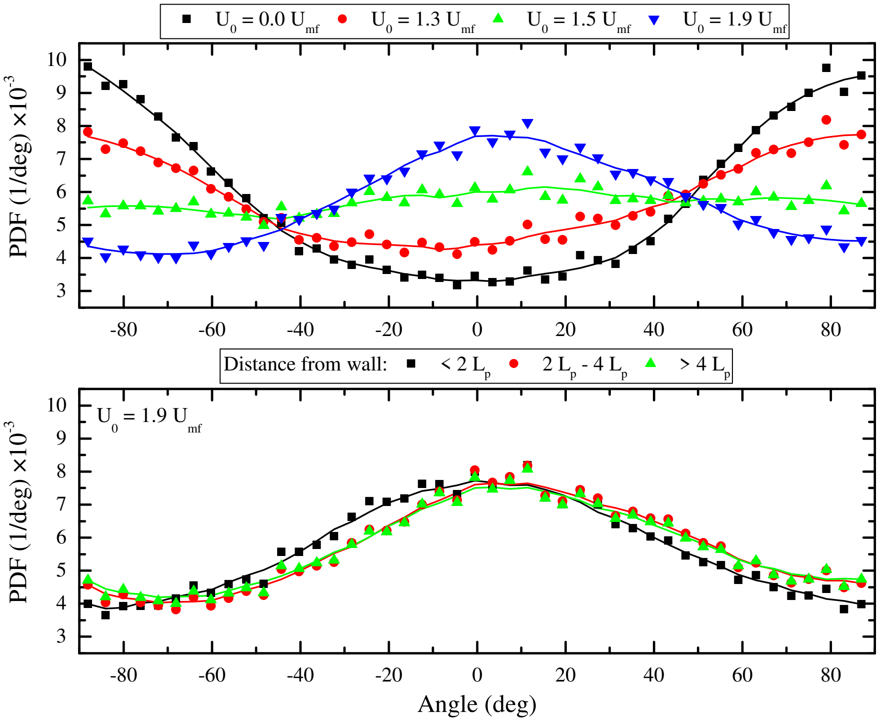

Figure 2.22: Probability Density Function (PDF) of the particle orientation (as observed from the front wall) in the large setup at different flow rates (top) and different positions in the bed (bottom, $U_0 = 1.9\ U_{mf}$). Angles of -90 and 90 degrees correspond with particles laying down horizontally, an angle of 0 degrees corresponds with particles standing up vertically. Lines are smooth fits.

From zero flow rate up to the onset of bubbling fluidization, particles predominately lie down horizontally, as is expected from a particle at rest. At high gas velocity, the flow causes particles to align themselves vertically. As the particles are pushed up at high gas velocities, the interaction with surrounding particles causes them to align themselves vertically. At intermediate flow rates, there is no clear preferred orientation. Similar behaviour was reported by Cai, Li, and Yuan (2012) for cylindrical particles. Overall, preferred orientational behaviour cannot be attributed to one single factor but is a result of several competing factors including particle-particle interaction, hydrodynamic lift, torque and drag. From Figure 2.22 (bottom), which shows the PDF at the highest flow rate at different positions in the bed, it can be seen that the upright position of the particles is due to the gas flow, not due to wall proximity. Particles close to the wall and in the bulk show a very similar PDF.

2.3.9 Particle coalignment

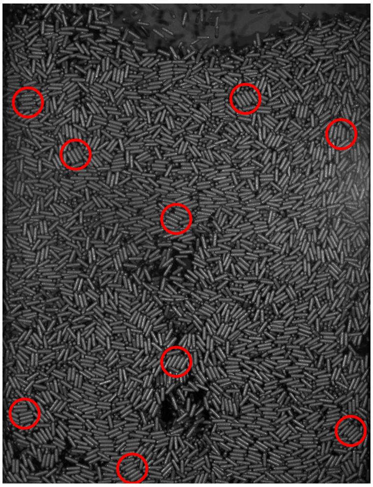

Figure 2.23: An example of particle coalignment for the large bed at $U_0 = 2.13$ m/s. The red circles indicate a few instances of particles largely coaligned within a distance of one particle length from a respective particle.

Figure 2.23 shows a snapshot of the large bed at $U_0 = 2.13$ m/s. The particles are largely coaligned within a distance of approximately one particle length from each respective particle. These visual observations of coalignment below a particle length reflects in our quantitative measurements. Results of the orientation autocorrelation in the large bed at $U_0 = 2.13$ m/s are shown in Figure 2.24. The solid lines and symbols represent the measured data, the dashed lines show the fitted exponential decay. At correlation lengths below the particle length, there is direct orientational particle-particle interaction (due to particles in contact with each other). This results in a high correlation value, which decays fast. At larger correlations length, there is indirect orientational interaction between the particles, leading to an (approximately) exponentially decaying correlation value. At this gas flow rate, still partially in the channelling regime, there is a high correlation length near the wall and a much lower value in the bulk. This is explained by the fact that channels form mainly in the centre of the bed, not near the wall. The indirect interaction (stacking) is especially strong outside the channels, where particles are largely stationary, as is expected.

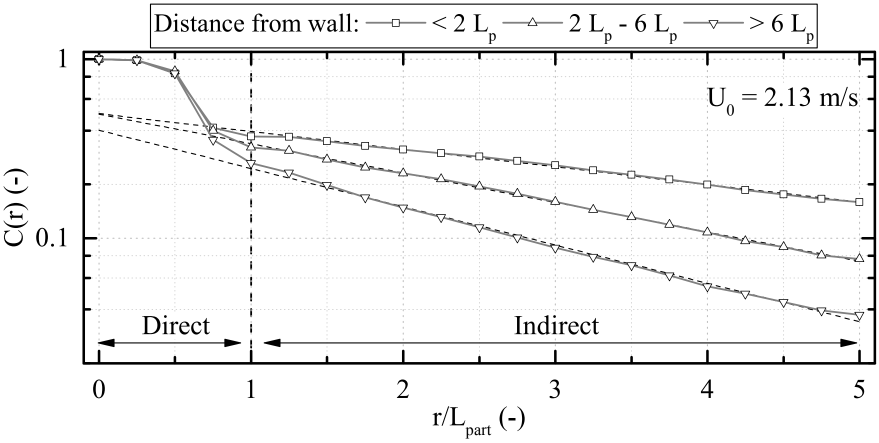

Figure 2.24: Spatial autocorrelation results of the orientation of particles seen directly through the front wall for the large bed at $U_0 = 2.13$ m/s. Symbols with grey solid lines represent measured data, dashed lines show the fitted exponential decay

2.3.10 Particle coordination number

Figure 2.25 shows the average particle coordination number as a function of the average vertical velocity in the frame. The coordination number (CN) is defined here as the number of neighbours in a $2L_p \times 2L_p$ area around the particle. The large bed was divided into four 15×15 cm sections (extending from the wall to the centre of the bed and up to 60 cm height). Recordings were made at $U_0 = 2.5$ m/s and $U_0 = 3.0$ m/s, 15,000 frames were captured for each height in the bed.

At the lowest position, velocities are small (as also shown by PIV measurements) and the particles are generally densely packed. At the higher positions, a proportional relationship between CN and velocity is observed. It can also be seen that the distribution of velocities is not symmetric around zero. This means that the particles move up relatively slowly in the densely packed regions, and then rain down faster in the dilute regions. See Figure 2.11 for a qualitative picture of why these trends are seen.

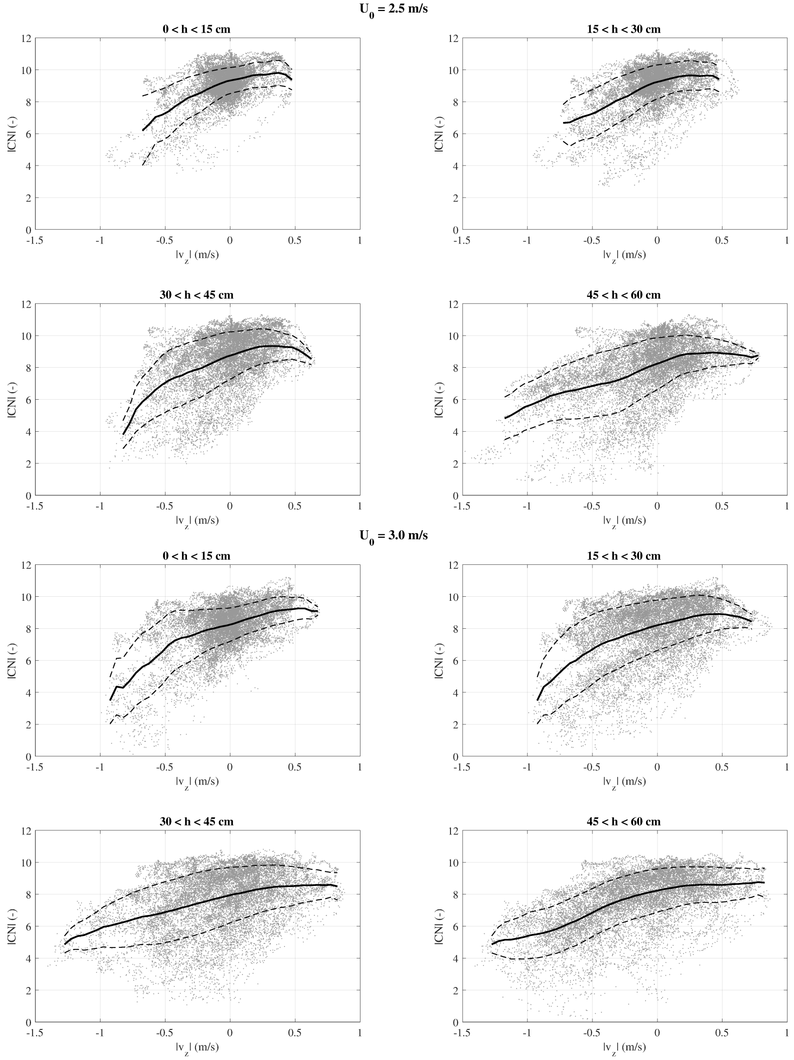

Figure 2.25: Average particle coordination number as a function of average vertical velocity, obtained from PTV measurements in the large bed at U_0 = 2.5 m/s (top) and U_0 = 3.0 m/s (bottom). Points indicate individual frames, solid line gives the running average, dashed line shows the standard deviation.

When comparing the results at the two different flow rates, it is observed that at the higher flow rate, the velocity distribution is broader and the coordination number is generally slightly lower. This is in line with the observed break-down of the interlocking particle structures at high gas velocities.

2.4 Conclusions and outlook

In this study, the fluidization behaviour of elongated particles characterized as Geldart-D has been investigated experimentally. Pressure drop and bed height measurements in two different sized set-ups have shown that, based on gas velocity, different regimes can be defined. At low gas velocity, the particles are packed, but as the flow rate increases, channels form. First, there is so-called passive channelling, meaning that no particles move through the channels. In the large set-up, at slightly higher gas velocity, active channelling was observed, with particles flowing through the channels and forming fountains. Finally, well above the minimum fluidization velocity, the particles show bubbling fluidization. Even at the highest flow rates, particles show interlocking behaviour, moving in large packed groups. It was demonstrated with experiments of two different sizes of rod-like particles and spherical particles that the behaviour described above is entirely an effect of particle shape, rather than particle size or material.

A Digital Image Analysis algorithm has been developed to analyse the orientation of particles. It was shown that at low gas velocity, particles prefer to lie down horizontally, while at high flow rate the particles align themselves along the flow direction. A spatial autocorrelation analysis has been performed to investigate the coalignment of particles. The orientation correlation decays exponentially at distances larger than particle length. At low flow rates (channelling regime), there is a strong correlation near the walls and a very weak correlation in the bulk. At higher flow rates (bubbling fluidizaton) the correlation length is not dependent on position in the bed, and slowly decreases with increasing flow rate.

Particle Image Velocimetry (PIV) has been applied to study the solid phase velocity and mass flux in the bed. A void fraction calculation algorithm based on CFD-DEM simulation data is used to obtain 3D void fractions. At sufficiently high flow rates, a circulation pattern similar to what is commonly observed for spherical particles is found. Particles generally move up through the centre of the bed, and come down along the walls. To gain knowledge on individual particles, Particle Tracking Velocimetry (PTV) has been used. By analysing the number of nearest neighbours (coordination number) for each particle, it was shown that particles tend to move up slowly in densely packed groups and rain down faster in dilute regions.

It is also possible to measure rotational velocities of the non-spherical particles. However, there are a few difficulties in doing this. Due to the nature of fluidization of elongated particles, we see particle-particle interaction as a dominant factor, as also observed for other dense gas-solid system. This leads to bulk behavior *i.e.* blocks of particles moving together, demonstrated by our PTV results. This leaves a low amount of rotational freedom, rendering this analysis unattractive. To be able to measure the rotational velocity it is important to sample sufficiently long trajectories. However, it is highly unlikely that individual particles stay and rotate in the plane parallel to the front wall. Also, particles are in the captured frame only for a very short amount of time especially for particles that are raining down.

Results on particle orientation and co-ordination numbers from this experimental study can have significant implications for both particle-scale and laboratory-scale numerical studies. In the case of particle-scale simulations, using a direct numerical simulation (DNS) such as the lattice Boltzmann method (LBM) (Sanjeevi and Padding, 2017), the choice of particular arrangements, in terms of volume fraction of particles and relative orientation to a fluid flow, will directly influence the measured hydrodynamic response. Experiments can be used to dictate the choice of particle arrangements to ensure that simulations consider arrangements that are representative of real fluidized systems. At the laboratory scale, where particle dynamics can be simulated using a CFD-DEM approach (Mema et al., 2019), experimental data sets such as those presented in this study are invaluable with regards to validating and adjusting simulations. Given the anisotropic geometry of the particles in this study, hydrodynamic forces other than drag such as torque and lift are of relevance. Simulation output for various hydrodynamic relations included in CFD-DEM simulations can be compared with experiments to test the validity of these relations.

Chapter 3

CFD-DEM Model

3.1 Introduction

Simulations that approximate particles as spheres cannot precisely predict the behaviour of real, complex shaped particles as encountered in e.g. biomass processing. Non-spherical particles are known to produce intermittent flow and dilute packing fractions as compared to spheres. They tend to result in larger fluidized bed voidages and larger minimum fluidization velocities due to interlocking of particles (Kodam et al., 2010). Information related to the influence of particle shape is therefore important, for example for reactor design and optimisation. Hence, there is a need to perform detailed particle-resolved simulations of fluidized beds consisting of non-spherical particles.

A detailed insight into particle and gas motion in the bulk region of the bed can be obtained from simulations. The coupled Computational Fluid Dynamics (CFD) - Discrete Element Method (DEM) approach combines discrete particle tracking with continuum modelling of the fluid. This approach generates detailed transient information such as the trajectories and orientation of particles and forces and torques acting on individual particles, which is extremely difficult, if not impossible, to obtain experimentally. Such information is important to understand the fundamentals of particle-fluid interactions in dense flows. This approach has been extensively employed to simulate systems with particle-fluid interactions (Tsuji, Kawaguchi, and Tanaka, 1993; Deen et al., 2007).

However, simulating non-spherical particles can be extremely complex and difficult for representing shape and detecting their contacts in the DEM system. Moreover, rep-

---

This chapter is based on **Mahajan, V. V.**, Nijssen, T. M., Kuipers, J. A. M. and Padding, J. T., *Non-spherical particles in a pseudo-2D fluidized bed: Modelling study*, Chemical Engg. Science **192**, 1105-1123 (2018).

resentation of the interaction between non-spherical particles and fluid increases complexity of data transfer between the CFD and DEM parts. At the same time, determining accurate fluid-particle interaction forces based on local orientation of particles while accounting for local voidage can be extremely challenging.

In the past 10 years, even more so than experimental studies, numerical methods have been employed to study non-spherical particle fluidization. Zhong et al. (2009) investigated cylindrical particles approximated through clustered spheres with the CFD-DEM. Ma, Xu, and Zhao (2017) performed CFD-DEM simulation of rod particles in a fluidized bed using super-ellipsoids. They investigated the orientation effects for different aspect ratio and gas inlet velocities. Zhou et al. (2011a), Gan, Zhou, and Yu (2016), and Zhou et al. (2011b) simulated ellipsoidal particles in a fluidized bed and demonstrated the effect of shape and particle aspect ratio on minimum fluidization velocity of such particles. Spherocylinders have been previously studied for the influence of particle aspect ratio on flow behaviour and packing (Langston et al., 2004; Zhao et al., 2012). Ren et al. (2014) performed simulations of spouting bed of rod like particles. Other studies of non-spherical gas-solid systems using CFD-DEM include pneumatic conveying (Hilton, Mason, and Cleary, 2010; Oschmann, Hold, and Kruggel-Emden, 2014) and fixed beds (Vollmari et al., 2015).

There is a large amount of literature on DEM methods that can realise arbitrarily-shaped particles while at the same time being fast, efficient, robust and accurate (Kodam et al., 2010; Pournin et al., 2005). There is increased interest in the implementation of complex shaped particles (Podlozhnyuk, Pirker, and Kloss, 2017). Lu, Third, and Müller (2015) made a comprehensive summary of recent developments of the DEM, including a variety of methods used for simulating non-spherical particles. A detailed overview of major DEM applications can be found in literature (Zhu et al., 2008). Among these methods to represent complex particle shapes the most popular is the glued sphere approach, whereby the particle is approximated by a certain number of spheres with overlap. A higher number of spheres results in a more accurate shape representation, but at the expense of computational time. A trade-off between robustness of the method in representing different shapes, accuracy of contact detection and overall efficiency has to be made.

An important aspect of CFD-DEM simulations is an accurate estimation of the drag force acting on the particle. A number of drag closures are available in literature for spherical particles. However, there are very few drag correlations available for non-spherical particles. Hölzer and Sommerfeld (2008) proposed a drag force model for single, complex shaped particles. In literature, this model is used in combination with a model of Di Felice (1994) to account for the effect of surrounding particles on the drag force. A number of researchers have followed this approach for simulating fluidized beds with CFD-DEM and demonstrated that the overall bed hydrodynamics can be fairly well predicted (Vollmari, Jasevičius, and Kruggel-Emden, 2016; Hilton, Mason, and Cleary, 2010). Zhou et al. (2011a) simulated ellipsoidal and oblate particles, Ren et al. (2014) simulated a spouted bed of corn-shaped particles, while Hilton and Cleary (2011) simulated a fluidized bed using superquadrics representing four types of complex shaped particles. A detailed summary of these works can be found in the paper of Zhong et al. (2016).

3.2 Model framework

The modelling done in this work is performed using a combined CFD-DEM method. A modified version of the CFDEM code is used to perform the simulations. The DEM framework, based on LIGGGHTS® (Kloss et al., 2012), handles all particle-particle and particle-wall interactions in a Lagrangian manner. Meanwhile, the CFD code based on OpenFOAM® (OpenCFD, 2004) and CFDEM®coupling (Goniva et al., 2012) solves the gas flow through the particle bed in an Eulerian way and couples this flow to the particles. It should be noted that the gas flow is resolved on a grid larger than the particle size. Using this combined simulation method and parallel computing, it is possible to gain accurate information on both particle movement and gas flow in a lab-scale fluidized bed, while still maintaining manageable computational times. Each of these models are described in detail below.

3.3 Discrete Element Method

DEM is used to describe the interaction of spherocylinders with rotational and translational degrees of freedom. A soft contact model, first introduced by Cundall and Strack to describe interactions between spherical granular particles, is used in this work (Cundall and Strack, 1979). The individual particles are tracked and their trajectories are numerically integrated over time. The local contact forces and torques develop when the adjacent particles spatially overlap. Consider a spherocylinder p in a dense environment of similar spherocylinders. The translational motion for spherocylinder p can be calculated by integrating

$$m_p \frac{d\vec{v}_p}{dt} = \vec{F}_{p,c} + \vec{F}_{p,b} + \vec{F}_{p,\nabla p} + \vec{F}_{p,f\rightarrow p} \tag{3.1}$$

where $\vec{F}_{p,c}$ is the contact force due to collision, $\vec{F}_{p,\nabla p}$ represents the pressure gradient (buoyancy) force acting on the particle and $\vec{F}_{p,f\to p}$ is the total interaction force exerted by the fluid phase on the particle which is further explained in section 3.5. The pressure gradient force $\vec{F}_{p,\nabla p}$ is evaluated as $-V_p \nabla p$. Here V_p is the particle volume and ∇p is the pressure gradient in the fluid phase. Gravity is accounted for in the body force $\vec{F}_{p,b}$. The rotational motion of particle p is calculated by integrating

$$\vec{\vec{I}}_p \cdot \frac{d\vec{\omega}_p}{dt} = \vec{T}_p \tag{3.2}$$

where $\vec{\vec{I}}_p$, $\vec{\omega}_p$ and $\vec{T}_p$ are the moment of inertia tensor, angular velocity and torque for particle p, respectively.

3.3.1 Contact model

We focus on accurate contact resolution for spherocylinder particles, while keeping the computational load minimal. A spherocylindrical particle can be represented in the model via a glued sphere approach. However, that is a method based on approximations, which may introduce new errors itself (Kruggel-Emden et al., 2008). A brief summary of DEM contact detection methods from literature with associated advantages and disadvantages is given in the Table 3.1.

Most of these methods are applicable to variety of particle shapes. Although these methods are versatile, these implementations come at the cost of accuracy and computational time. We keep the level of complexity to a minimum and choose to perform exact analytical calculations for the contact detection of spherocylindrical particles. In order to resolve the contact between particles and between particles and walls, a linear spring-dashpot model with rolling friction is used. The simple force models like linear spring-dashpot can be substituted for more accurate force models based on Hertzian force and contact volume calculations, if bulk properties only are of interest as opposed to detailed contact information such as contact area or contact duration (Kumar et al., 2018).

In the case of spherical particles, particles overlap when the distance between the particle centres is less than the sum of the particle radii. For spherocylindrical particles, the identification of contacts between particles, and the subsequent calculation of the overlap region is more complicated. Two adjacent spherocylinder particles are deemed to be overlapping once the distance between their central shafts is smaller than the sum of their radii. The only requirement for this contact is the determination of the closest

Table 3.1: Review of DEM contact detection methods.

#	Method	Advantages	Disadvantages
1	Glued spheres (Guo et al., 2012a)	Easy implementation, versatile	No exact representation, dissipative and stiff contact, computationally expensive
2	Intersecting glued spheres (Ren et al., 2014; Zhong et al., 2009)	Easy implementation, high degree of versatility	Dissipative and stiff contact, computationally expensive
3	Superquadrics or superellipsoids (Podlozhnyuk, Pirker, and Kloss, 2017; Delaney and Cleary, 2010)	For symmetric geometric shapes	Contact computations cumbersome for particles with sharp edges
4	Discrete function representation (DFR) (Williams and OConnor, 1995)	More advanced version of superquadrics method w.r.t. particle shape modelling	Large memory allotted for sorting particle surface points, contact calculations expensive
5	Probability based methods (Jin et al., 2011)	Contact calculations simple	Contacts not actual, Suitable only for regular polygons
6	Method of potential particles (Houlsby, 2009)	Versatile w.r.t. particle shapes	Problem modelling tangential component during contact
7	GJK Algorithm (Wachs et al., 2012)	Versatile w.r.t. particle shapes	Slow compared to exact analytical calculation
8	Exact analytical contact calculation (Kodam et al., 2010)	Accurate and fast	Specific to particular shape

distance points on the shafts of the two particles.

A modified spherocylinder contact detection algorithm originally developed by Pournin *et al.* for granular flows has been used in this study (Pournin et al., 2005). The shortest distance points on the shafts $\vec{s}_i, \vec{s}_j$ are found using an improved version of the algorithm described by Vega and Lago (1994).

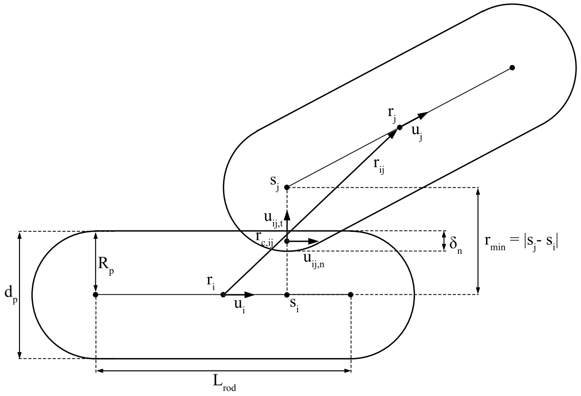

Figure 3.1: A schematic representation of two particles in contact.

Figure 3.1 shows an example of an overlapping contact between two spherocylinder particles P_i and P_j. For any particle, R_p is the characteristic radius or radius of the spherical part of the spherocylinder, $\vec{r}_i$ is the centre of mass, L_{rod} is the shaft length, $\vec{u}_i$ is the orientation unit vector originating at $\vec{r}_i$ and $\vec{v}_i$ is the translational velocity. λ and ψ are two arbitrary parameters for particles P_i and P_j which range in the interval $(-\infty, +\infty)$ such that when both λ and ψ are within range [-1,+1] the vector $\vec{r}$ in Eq. 3.5 connects the two finite rods. $\vec{s}_i$ and $\vec{s}_j$ are closest distance points and can be expressed as follows.

$$\vec{s}_i = \vec{r}_i + \lambda\, L_{rod}/2\, \vec{u}_i \tag{3.3}$$

$$\vec{s}_j = \vec{r}_j + \psi\, L_{rod}/2\, \vec{u}_j \tag{3.4}$$

In other words, λ and ψ values represent points on shafts for which the distance between two rods is minimum. For the sample contact illustrated in Figure 3.1, the shortest distance between the particles $|\vec{s}_j - \vec{s}_i|$, where $\vec{s}_i$ and $\vec{s}_j$ are points on the central axes of P_i and P_j respectively, is given by

$$\vec{s}_j - \vec{s}_i = \vec{r} = \vec{r}_{ij} + L_{rod}/2\,(\psi\,\vec{u}_j - \lambda\,\vec{u}_i) \tag{3.5}$$

where $\vec{r}_{ij} = \vec{r}_j - \vec{r}_i$ is the vector pointing from the center of particle P_i to the center of particle P_j. λ' and ψ' are the values minimizing Eq. 3.5 and are given by:

$$\lambda' = \frac{2}{L_{rod}} \frac{(((\vec{r}_{ij} \cdot \vec{u}_i) - (\vec{u}_i \cdot \vec{u}_j)(\vec{r}_{ij} \cdot \vec{u}_j)))}{((1 - (\vec{u}_i \cdot \vec{u}_j)^2))} \tag{3.6}$$

$$\psi' = -\frac{2}{L_{rod}} \frac{(((\vec{r}_{ij} \cdot \vec{u}_j) - (\vec{u}_i \cdot \vec{u}_j)(\vec{r}_{ij} \cdot \vec{u}_i)))}{((1 - (\vec{u}_i \cdot \vec{u}_j)^2))} \tag{3.7}$$

$$(\lambda, \psi) = \begin{cases} 1 & \text{for } (\lambda', \psi') \geq 1 \\ (\lambda', \psi') & \text{for } -1 < (\lambda', \psi') < 1 \\ -1 & \text{for } (\lambda', \psi') \leq -1 \end{cases} \tag{3.8}$$

An algorithm used for determining the closest distance points between the central axis of particles is given below:

- The positions ($\vec{r}_i$, $\vec{r}_j$) and unit orientation vectors $\vec{u}_i$, $\vec{u}_j$ of two particles under consideration are known. The closest point between the infinite lines is calculated via Eqs. 3.6 and 3.7.
- Rod P_i: λ check for bounds using Eq. 3.8. Evaluate $\vec{s}_i$ via Eq. 3.3. Find ψ with a perpendicular on Rod j from $\vec{s}_i$.
- Rod P_j: ψ check for bounds using Eq. 3.8. Evaluate $\vec{s}_j$ via Eq. 3.4. Find λ with a perpendicular on Rod i. Recheck Eq. 3.8.

After $\vec{s}_i$ and $\vec{s}_j$ are determined, the mid-point between these points is $\vec{r}_c$, the point of contact and the degree of overlap between the particles is expressed as δ_n. $\vec{n}_{ij}$ and $\vec{t}_{ij}$ are the normal and tangential unit vectors for the contact respectively. The contact force acting on a particle is the total of normal and tangential forces calculated as a result of overlap.

$$\vec{F}_{i,c} = \sum_{j \neq i} (\vec{F}_{ij,n} + \vec{F}_{ij,t}) \tag{3.9}$$

The normal contact force exerted on particle P_i by particle P_j is given by using a linear spring-dashpot model.

$$\vec{F}_{ij,n} = -k_n|\delta_{ij,n}|\vec{n}_{ij} + \zeta_n \vec{v}_{ij,n} \tag{3.10}$$

where k_n is the normal spring constant, ζ_n is the normal damping coefficient and $\vec{v}_{ij,n}$ is the normal relative velocity between the particles at the location of the contact point. The tangential contact force is calculated from the Coulomb-type friction expression

$$\vec{F}_{ij,t} = \begin{cases} -k_t|\delta_{ij,t}|\vec{t}_{ij} + \zeta_t \vec{v}_{ij,t} & \text{for } |\vec{F}_{ij,t}| \le \mu|\vec{F}_{ij,n}| \\ -\mu|\vec{F}_{ij,n}|\vec{t}_{ij} & \text{for } |\vec{F}_{ij,t}| > \mu|\vec{F}_{ij,n}| \end{cases} \tag{3.11}$$

In this expression k_t, δ_t, ζ_t, μ and $\vec{v}_{ij,t}$ are the tangential spring constant, tangential overlap, tangential damping coefficient, friction coefficient and tangential relative velocity respectively. δ_t is calculated from the time integral of the tangential relative velocity since the initial particle contact at time $t_{c,0}$. This expression represents the elastic tangential deformation of the particles since the onset of particle contact. Additional equations describing the contact model are given in Table 3.2.

Table 3.2: Equations for the contact model.

#	Parameter	Expression(s)
1	Point of contact	$\vec{r}_{c,ij} = \dfrac{\vec{s}_i + \vec{s}_j}{2}$
2	Normal overlap	$\delta_{ij,n} = d_p - |\vec{s}_i - \vec{s}_j|$
3	Tangential overlap	$\delta_{ij,t}(t) = \int_{t_{c,0}}^{t} \vec{v}_{ij,t} dt$
4	Relative velocity at contact point	$\vec{v}_{ij} = \vec{v}_j - \vec{v}_i + \vec{\omega}_j \times (\vec{r}_{c,ij} - \vec{r}_j) - \vec{\omega}_i \times (\vec{r}_{c,ij} - \vec{r}_i)$
5	Rolling torque (Wensrich and Katterfeld, 2012)	$\vec{\tau}_{ij,roll} = -\mu_{roll}|\vec{r}_i - \vec{r}_{c,ij}||\vec{F}_{ij,n}|\dfrac{\vec{\omega}_{ij}}{|\vec{\omega}_{ij}|}$

3.3.2 Contact parameters

The contact parameters are set based on the assumption of a maximum allowed overlap between particles to avoid unrealistic behaviour. A set of steps is followed to determine the contact parameters using the equations given in Table 3.3. This procedure is given as follows:

- Set the values for coefficient of restitution (e_n and e_t) obtained from experiments, assume $\delta_{max} \approx 0.01\, d_p$.
- Estimate maximum relative velocity δv_{max} from characteristic particle velocities.
- $k_{n,min}$ is estimated based on the potential energy stored in a spring and the amount of kinetic energy lost. $k_n\, \delta_{max}^2 = m_{eff}\, \delta v_{max}{}^2$
- Estimate duration of a binary contact t_c.
- k_t is estimated with orientationally averaged moment of inertia.
- Damping coefficients, η_n and η_t can be estimated. Orientationally averaged moment of inertia for spherocylinder is assumed to be an average over the moment of inertia along its three principle axes.

Table 3.3: Expressions describing the contact parameters (Pournin et al., 2005; Constatin, 2014).

#	Parameter	Expression(s)
1	Effective mass	$m_{eff,ij} = \dfrac{m_i\, m_j}{m_i + m_j}$
2	Contact time	$t_c = \left(\dfrac{m_{eff}}{k_n} \left(\pi^2 + \ln(e_n)^2 \right) \right)^{1/2}$
3	Normal damping coefficient	$\zeta_n = -\dfrac{2\, m_{eff}}{t_c} \ln e_n$
4	Tangential spring constant	$k_t = t_c^{-2} \left(\dfrac{1}{m_{eff}} + 2 \dfrac{(\vec{r}_c - \vec{r}_i)^2}{\langle I \rangle} \right)^{-1} \left(\pi^2 + \ln(e_t)^2 \right)$
5	Tangential damping coefficient	$\zeta_t = -2 t_c^{-1} \left(\dfrac{1}{m_{eff}} + 2 \dfrac{(\vec{r}_c - \vec{r}_i)^2}{\langle I \rangle} \right)^{-1} \ln e_t$
6	Moment of inertia	$I_{yy} = \pi \rho_p \left(\dfrac{1}{2} R_p^4 L_{rod} + \dfrac{8}{15} R_p^5 \right)$ $I_{xx} = I_{zz} = \pi \rho_p \left(\dfrac{1}{12} R_p^2 L_{rod}^3 + \dfrac{83}{240} R_p^5 + \right.$ $\left. \dfrac{4}{3} R_p^3 L_{rod}^2 + \dfrac{3}{4} R_p^5 + 2 R_p^4 L_{rod} \right)$ $\langle I \rangle_{orient} = \frac{1}{3} (I_{xx} + I_{yy} + I_{zz})$

In order to accurately model the particle-particle collisions in the bed, the coefficients of restitution (normal and tangential), and coefficients of friction (static and dynamic) need to be determined. These coefficients are determined from binary collision and sliding experiments.

Coefficient of restitution

In a binary collision, based on center of mass movement, the coefficients of restitution are defined as follows (Schwager and Pöschel, 2007; Kharaz, Gorham, and Salman, 2001), where v denotes the relative velocity between the two particles.

$$e_n = -\frac{v_{n,post}}{v_{n,pre}} \tag{3.12}$$

$$e_t = \frac{v_{t,post}}{v_{t,pre}} \tag{3.13}$$

As the coefficients of restitution depend strongly on material type, but only weakly on particle shape (Marhadi and Kinra, 2005), measurements were conducted using a flat plate and spherical particles of the Alumide material used in our fluidization experiments. A spherical particle of volume equivalent diameter was dropped onto the flat plate from a height of 20 cm. The plate was fixed on a rotating axis to allow for angled collisions. The collision was captured using a pco.dimax HD+ high-speed camera (approx. 1600 fps), as shown in Figure 3.2. Particle displacement between frames was used to determine velocity. Multiple (15) perpendicular collisions were captured, as well as 5 collisions per angle from 10 to 80 degrees at increments of 10 degrees. Measurements at 0-60 degrees were used to calculate e_n, 20-80 degrees were used for e_t.

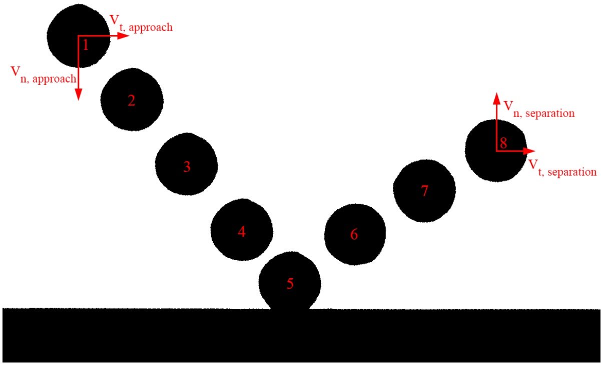

Figure 3.2: Particle-plate collision used to determine coefficients of restitution. Particle movement is shown over time (1-8). Vectors indicate velocities used in calculation of the coefficients.

Figure 3.3 shows the results from the particle-plate collision experiments. The error bars represent standard deviation. These measurements reveal that the restitution coefficient is approximately invariant to changes in the angle of collision for the angles

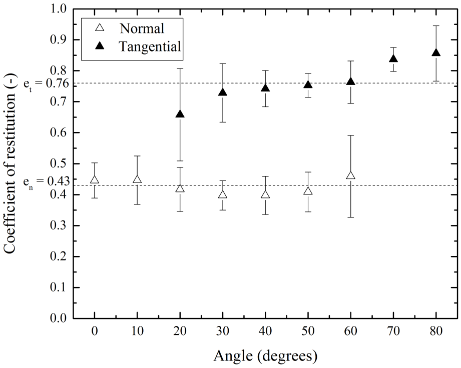

Figure 3.3: Measured coefficients of restitution for different angles. Error bars represent standard deviation, dashed lines represent mean values. There is no apparent relation between angle and coefficient of restitution.

investigated. The mean values found are $e_n = 0.43$ ($\sigma = 0.08$) and $e_t = 0.76$ ($\sigma = 0.10$).

Coefficient of friction

The dynamic coefficient of friction can be determined from the coefficients of restitution, as described by Kharaz, Gorham, and Salman (2001) and shown in Eq. 3.14, where μ_d is the dynamic coefficient of friction and θ the angle of impact.

$$\mu_d = -\frac{\partial(e_t)}{\partial((1+e_n)\cot(\theta))} \tag{3.14}$$

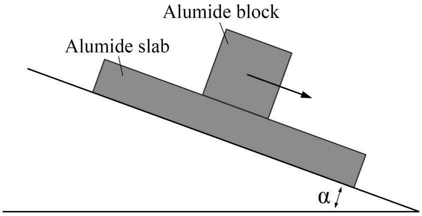

Figure 3.4: The setup used for determination of the static coefficient of friction.

The static coefficient of friction is determined from a sliding experiment. A block of the alumide material is placed on a slab of the same material. The angle of the slab is then slowly increased until the block starts sliding. A schematic representation of this setup is shown in Figure 3.4. The static coefficient of friction can then be calculated from the angle α at which the block starts sliding (Eq. 3.15, where μ_s is the static coefficient of friction, m is the mass of the block and g is gravitational acceleration). This experiment is repeated 50 times.

$$\mu_s = \frac{\sin(\alpha_{slab})mg}{\cos(\alpha_{slab})mg} = \tan(\alpha_s) \tag{3.15}$$

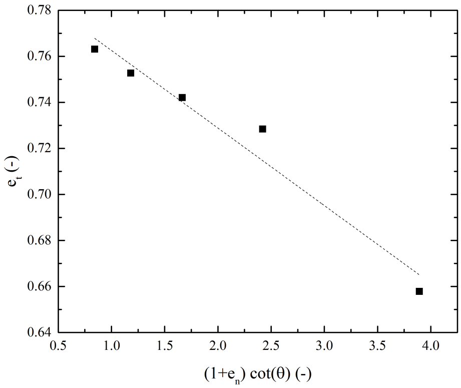

Figure 3.5: Determination of the coefficient of friction, according to Kharaz, Gorham, and Salman (2001).

Figure 3.5 shows the determination of the dynamic coefficient of friction. The resulting value is $\mu_d = 0.034$, with a coefficient of determination of $R^2_{adj} = 95\%$. From the sliding block experiments, a static friction coefficient of $\mu_s = 0.46$ ($\sigma = 0.06$) was found. The rolling friction value is chosen based on packed bed simulations. The value for which the simulated packed bed height is matches closely with the experimentally determined packed bed height is chosen as rolling friction value for fluidized bed simulations.

3.3.3 Neighbour list

To improve the performance of the DEM model, a neighbour list is used. In the neighbour list, the indices of particles surrounding a certain particle are stored so that contact calculations are only made with reference to these neighbouring particles. This neighbour list is then re-used for multiple time steps until the maximum displacement of the ends of a system particle has exceeded some prescribed limit and a new list must be built.

In order to further improve efficiency, an Oriented Bounding Box (OBB) (Ericson, 2005) is used. The bounding volume used to detect particles close to each other de-

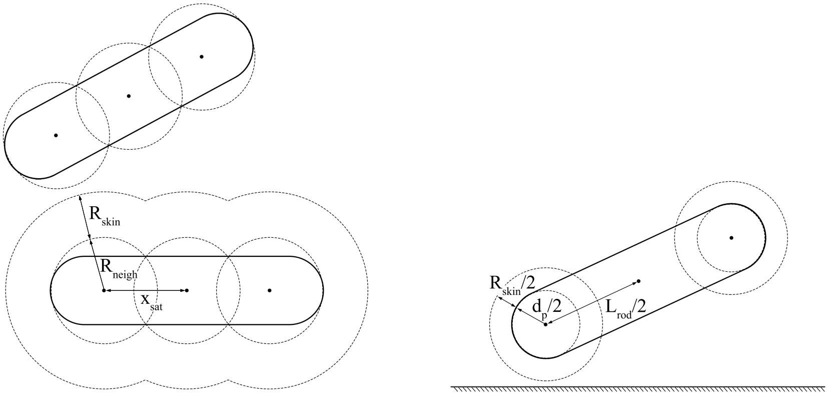

(a) (b)

Figure 3.6: Multi-sphere neighbourlist building method for (a) particle-particle contact and (b) particle wall-contact. x_{sat} and R_{neigh} are given by Eqs. 3.16 and 3.17 respectively.

pends on the orientation of both particles. In this study, a multi-sphere shaped bounding volume is applied. As shown in Figure 3.6a, a compound shape consisting of 3 spheres tightly surrounds the spherocylinder. The distance between the satellite points and the centre of mass (COM) x_{sat} is given by Eq. 3.16, which was derived from geometry. In addition to the sphere radius (Eq. 3.17), a skin of radius R_{skin} is used to guarantee the neighbour list can be used for multiple time steps. When the maximum displacement of each of two particle ends since the last neighbour list build surpasses $R_{skin}/2$, a new list is created. A similar approach is used to build the particle-wall neighbour list as shown in Figure 3.6b. Since the closest distance between a particle and a wall is always located at one of the tips of the particle, the spheres are only centred around the ends of the rod.

$$x_{sat} = \frac{1}{3}\left(-\sqrt{4d_p^2 + 2dL_{rod} + L_{rod}^2} + 2(d_p + L_{rod})\right) \tag{3.16}$$

$$R_{neigh} = \sqrt{\left(\frac{x_{sat}}{2}\right)^2 + \left(\frac{d_p}{2}\right)^2} \tag{3.17}$$

3.4 Computational Fluid Dynamics

3.4.1 Flow solver

The fluid phase is described in an Eulerian manner by imposing a mesh of equal sized cells on the fluidized bed. The PISO algorithm (Versteeg and Malalasekera, 1995) is used to solve the phase continuity and momentum transport equation for incompressible, Newtonian flow. Eqs. 3.18 and 3.19 are known as Model A in literature recommended by Zhou et al. (2011a) for dense gas-solid flows.

$$\frac{\partial(\epsilon\rho_f)}{\partial t}+\nabla\cdot(\epsilon\rho_f\vec{u}_f)=0 \tag{3.18}$$

$$\frac{\partial(\epsilon\rho_f\vec{u}_f)}{\partial t}+\nabla\cdot(\epsilon\rho_f\vec{u}_f\vec{u}_f)=-\epsilon\nabla p+\nabla\cdot(\epsilon\vec{\vec{\tau}}_f)+\epsilon\rho_f\vec{g}+\vec{f}_{p\rightarrow f} \tag{3.19}$$

where ϵ is fluid volume fraction, ρ_f is fluid density, $\vec{u}_f$ is fluid velocity and $\vec{\vec{\tau}}_f$ is the stress tensor. $\vec{f}_{p\rightarrow f}$ represents the momentum exchange between the fluid and particle phases. The volumetric force acting on the fluid phase due to particles and is given as

$$\vec{f}_{p\rightarrow f}=-\frac{\sum_{p,cell}^{n}\vec{F}_{p,f\rightarrow p}}{V_{cell}} \tag{3.20}$$

where $\vec{F}_{p,f\rightarrow p}$ is the force acting on an individual particle and n is the total number of particles in the CFD cell. The details of the transient solver with a PISO loop for pressure velocity coupling used in this work are given in the paper by Goniva et al. (2010).

3.5 Gas-particle coupling

The total fluid-particle interaction force $\vec{F}_{p,f\rightarrow p}$ includes the drag force $\vec{F}_d$. Often, the pressure gradient force is accounted in the drag closure and needs to be carefully checked before use (Tang et al., 2015; Vollmari, Jasevičius, and Kruggel-Emden, 2016). The most important contribution to the particle-fluid momentum exchange is given by the drag force depending on the local relative velocity between the fluid and the particle and granular volume fraction. Additionally, for non-spherical particles the orientation of the particle needs to be accounted for to accurately calculate drag. In view of these points, we present the drag models used in this work in the two following sub-sections: Section 3.5.1: Single particle drag models and Section 3.5.2: Voidage correction models.

3.5.1 Single particle drag models

Hölzer and Sommerfeld Drag

Hölzer and Sommerfeld (2008) derived an equation describing the drag coefficient for a single non-spherical particle in a gas flow (Eq. 3.21). Here ϕ is the particle sphericity, $\vec{v}_r$ is the relative velocity between the particle and the gas, A_e is the cross-sectional area of the volume equivalent sphere and $A_{p,tot}$ is the surface area of particle. This equation incorporates the orientation of the particle in the crosswise ($\phi_\perp$) and lengthwise sphericity ($\phi_\parallel$), given by Eqs. 3.23 and 3.24 respectively. These are calculated based on θ, the angle between the gas velocity vector and the particle orientation vector otherwise referred to as the incident angle or angle of attack.

$$C_{D0} = \frac{8}{\mathrm{Re}_p}\frac{1}{\sqrt{\phi_\parallel}} + \frac{16}{\mathrm{Re}_p}\frac{1}{\sqrt{\phi}} + \frac{3}{\sqrt{\mathrm{Re}_p}}\frac{1}{\phi^{\frac{3}{4}}} + 0.42\,10^{0.4(-\ln\phi)^{0.2}}\frac{1}{\phi_\perp} \tag{3.21}$$

$$\mathrm{Re}_p = \frac{\epsilon|\vec{v}_r|d_e\rho_f}{\mu_f} \tag{3.22}$$

$$\phi_\perp = \frac{A_e}{A_{p,\perp}} \text{ where: } A_{p,\perp} = \frac{\pi d_p^2}{4} + d_p L_{rod}\sin(\theta) \tag{3.23}$$

$$\phi_\parallel = \frac{2A_e}{A_{p,tot} - 2A_{p,\parallel}} \text{ where: } A_{p,\parallel} = \frac{\pi d_p^2}{4} + d_p L_{rod}\cos(\theta) \tag{3.24}$$

Figure 3.7 shows the single-particle drag coefficient as a function of Reynolds number, compared with single-particle Direct Numerical Simulation (DNS) results; the Zastawny model (Zastawny et al., 2012) extended for spherocylinders (Mema et al., 2017) and the Sanjeevi model (Sanjeevi, Kuipers, and Padding, 2018). It can be seen that the correlation by Hölzer and Sommerfeld shows some deviations from the DNS simulations for 0 degrees angle of attack at higher Reynolds number. It can also be seen that the particle orientation has large influence on the acting drag force and therefore fluidization of such non-spherical particles.

Sanjeevi Drag

A drag closure has been developed in-house using Lattice-Boltzmann (LB) simulations for a spherocylinder rod of aspect ratio 4 (Sanjeevi, Kuipers, and Padding, 2018). A

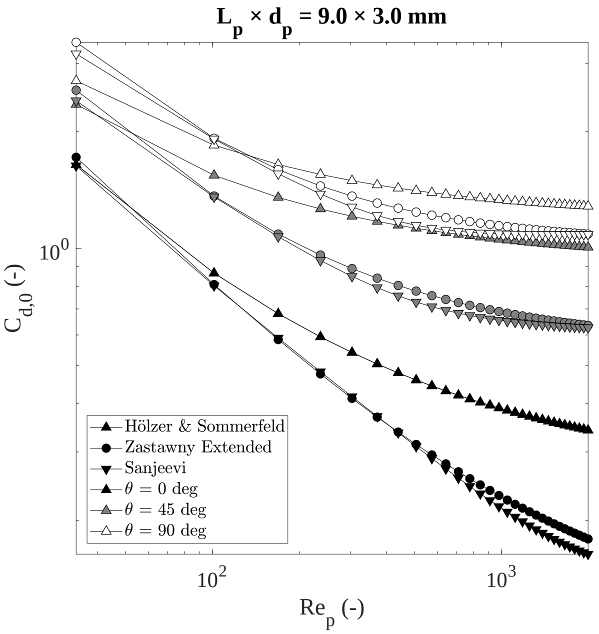

Figure 3.7: Single particle drag coefficient as a function of Reynolds number. The black, gray and hollow symbols represent 0°, 45° and 90° angle of attack respectively.

number of LB simulations were performed for different angles of attack and particle Reynolds number defined as $\mathrm{Re} = |\vec{v}_r| d_e \rho_f / \mu_f$. The coefficients are given in Table 3.4.

$$C_{D,\theta} = C_{D,\theta=0^\circ} + (C_{D,\theta=90^\circ} - C_{D,\theta=0^\circ}) \sin^2\theta \tag{3.25}$$

$$C_{D,\theta=0^\circ,90^\circ} = \left(\frac{a_1}{Re} + \frac{a_2}{Re^{a_3}}\right) e^{-a_4 Re} + a_5 (1 - e^{-a_4 Re}) \tag{3.26}$$

Table 3.4: The coefficients for the Sanjeevi drag correlation (Sanjeevi, Kuipers, and Padding, 2018).

	$\theta = 0^\circ$	$\theta = 90^\circ$
a_1	24.48	31.89
a_2	3.965	5.519
a_3	0.41	0.229
a_4	0.0005	0.0032
a_5	0.15	1.089

3.5.2 Voidage correction models

The drag force acting on a single particle in a gas flow is given by Eq. 3.27. It is crucial to take into account the effect of local voidage to determine the actual drag force acting on the particle.

Di Felice model

Di Felice (1994) developed a correlation describing the effect of local fluid volume fraction ϵ on the drag force (Eq. 3.28 and Eq. 3.29). Although not developed specifically for non-spherical particles, the Di Felice model is widely used to account for voidage effects (Nan, Wang, and Wang, 2016; Vollmari et al., 2015; Zhou et al., 2011a).

$$\vec{F}_{d0} = \vec{v}_r|\vec{v}_r|C_{D0}\frac{1}{2}\rho_g\frac{\pi}{4}d_e^2 \tag{3.27}$$

$$\vec{F}_d = \vec{F}_{d0}\epsilon^{2-\beta} \tag{3.28}$$

$$\beta = 3.7 - 0.65\exp\left(-\frac{(1.5-\ln \mathrm{Re}_p)^2}{2}\right) \tag{3.29}$$

Here ϵ is the local fluid volume fraction around the particle. Gidaspow (1994) recommends the use of the Ergun equation (Ergun, 1952) in dense regions, as it is derived for a dense, packed bed. Despite the fact that it was derived for isotropic-shaped solids, this equation also accurately describes the pressure drop over a bed of non-spherical particles, as will be shown in section 4.3.2. The drag force on a particle derived from the Ergun equation is given by Eq. 3.30. The smallest of the Di Felice and Ergun drag forces is used. Here ϕ is the particle sphericity, ν_f is the fluid kinematic viscosity and d_e is the volume equivalent particle diameter.

$$\vec{F}_d = \frac{\Delta P_{cell}}{L_{cell}}A_{cell}L_{cell}\frac{V_p}{V_{cell}}\frac{\epsilon}{1-\epsilon} = V_p\frac{\vec{v}_r\rho_f}{\phi d_e}\left(150\frac{\nu_f}{\phi d_e}\frac{1-\epsilon}{\epsilon}+1.75|\vec{v}_r|\right) \tag{3.30}$$

Tang and Tenneti models

Tang et al. (2015) and Tenneti, Garg, and Subramaniam (2011) proposed new correlations for static arrays of spheres. Extending the approach of Di Felice and in the absence of multi-particle drag data for non-spherical particles, we propose using these drag correlations to account for voidage effects as follows:

$$\vec{F}_d = \vec{F}_{d0}\, g(\epsilon, \mathrm{Re}_p) \tag{3.31}$$

where $g(\epsilon, \mathrm{Re}_p) = \vec{F}_d(\epsilon, \mathrm{Re}_p)/\vec{F}_d(\epsilon = 1, \mathrm{Re}_p)$ is the voidage correction factor while $\vec{F}_{d0}$ is given by drag equations evaluated for a single particle. The drag force expressions are given in Table 3.5.

Table 3.5: Expressions of drag force used for voidage correction.

Drag model	Expression(s)
Tang et al. (2015)	$F_d(\epsilon, \mathrm{Re}_p) = \dfrac{10(1-\epsilon)}{\epsilon^2} + \epsilon^2(1 + 1.5\sqrt{(1-\epsilon)})$ $+ \left[0.11(1-\epsilon)(2-\epsilon) - \frac{0.00456}{\epsilon^4} + \left(0.169\epsilon + \frac{0.0644}{\epsilon^4}\right)\mathrm{Re}_p^{-0.343}\right]\mathrm{Re}_p$
Tenneti, Garg, and Subramaniam (2011)	$F_d(\epsilon, \mathrm{Re}_p) = \dfrac{F_{isol}}{\epsilon^3} + F_\epsilon + F_{\epsilon,\mathrm{Re}_p}$ $F_\epsilon = \dfrac{5.81(1-\epsilon)}{\epsilon^3} + 0.48\dfrac{(1-\epsilon)^{1/3}}{\epsilon^4}$ $F_{\epsilon,\mathrm{Re}_p} = (1-\epsilon)^3\mathrm{Re}_p\left(0.95 + \dfrac{0.61(1-\epsilon)^3}{\epsilon^2}\right)$ $F_{isol} = \dfrac{\mathrm{Re}}{24}\left(\max(\dfrac{24}{\mathrm{Re}}(1.0 + 0.15\mathrm{Re}^{0.687}), 0.44)\right)$

Figure 3.8 shows the voidage correction factor as a function of void fraction and Reynolds number. The Tang and Tenneti models show stronger dependence on voidage compared to the model of Di Felice. This drastic change in voidage dependence can have significant impact on overall fluidization behaviour. Further, it can be seen that Di Felice model shows hardly any dependence on particle Reynolds number above 300. Rong, Dong, and Yu (2013) suggested an extension for Di Felice model. The voidage correction factor ($g(\epsilon)$) for the extended Di Felice equation showed relatively similar behavior to the original Di Felice model, when compared to other correction factors presented in this work. In order to avoid the redundancy of the results, we decided not to include the model by Rong et al. in the current investigation.

A comparison of the overall drag coefficient for different drag model combinations is shown in Figure 3.9. The comparison is done for two different particle Reynolds

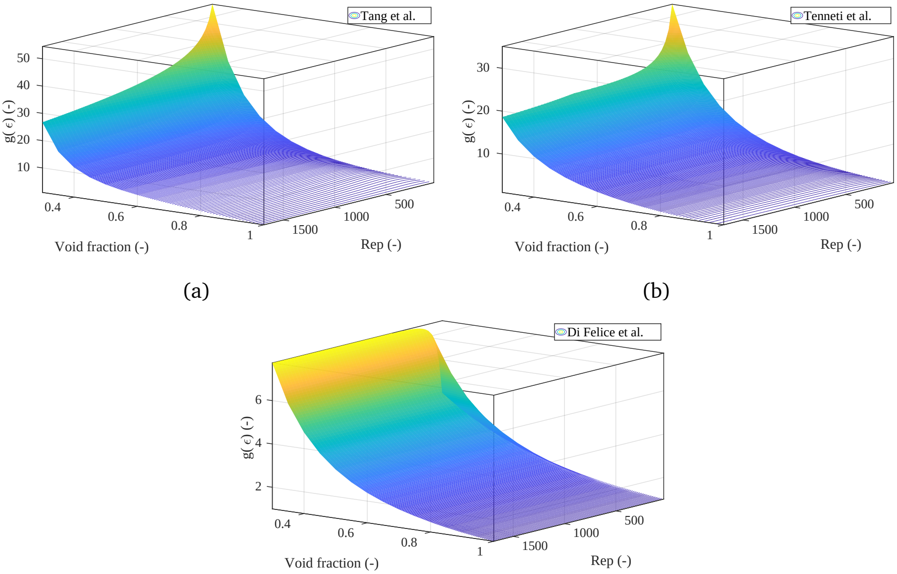

(a)

(b)

(c)

Figure 3.8: Voidage correction factor as a function of void fraction and Reynolds number for (a) Tang et al. (2015), (b) Tenneti, Garg, and Subramaniam (2011) and (c) Di Felice (1994) models.

number and a particle oriented at 45° relative to the flow. As discussed earlier, the Tang and Tenneti models with single particle drag are more sensitive to changes in Reynolds number and thus better suited for voidage corrections than the widely-used drag model of Di Felice model. Even then, it should be noted that one common limitation of all these models is that they have been developed for (mono-disperse) spheres, which are randomly arranged in space. To summarize, there are three models available which all take into account the voidage effect but which, on the other hand, do not consider non-sphericity of particles and heterogeneities with regard to particle arrangement or coalignment patterns.

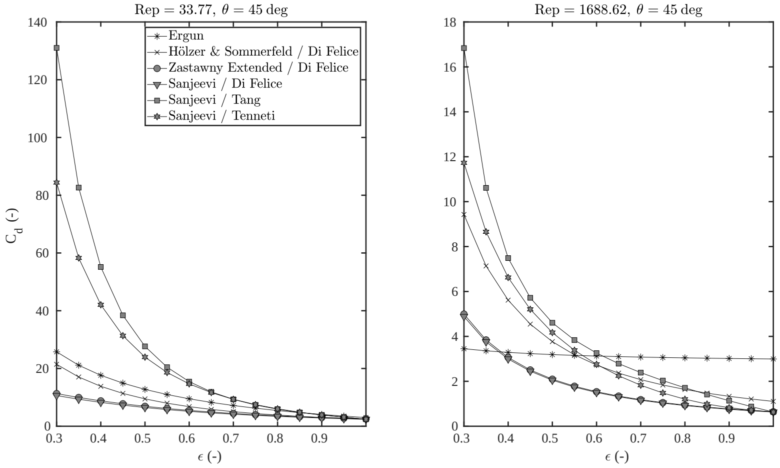

Figure 3.9: A comparison of drag coefficients for different drag models along with voidage correction as a function of void fraction. Plots are made for relative velocities of 0.1 m/s and 5.0 m/s giving an estimate for magnitude of drag coefficients at two different Reynolds number.

3.5.3 Void fraction calculation

The drag force depends on the local void fraction at each point in the bed. To attain these values, a distributed void fraction calculation is used, meaning that the volume of a particle is assigned to not one, but multiple cells when it crosses cell boundaries. The voidage calculation is performed on cells of same size as the CFD grid. Each particle possesses 16 satellite points, placed evenly in the complete particle volume as shown in Figure 3.10. Each cell containing such a satellite point is assigned a fraction of the particle volume, creating a more continuous void fraction field and preventing sudden jumps in local porosity.

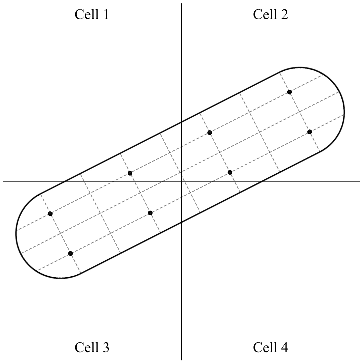

Figure 3.10: The particle volume is distributed among the cells according to the location of the 16 satellite points. Eight more points are located in the plane perpendicular to the shown cross-section.

Chapter 4

Model Validation

4.1 Introduction

The quality of a model can ultimately only be judged by comparing its predictions with careful experimental measurements. Vollmari, Jasevičius, and Kruggel-Emden (2016) validated their CFD-DEM model for the pressure drop and bed height for a number of irregularly shaped particles. Cai, Li, and Yuan (2012) numerically and experimentally studied the orientations of cylindrical particles in fluidized beds. While there are a number of studies on computational modelling of non-spherical particle fluidization, there are no detailed validation cases available in literature.

This chapter deals with detailed one-to-one comparison of simulations with experiments. In a semi-2D fluidized bed filled with spherocylindrical particles, pressure drop and bed expansion is measured as a function of gas flow rate. Particle orientation, circulation patterns and local particle dynamics in the bed obtained from simulations are compared with experimental measurements obtained from Digital Image Analysis (DIA), Particle Image Velocimetry (PIV) and Particle Tracking Velocimetry (PTV). We also compare the results of stacking of particles and coordination number with the experiments. The non-spherical single particle drag model of Hölzer and Sommerfeld (2008) is compared with a DNS drag model for spherocylindrical particle developed in-house. The results of proposed two new voidage correction models are compared with the widely popular model of Di Felice (1994).

This chapter is based on **Mahajan, V. V.**, Nijssen, T. M., Kuipers, J. A. M. and Padding, J. T., *Non-spherical particles in a pseudo-2D fluidized bed: Modelling study*, Chemical Engg. Science **192**, 1105-1123 (2018).

4.2 Simulation setup

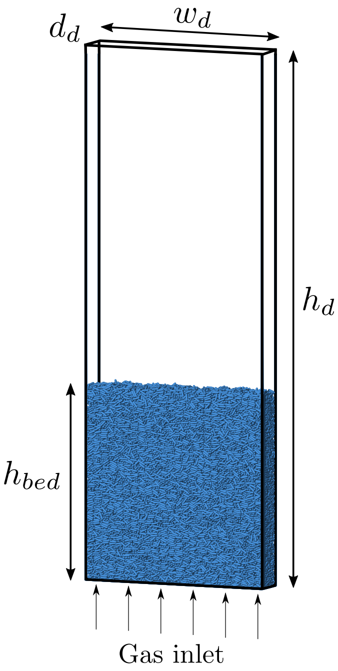

Figure 4.1: Schematic representation of the pseudo-2D fluidized bed setup used in this work, also showing the initial condition for all the simulations.

Simulations were performed to validate the CFD-DEM model for two fluidized beds (small and large), with their sizes given in Table 4.1. The simulations are done for three different drag models:

- Hölzer and Sommerfeld single particle drag with Di Felice model for voidage effects (HDF)
- Sanjeevi single particle drag with Tenneti model for voidage effects (STE)
- Sanjeevi single particle drag with Tang model for voidage effects (STA)

A schematic diagram of the setup is shown in Figure 4.1. The number of particles in the bed was calculated from the total bed mass measured experimentally (Mahajan et al., 2018b). All model parameters are listed in Table 4.1. Initially, a packing was generated by dropping randomly oriented particles into the bed under the influence of gravity. The bed height was verified for a number of different random particle orientations and a de-fluidized bed. The calculated bed height was the same for all initialisation methods, thus confirming an unbiased initial configuration. Gas was then introduced uniformly from the bottom to fluidise the bed. Simulations were run with superficial gas velocities starting from 0.2 m/s with 0.2 m/s intervals. The bed was allowed to attain a quasi-steady state (5 s), after which measurements were performed from 15 s. The boundary conditions used to solve the gas flow are given below.

- Inlet: fixed inlet superficial gas velocity ($\epsilon u_z = U_0$)
- Walls: no slip, no penetration ($u_x = u_y = u_z = 0$ m/s)
- Outlet: fixed outlet reference pressure ($P = 0$ Pa)

Table 4.1: Simulation parameters.

Parameter		Small scale	Large scale	Units
Domain height	h_d	1.0	2.0	m
Domain width	w_d	0.1	0.3	m
Domain depth	d_d	0.014	0.05	m
Particle length	L_p	6.0	$12.0 \cdot 10^{-3}$	m
Particle diameter	d_p	1.5	$3.0 \cdot 10^{-3}$	m
Particle density	ρ_p	1395	1395	kg/m^3
Number of particles	N_p	8070	32448	-
Initial bed height	h_{bed}	0.106	0.307	m
Coefficient of friction (P-P)	μ_{pp}	0.58	0.46	-
Coefficient of friction (P-W)	μ_{pw}	0.33	0.33	-
Coefficient of rolling friction	μ_{roll}	0.025	0.025	-
Coefficient of restitution	e	0.43	0.43	-
Normal spring constant	k_n	6000	6000	N/m
Time step DEM	t_{dem}	5×10^{-5}	s	
Time step CFD	t_{cfd}	5×10^{-4}	s	
Gas density	ρ_g	1.2	1.2	kg/m^3
Gas viscosity	η_g	$1.568 \cdot 10^{-5}$	$1.568 \cdot 10^{-5}$	Pa · s
Number of CFD cells (width)	$N_{cells,x}$	12	12	-
Number of CFD cells (depth)	$N_{cells,y}$	3	3	-
Number of CFD cells (height)	$N_{cells,z}$	120	120	-
Number of processors	N_{procs}	12	24	-

4.3 Results and discussion

In this section, the results obtained from the simulation of the small and large fluidized beds are presented. The results of particle orientation, particle co-ordination number and particle coalignment are presented only for the small bed.

4.3.1 Fluidization behaviour

The simulations are done using a wide range of superficial gas velocities from 0.2 m/s upto 2.6 m/s for the small bed and upto 3.2 m/s for the large bed. Over this range of gas velocities two regimes are observed:

- Packed bed: At flow rates below the minimum fluidization velocity (U_{mf}), particles are stationary. The gas passes through the voids barely moving the particles.
- Bubbling bed: At flow rates well above the minimum fluidization velocity, large pockets of gas move through the center of the bed and particles are thrown high in the freeboard region.

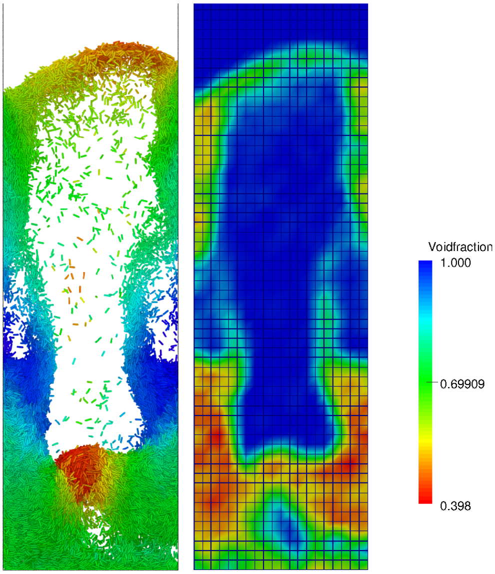

Figure 4.2: A simulation snapshot of fluidized bed showing particles colored according to z-velocity (left) and corresponding void fraction (right) for the large setup at $U_0 = 3.2$ m/s.

This behaviour is also observed in experiments as reported in Section 2.3 of Chapter 2. We do not observe a channelling regime in simulations. This is due to the inherent nature of the CFD-DEM modelling approach. In CFD-DEM simulations, the fluid cell size is usually 4 times larger than the volume equivalent particle diameter. This allows for accurate calculation of void fraction, but has the disadvantage that changes in local drag due to channel formation are not well captured. Figure 4.2 shows an instantaneous snapshot of fluidized bed simulation for large particles at $U_0 = 3.2$ m/s.

4.3.2 Pressure drop and bed height

The pressure drop is a key parameter for the characterisation of the fluidization behaviour of particles. The pressure drop found from simulations of the small and large beds are shown in Figure 4.3 and 4.4, alongside the experimental results for the same systems. Qualitatively, the pressure drop curves match their experimental counterparts very well.

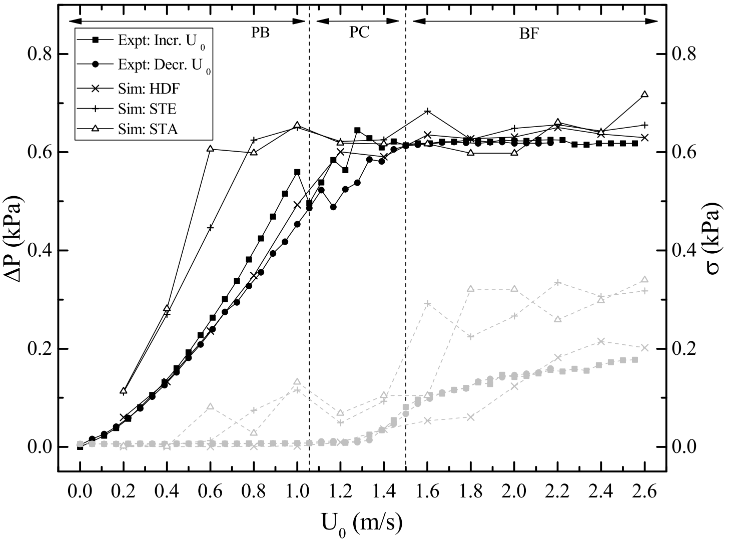

Figure 4.3: Comparison of the pressure drop from experiments and simulations in the small setup. Black symbols and left scale: average pressure drop. Grey symbols and right scale: standard deviation of the fluctuations in pressure drop.

In Figure 4.3, the pressure drop curve for the small bed for the Hölzer-Sommerfeld drag model shows a very good prediction. On the other hand, for the drag models of Tenneti and Tang, fluidization is achieved at gas velocities lower than in experiments. This is due to the strong dependence on voidage of these drag models as demonstrated in Section Gas-particle coupling.

In Figure 4.4, the pressure drop curve for the large bed for the Hölzer-Sommerfeld drag model shows an under-prediction, especially in the packed bed regime. This results in a higher minimum fluidization velocity than observed in experiments. In Section 3.5, it was shown that the Hölzer and Sommerfeld drag model does not under-predict the single particle drag coefficient. Therefore, the most probable cause for this discrepancy is the conversion from single particle drag to multi-particle drag. Contrary to the results for the small bed, for the large bed the pressure drop curves with the Tang and Tenneti drag models show a better prediction than the Hölzer-Sommerfeld model. One reason for this could be the relative accuracy of these drag models for different particle Reynolds numbers.

The bed height found from simulations of the small and the large cases are shown in Figure 4.5 and 4.6 respectively. The measurement of bed height was achieved using a

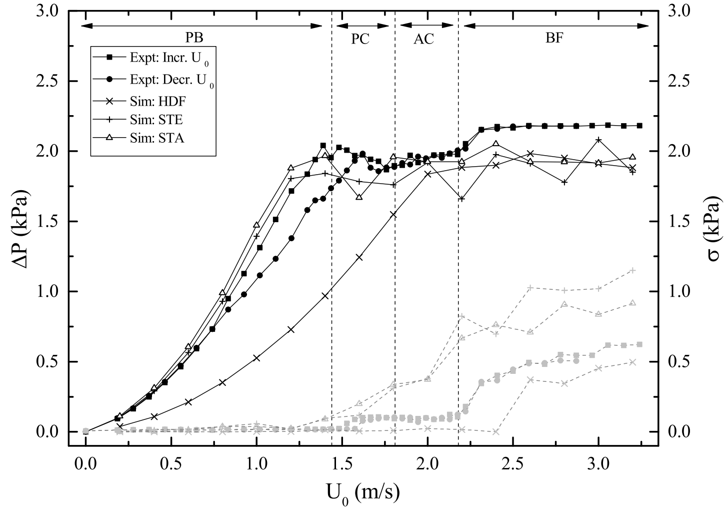

Figure 4.4: Comparison of the pressure drop from experiments and simulations in the large setup. Black symbols and left scale: average pressure drop. Grey symbols and right scale: standard deviation of the fluctuations in pressure drop.

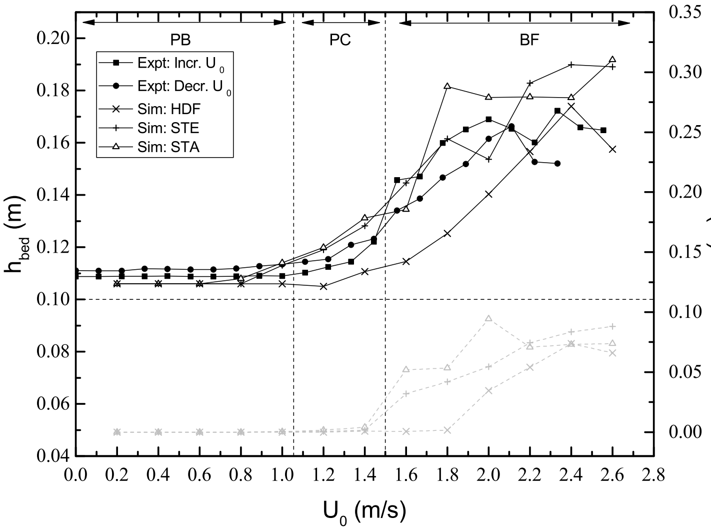

Figure 4.5: Comparison of the bed height from experiments and simulations in the small setup. Black symbols and left scale: average bed height. Grey symbols and right scale: standard deviation of the fluctuations in bed height (simulations only).

similar method as in experiments; by finding the maximum gradient in particle density. Similar to the pressure drop curves, the bed height curves qualitatively match their experimental counterparts very well. The most probable cause of quantitative mismatch is again the inaccurate representation of the effective drag acting on the particles.

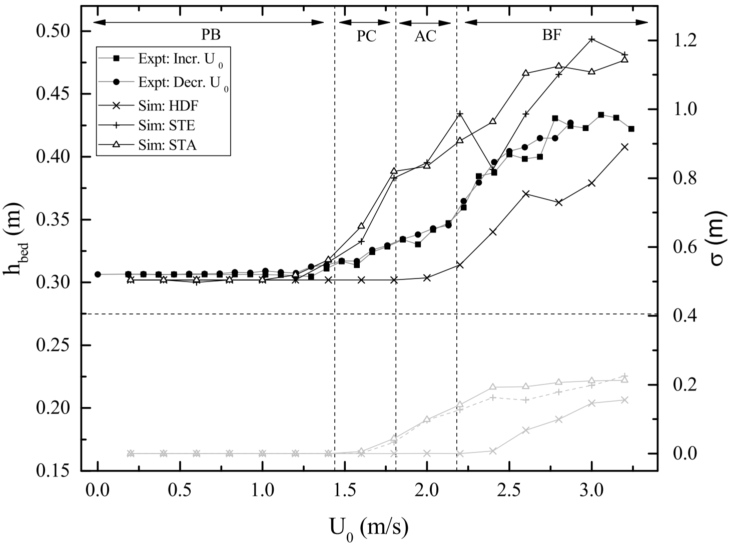

Figure 4.6: Comparison of the bed height from experiments and simulations in the large setup. Black symbols and left scale: average bed height. Grey symbols and right scale: standard deviation of the fluctuations in bed height (simulations only).

The other possible causes for the bed height mismatch are related to the contact model and the parameters, and is mainly of concern in the fluidized regime. The chosen inter-particle collision model accounts for particle penetration (overlap) based on distance but not based on the penetration (overlap) volume. This can cause inaccuracies in determination of the local voidage. Secondly, even though the contact parameters used in the model are based on experimental observations (see Section 3.3.2), this does not guarantee that the particle contact is captured realistically by the model. The DEM contact model, which is based on particle overlap, is different in nature from the true particle-particle and particle-wall contact, where particles deform and have an inherent surface roughness. For this reason, it is necessary to carefully tune the contact parameters (both for particle-particle and particle-wall contact) to equate the simulated bed height and experimentally obtained values. Additionally, the contact stiffness has been assumed to be constant while for spherocylinder particles, varying stiffness with transitions should be used according to the local geometry at the point of contact (Kumar et al., 2018; Kidokoro, Arai, and Saeki, 2015).

4.3.3 Mass flux

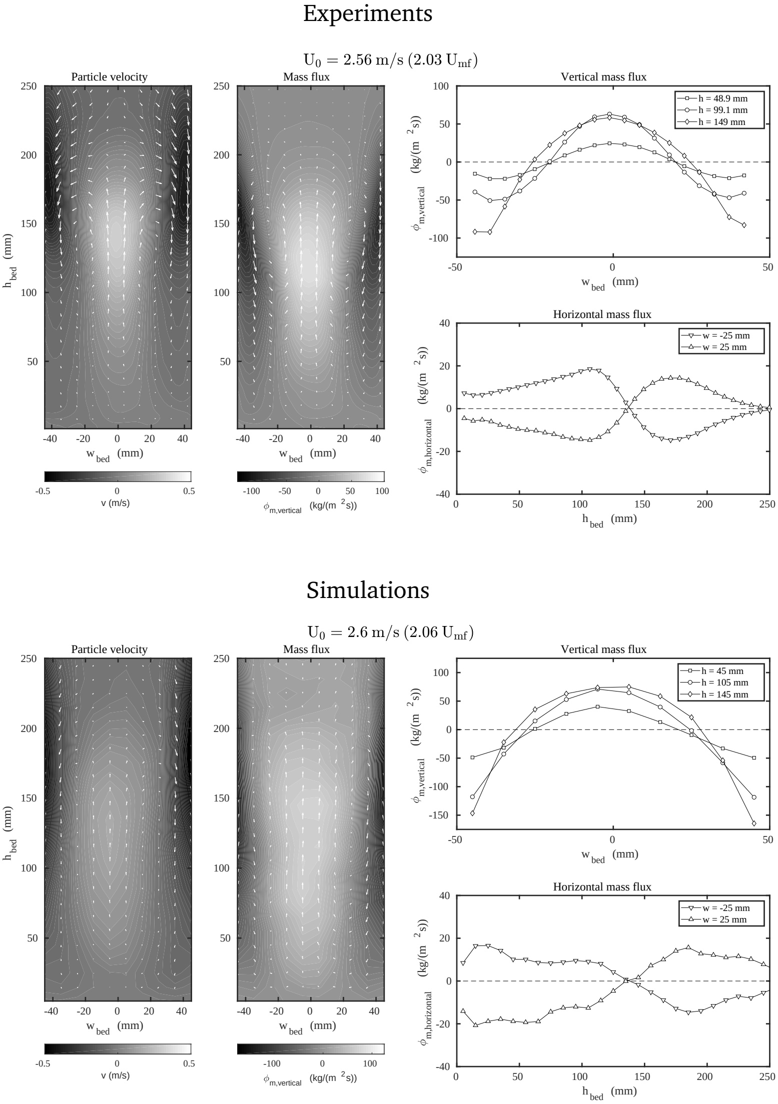

Figure 4.7: Particle velocity and mass flux from experiments in the small setup at $U_0 = 2.56$ m/s (top) and simulations of the small setup at $U_0 = 2.6$ m/s (bottom).

A comparison between mass flux and particle velocity results from experiments and simulations of the small and large bed is shown in Figures 4.7 and 4.8 respectively. The mass flux is extracted from simulation data by multiplying the solids volume fraction in each cell with the average velocity of all particles in that cell. This is expressed by $\langle \vec{\phi}_m \rangle = \langle \vec{v} \rho_p (1-\epsilon) \rangle$, where $\vec{\phi}_m$ is the local mass flux, $\vec{v}$ the particle velocity, ρ_p the particle density and ϵ the local void fraction.

Experiments and simulations show a good match for both large and the small bed. However, it is clear that in simulations, particles are much more mobile than in experiments, noted by the higher mass flux in both negative and positive direction. It is likely that this discrepancy is caused by the same reasons of sufficiently accurate drag and contact parameters mentioned earlier in Section 4.3.2. It was shown that both particle-particle contact parameters (especially coefficients of restitution and friction) (Goldschmidt, Kuipers, and Van Swaaij, 2001; Reuge et al., 2008) and particle-wall (Li et al., 2010; Ye, Van Der Hoef, and Kuipers, 2005) contact parameters can greatly influence the dynamics and solids mixing in fluidized beds. When particles are able to slide against each other more freely, bubbling is more vigorous, particles are thrown higher and solids mixing is faster.

4.3.4 Particle orientation

Figures 4.9 and 4.10 shows the probability density function (PDF) of the particle orientation from experiments and simulations respectively for the large setup at different flow rates. The PDF is given by Eq. 4.1, where $N_p(\alpha)$ is the number of particles at angle α.

$$PDF(\alpha) = \frac{N_p(\alpha)}{\int_{-90}^{90} N_p(\alpha) d\alpha} \tag{4.1}$$

Only particles close to and parallel to the front wall have been considered, to be comparable with the experimental results in Figure 4.9. Evidently, in simulations, particle do not align themselves with the gas flow at high flow rates. Particles remain predominantly horizontal, with a small peak emerging at an angle of 0° . When the PDF is parsed for different positions in the bed (Figure 4.10 bottom), it is clear that this peak is caused by interaction with the side walls. Similar results have been obtained by Oschmann, Hold, and Kruggel-Emden (2014).

The difference between particle orientation distributions may, in part, be attributed to the differing hydrodynamic forces experienced by particles in experiments and simulations. While spherocylindrical particles are inherently subject to drag, lift and torque in the laboratory-scale reactor, we consider only hydrodynamic drag forces in our simulations. Hydrodynamic torque is often considered to be negligible, given that gas density

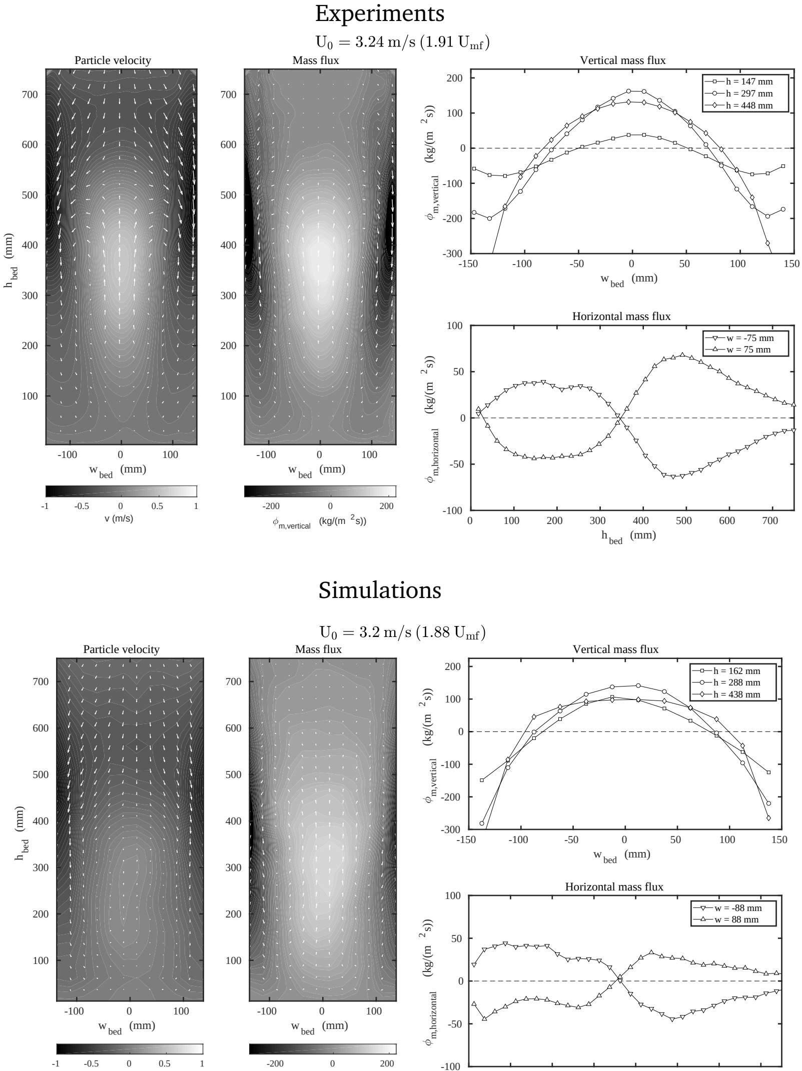

Figure 4.8: Particle velocity and mass flux from experiments in the large setup at $U_0 = 3.24$ m/s (top) and simulations of the large setup at $U_0 = 3.2$ m/s (bottom).

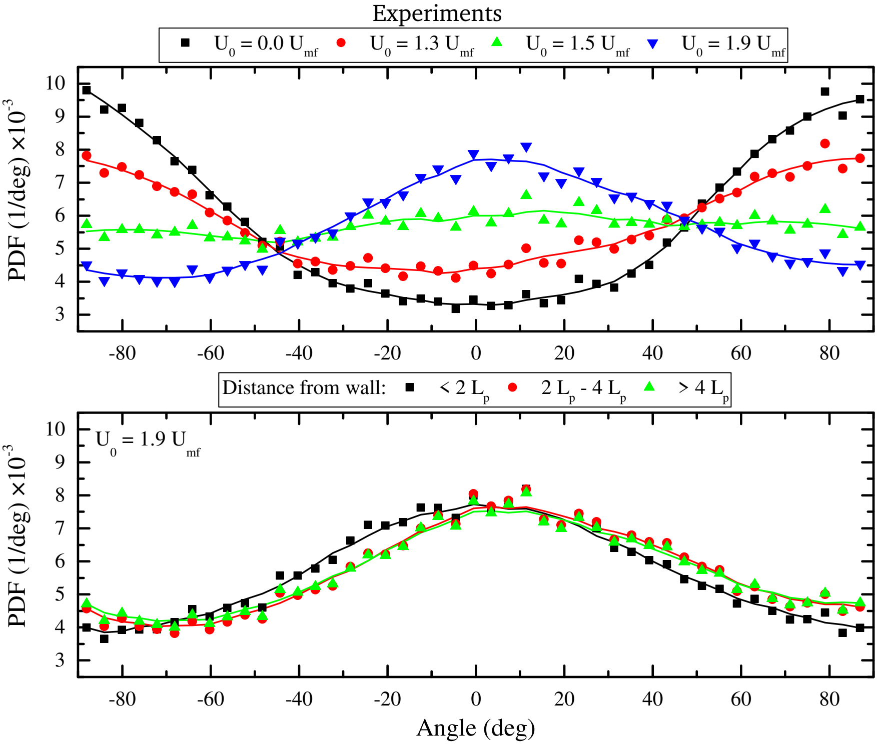

Figure 4.9: Probability Density Function (PDF) of the particle orientation (as observed from the front wall) in the large setup at different flow rates (top) and different positions in the bed (bottom, $U_0 = 1.9\ U_{mf}$). Angles of -90 and 90 degrees correspond with particles laying down horizontally, an angle of 0 degrees corresponds with particles standing up vertically (Mahajan et al., 2018b).

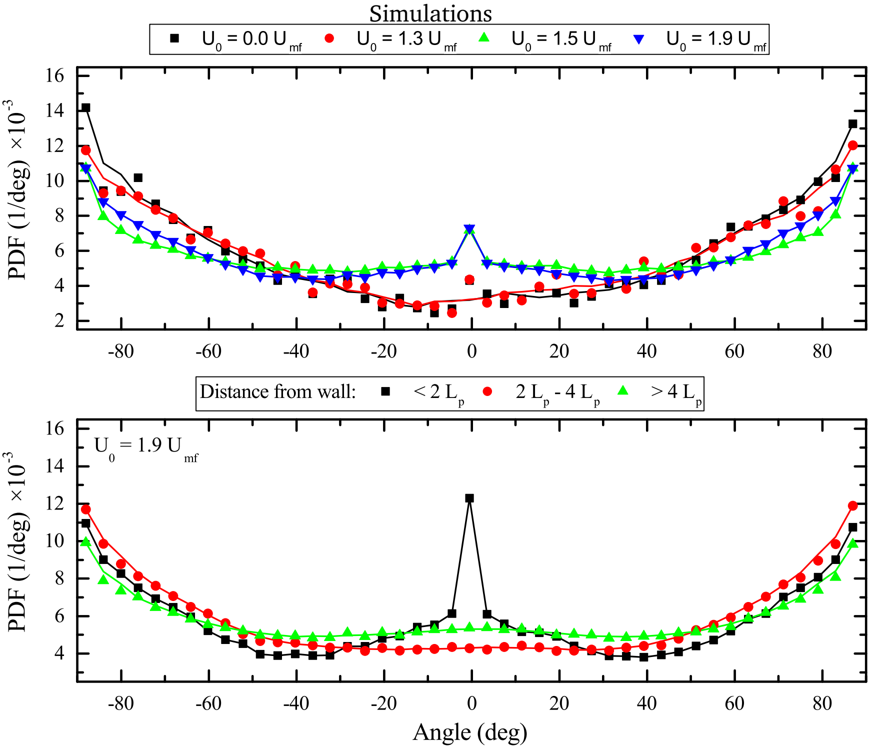

Figure 4.10: Probability Density Function (PDF) of the particle orientation from simulations of the large setup at different flow rates (top) and different positions in the bed (bottom, $U_0 = 1.9\ U_{mf}$). Angles of -90 and 90 degrees correspond with particles laying down horizontally, an angle of 0 degrees corresponds with particles standing up vertically.

is low and the particle mean free path between particle collisions is short (Radl, Girardi, and Sundaresan, 2012; Bernard, Climent, and Wachs, 2016).This assumption certainly holds for domains that have a large particle volume fraction i.e. in close proximity to the inlet of the reactor. However, in the upper domains of a reactor where particle volume fraction is comparatively lower, the trajectory of particles is likely to be more susceptible to the influence of the gas phase, and thus a particle can experience significant hydrodynamic torque and lift. As torque facilitates the rotation of a particle depending on its initial orientation to an incoming flow, the inclusion of torque in the simulations may more accurately capture particle orientations as observed in experiments.

4.3.5 Particle coalignment

Particle coalignment has been studied only for particles close to, and parallel to the front wall. Figure 4.11 shows the result of the orientation autocorrelation in the large bed from experiments and the simulations. The orientation autocorrelation value drops at a distance much less the particle length. Comparison shows a good quantitative agreement between simulation and experiment. However, the curves for experiments show little difference as a function of distance from the side walls. Contrary to this, in simulations although very small, a clear distinction is seen with respect to proximity to side walls, although this effect is very small. As discussed earlier, this might be due to the simplicity of our model i.e. neglecting hydrodynamic torque effects.

4.3.6 Particle coordination number

Since in simulations there is direct access to particle positions and velocities, it is straightforward to compare simulation data with results from experimentally determined PTV measurements. Figure 4.12 shows an example snapshot of the large bed with particles coloured according to their coordination number (CN). Figure 4.14 shows the average particle coordination number in a way analogous to the experimental results in Figure 4.13. As in the experiments, the height of the bed is divided into sections with height equal to half the bed width. In order to obtain the 2D CN that is measured using PTV, the 3D CN is divided by the number of particle layers in the cut-off radius.

From comparison of the figures, it is clear that both experimental and simulation results are in good agreement. In the lower section of the bed velocities are small and particles are densely packed, as also shown by Figure 4.14 (bottom) in the previous section. Higher in the bed, particles mainly move upwards in dense structures and rain down in dilute regions. The same observations were made in experiments (Figure 4.13).

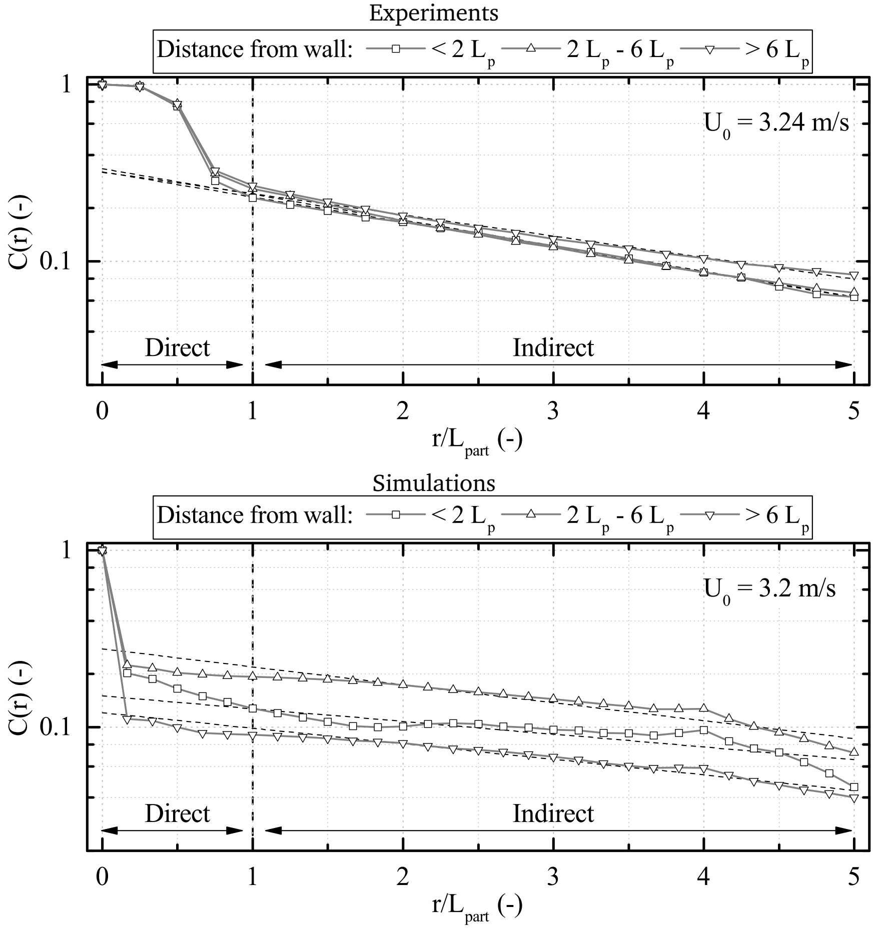

Figure 4.11: Spatial autocorrelation of the orientation of particles seen directly through the front wall for the large bed at U_0 = 3.24 m/s for experiments and at U_0 = 3.2 m/s for simulations.

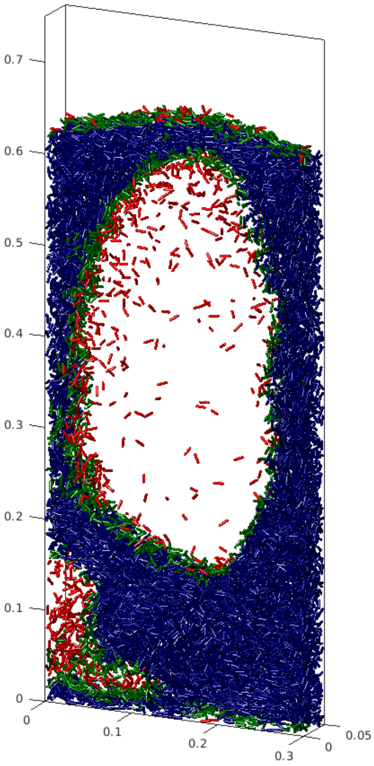

Figure 4.12: An example snapshot of particle coordination number, obtained from simulations in the large bed at $U_0 = 3.2$ m/s. The colors indicate the coordination number for the respective particles, blue: particles with 9 or more neighbours, green: 5 to 8 neighbours and red: less than 5 neighbours.

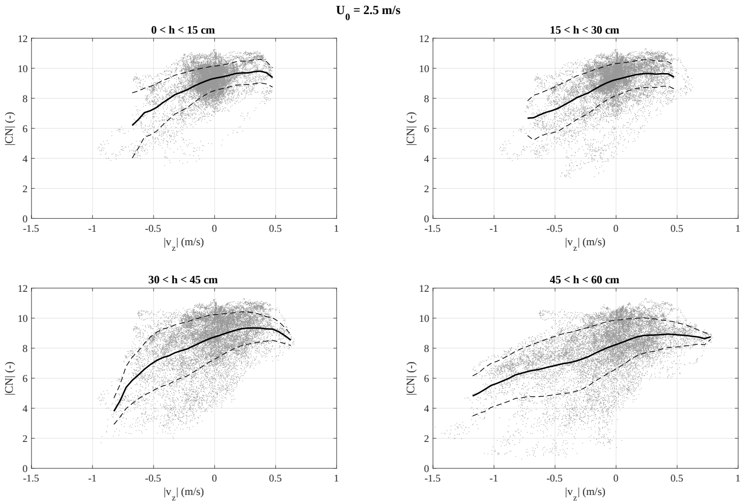

Figure 4.13: Average particle coordination number as a function of average vertical velocity, obtained from experimental PTV measurements in the large bed at U_0 = 2.5 m/s. Points indicate individual frames, solid line gives the running average, dashed line shows the standard deviation (Mahajan et al., 2018b).

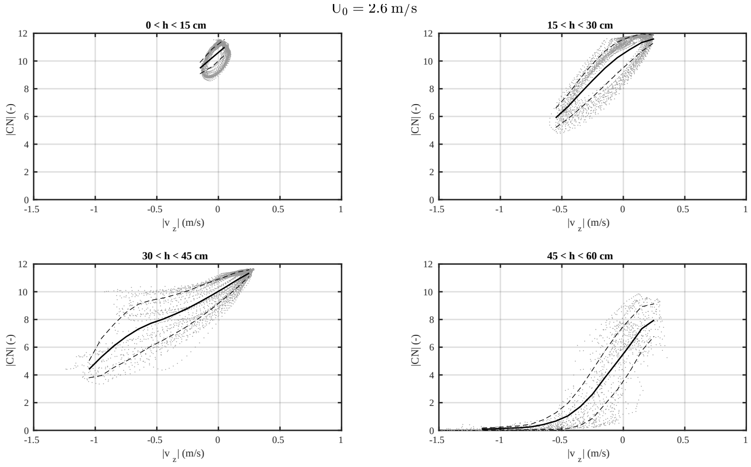

Figure 4.14: Average particle coordination number as a function of average vertical velocity, obtained from simulation of the large bed at U_0 = 2.6 m/s. Points indicate individual frames, solid line gives the running average, dashed line shows the standard deviation.

4.4 Conclusions and outlook

In this study, the fluidization behaviour of rod-like particles has been investigated numerically with the CFD-DEM approach and compared with experiments. A description of the model was given, focussing on the extensions developed in this study. An exact representation of particle shape through analytical calculation is used instead of a comparatively slow and inaccurate multi-sphere approach. The fluid forces acting on particles are calculated using particle orientation, shape and local void fraction. The bed behaviour is investigated at different gas inlet flow rates.

Comparison of experimental and numerical pressure drop and bed height results has been carried out for three different drag models in two differently sized beds. The results show good qualitative agreement. However, when compared quantitatively, the results show that the particle drag force is under-predicted in case of the combined Hölzer and Di Felice drag model while over-predicted in the other two cases. This is associated with the voidage correction term for the drag coefficient, which is based on data for spherical particles in absence of this information for spherocylindrical particles. A combination of single particle drag for orientation effects and multi-particle drag correlation of spherical particles for voidage correction clearly is not the most accurate approach. For more accurate results (also in the channelling regime), a multi-particle drag closure is needed. This drag closure should be derived from direct numerical simulations of same particle shape and size, in this case, spherocylinder particles aspect ratio 4 (Sanjeevi, Kuipers, and Padding, 2018). More importantly, such simulations should consider voidage, relative particle spacing, mutual particle orientation and particle Reynolds number as parameters. In addition, it could also take into account channeling within a single CFD cell.

Comparison of simulations with PIV and PTV experimental results shows that qualitatively the solids circulation pattern is well captured by the model. Comparison of the average particle orientation at different flow rates shows the importance of the hydrodynamic torque. In experiments, particles align themselves along the flow direction at high gas velocities. In simulations, this effect is not observed as particles remain predominately horizontally oriented. It was also shown that this observation is not an effect of particle-wall collisions but rather depends on the particle-gas interaction. In literature, the hydrodynamic torque is generally regarded as of very little influence, as gas viscosity is low and the mean free path between particle collisions is very short. However, our results suggest that the incorporation of hydrodynamic torque is necessary for accurate modelling of non-spherical particles.

The effects of lift forces and hydrodynamic torque are excluded in this work. The recent work by Mema et al. (2019) has shown that these forces cannot be neglected for rod-like particles. Inclusion of these additional forces should be considered for better prediction of non-spherical fluidized bed hydrodynamics. Furthermore, with this validation study, this CFD-DEM model can further be used to study the rheological behaviour of non-spherical particle suspensions. The DEM model can be used to measure and study the developed particle stresses. With a comprehensive study considering all the relevant parameters encountered for fluidized bed, a stress closure can be developed, which can be used in modelling particle stresses in a more coarse-grained model for industrial scale simulations.

Chapter 5

Rheology of inertial rods: effect of fluid medium

5.1 Introduction

Granular flows consisting of particles suspended in fluid are present everywhere in nature (rivers, sandstorms, landslides) and industry (cosmetics, detergents, paints and various fluids in the oil and mineral industries). Granular flows, particularly of solids dispersed in a continuous fluid phase (liquid or gas) exhibit a wide range of behaviour, including Newtonian, shear thinning, shear thickening and discontinuous shear thickening (Mari et al., 2014a). The behaviour of these materials under different conditions is still not well understood and therefore has been a topic of research for decades. Better understanding of the fundamental physics of inertial particle flows is necessary to control industrial processes and products.

Studying granular flows via experiments is a difficult and tricky process (Campbell, 1989). Rheometers are used to study suspensions, but only offer measurement of shear stress and total pressure in the system. Non-intrusive experimental techniques, which can improve our understanding of granular flow rheology, are rare. Also they only measure the combined macroscopic result of all the interactions and not the behaviour of individual particles on a microscopic level. Additionally, most suspension experiments reported in literature are performed on small particles in a liquid continuous phase, meaning that the particle inertia is relatively unimportant (very low Stokes number). In

---

This chapter is based on **Mahajan, V. V.**, Mehmood J., El Hasadi Y. M. F. and Padding, J. T., *Fluid medium effect on stresses in suspension of high-inertia rod-like particles*, Chemical Engg. Science X **3**, 100030 (2019) the past 40 years, the discrete element method (DEM), originally developed by Cundall and Strack (1979) for soft-sphere interactions, has been widely used to study granular systems in depth. This method offers many advantages over experimentation, like precise measurements of volume fraction, particle orientation and complete access to the stress tensor and residual kinetic energy of the system. DEM coupled with computational fluid dynamics (CFD) has been used extensively to understand a number of granular flows, encountered in shear flows, risers and fluidized beds (Campbell, 1989; Campbell and Gong, 1986; Deen et al., 2007; Mahmood and Elektorowicz, 2016). The CFD-DEM method, due to its ability to accurately deal with a variety of shapes, is also a popular method of choice to study granular flows of non-spherical particles (Mahajan et al., 2018a; Zhong et al., 2016).

On the other hand, to understand the rheology of dilute and dense granular flows, granular kinetic theory was developed based on the kinetic theory of dense gases by Chapman and Cowling (1970). Jenkins and Savage (1983) extended the kinetic gas theory to predict the collisional stresses in granular flows. Lun et al. (1984) improved on the theory presented by Jenkins and Savage. Their theory predicts not only collisional stresses but also kinetic stresses produced due to particle motion. Campbell and Gong (1986) performed 2-D numerical simulations, which were found to be in good agreement with the predictions by Lun et al. (1984). The most widely used kinetic theory models are developed for the flow of inelastic, smooth spheres excluding the effect of interstitial fluid (Fan, 1996; Garzó and Dufty, 1999). Kinetic theory models have been extended or modified to account for different particle properties (e.g. friction) and physical phenomena (e.g. long lasting collisions) (Campbell, 2002; Jenkins, 2006; Jenkins, 2007; Jenkins and Berzi, 2010; Chialvo and Sundaresan, 2013).

Another popular theory in literature to describe granular flows is $(\mu_{eff})(I)$ rheology (MiDi, 2004; Forterre and Pouliquen, 2008), which was developed in the mid 2000's. In this theory, constitutive equations, which describe the conservation laws of granular flows, are characterized by an inertial number, $I = \dot{\gamma}D/\sqrt{\frac{P}{\rho_p}}$, with $\dot{\gamma}$ the shear rate, D the particle diameter, P the particle pressure, and ρ_p the particle density. An important result of the theory is that the effective friction (μ_{eff}), which is the ratio of shear stress to the pressure, is a function of inertial number I. These functions have been determined by simulations (Jop, Forterre, and Pouliquen, 2006; Da Cruz et al., 2005; Hatano, 2007) as wells as by experiments (Fall et al., 2015; Jop, Forterre, and Pouliquen, 2005).

Most of the studies discussed above deal with circular disks in 2D or spheres in 3D, primarily because dealing with non-spherical particles in kinetic theory is not trivial. However, there is a recent increase in studies dealing with such particles. Researchers have performed experiments (Baosheng, He, and Zhong, 2010; Li et al., 2004) and simulations with other particle shapes. Simulations performed by Pena, Garcia-Rojo, and Herrmann (2007) for polygonal disks and by Cleary and Sawley (2002) for blocky particles show that particle shape has strong effects on the granular temperature and volume fraction in the core of the flow, both of which are smaller compared to volume-equivalent spherical particles. Moreover, particles with irregular shape (higher aspect ratio) are hard to shear due to interlocking of the particles. One of the main attributes of elongated particles is that they have a preferred alignment towards the main flow stream, as shown by Pena, Garcia-Rojo, and Herrmann (2007), Reddy, Kumaran, and Talbot (2009), and Reddy, Talbot, and Kumaran (2010) and Campbell (2011). Campbell (2011) found that for smooth frictionless ellipsoid particles, smaller stresses were observed when compared to volume-equivalent spheres. It was also found that large surface friction can lead to particle rotation which can block the flow leading to higher stress values. Guo et al. (Guo et al., 2012a; Guo et al., 2012b; Guo et al., 2013; Guo and Curtis, 2015) extensively studied the dry granular shear flow of rod-like particles of various aspect ratio, wet flexible fibers, flat disks and elongated rods in the presence and absence of friction. Nagy et al. (2017) have also performed a 3D simulation with spherocylindrical particles upto aspect ratio of 2.5. Their study demonstrated that $\mu_{eff}(I)$ rheology can be extended to non-spherical particles at high volume fractions. All of these studies exclude the effect of fluid on the developed stresses.

Guazzelli and Pouliquen (2018) explained, in a comprehensive paper on rheology of dense granular suspensions, that hydrodynamic interactions or lubrication forces between the particles are important in the dilute regime. At high concentrations they become less significant compared to direct particle contacts. Although in reality granular particles are usually surrounded by an interstitial fluid (like air) the influence of the latter on the dynamic properties of the solid particles is generally neglected in most theoretical and computational works. Needless to say, the effect of the interstitial fluid on solid particles turns out to be significant in a wide range of practical applications and physical phenomena (Xu et al., 2013; Chamorro, Reyes, and Garzó, 2015). Garzó et al. (2012) presented an Enskog kinetic theory for monodisperse gas-solid flows. Their theory demonstrates that the effect of the fluid phase on the constitutive equations for the solid phase shear viscosity is non-negligible. However, their theory, like most kinetic theories, is limited to spherical particles and therefore is not applicable to granular non-spherical particle suspensions.

While the majority of studies so far have focused on Stokes numbers, $St = \rho_p {d_p}^2 \dot{\gamma} / \eta_f$ (where $\dot{\gamma}$ is the shear rate, η_f the viscosity of the fluid phase, and ρ_p and d_p are the density and volume equivalent diameter of the solid particles, respectively) of the order of 1 or smaller, this chapter focuses instead on particle flows that have Stokes number and Reynolds number much larger than 1. The range of numbers is given in Table 5.1.

Dimensionless quantity		Range	
		Air	Water
Stokes number	$St = \rho_p {d_p}^2 \dot{\gamma}/\eta_f$	$O(10^2 - 10^5)$	$O(10^0 - 10^3)$
Reynolds number	$Re = \rho_f {d_p}^2 \dot{\gamma}/\eta_f$	$O(10^{-1} - 10^2)$	$O(10^0 - 10^3)$
Inertial number	$I = \dot{\gamma} d_p \sqrt{\rho_p/P}$	$O(10^0 - 10^1)$	$O(10^{-2} - 10^1)$
Viscous number	$I_v = \eta_f \dot{\gamma}/P$	$O(10^{-6} - 10^{-1})$	$O(10^{-4} - 10^1)$

Table 5.1: Range of dimensionless numbers for the simulations in this work.

Although such high Stokes and Reynolds numbers are encountered in a number of applications (a variety of chemical, pharmaceutical and process industries), the main motivation behind understanding the high Stokes number flows comes from the use of biomass particles as raw material in fluidized bed gasifiers. These biomass particles are often preprocessed into elongated pellets with aspect ratio ranging from 2 to 8 before being fed to gasifier. As a starting point, the shape is simplified to spherocylinders and an intermediate aspect ratio 4 is chosen for this study. However, this work can be extended to any aspect ratio mentioned above. The pellets typically have a size of a few millimeters and are processed in the fluidized bed gasifier with an upward flow of gas. This combination of large particle size and low viscosity gas results in high Stokes numbers. More generally, fluidized beds containing high inertia particles are used in a variety of chemical, pharmaceutical and process industries and often experience the range of Stokes and Reynolds numbers studied in this chapter. The values for the water case given in Table 5.1 are consistent with values encountered in water treatment plants. There, activated carbon particles, non-spherical in shape (often elongated) are fluidized in water. These particles have a volume equivalent diameter of a few millimeters resulting in the Stokes numbers studied in this work.

In summary, the rheology of inertial particulate flows is highly dependent on the properties of the particles (size, shape and surface properties) as well as the properties of the continuous fluid (viscosity, relative density). Understanding the interplay of inter-particle forces and coupling to the fluid is crucial for understanding the rheological behaviour of granular flows, and producing meaningful results. Most existing studies assume mono-disperse spherical particle granular systems to simplify the analysis. However, real systems nearly always differ from this ideal case, being poly-disperse or containing ellipsoids, platelets or even irregular shapes. The relatively few works on the rheology of non-spherical granular particles in the past have dealt mainly with dry frictionless elastic particles. There are very few studies available on the rheology of non-spherical and inelastic granular particle flows via CFD-DEM simulations. This chapter focuses on exploring this topic, in particular for rod-like granular particles. Not only the rheological properties of rod-like particles are investigated, but also the theories discussed above are used to understand the observed behaviour. Note that *the granular flows in the presence of fluid* hereafter is referred to as *suspensions*. The reader is advised not to confuse this with suspensions of colloids.

5.2 Model framework

The modelling done in this chapter is performed using a combined CFD-DEM method described in chapter 3. Note that in this chapter we limit ourselves to smooth particles without tangential friction. This is closest to the assumptions of (most common forms of) kinetic theory. Additionally, by reducing the number of parameters (in this case, friction) we can independently study the effect of fluid on the rod suspension. In the next chapter, we investigate the additional role of tangential friction. It must be noted that the effect of torque and lift on particles due to the fluid are neglected in this work. The lubrication force, which arises from the additional hydrodynamic pressure when the interstitial fluid is squeezed out from the space between two solid surfaces, is also not accounted for. This is acceptable for large granular particles with higher Stokes numbers. In other words, the time between particle collisions is much smaller than the time needed by fluid (air) to substantially affect (reduce) the relative approach velocities of particles. The only force acting on the particles due to the surrounding fluid medium is the drag force acting at the center of mass of each particle. Therefore, it is safe to say that the orientation of particles in the simulations are solely a result of particle-particle and particle-wall collisions.

5.3 Stress measurements

Our prime quantity of interest is the total particle stress tensor $\vec{\vec{\sigma}}_t$. Due to its dynamic nature, momentum transport can occur by simple flux of particles or by particle-particle contact. Therefore, the particle stress is a combination of two independent contributions, i.e the streaming stress tensor ($\vec{\vec{\sigma}}_s$) due to particle momentum flux and the collisional stress tensor ($\vec{\vec{\sigma}}_c$) due to particle collisions (Cleary, 2008). These stress tensors are given as follows :

$$\vec{\vec{\sigma}}_t = \vec{\vec{\sigma}}_s + \vec{\vec{\sigma}}_c \tag{5.1}$$

$$\vec{\vec{\sigma}}_s = \frac{1}{V_{cb}} \sum_i \left\langle m_i \vec{v}_i^{\prime} \vec{v}_i^{\prime} \right\rangle \tag{5.2}$$

$$\vec{\vec{\sigma}}_c = \frac{1}{V_{cb}} \sum_{i<j} \left\langle \vec{F}_{ij} \vec{r}_{ij} \right\rangle \tag{5.3}$$

where $\vec{v}_i'$ is the velocity fluctuation for particle i and $\langle \ldots \rangle$ indicates averaging over time (under steady state conditions) and over all particles located in the bulk control volume V_{cb}. The velocity fluctuation is calculated relative to the locally averaged velocity of the particles : $\vec{v}_i' = \vec{v}_i - \vec{v}_{avg}$. To avoid wall-effects, the measurements are performed in a bulk-like control volume which is one particle length away from the walls located at $z = 0$ and $z = h_d$. The granular temperature (T) is a measure for the residual kinetic energy in the system. It is calculated from the velocity fluctuation of the particles.

$$T = \frac{1}{3} \left\langle \vec{v}_x'^2 + \vec{v}_y'^2 + \vec{v}_z'^2 \right\rangle \tag{5.4}$$

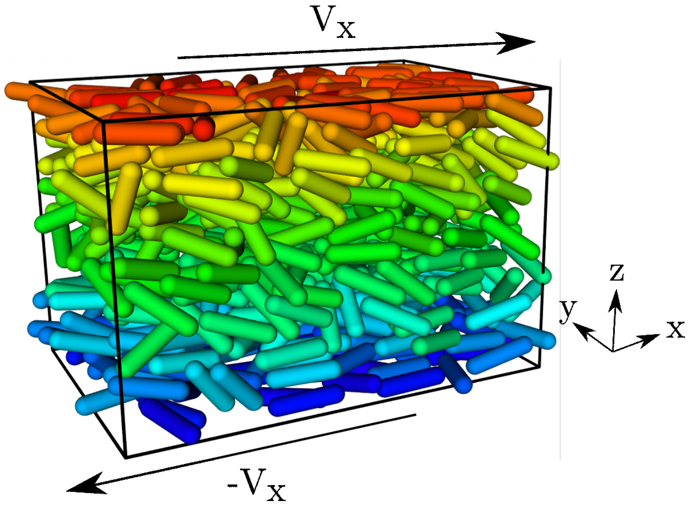

Figure 5.1: Snapshot of a CFD-DEM coupled simulation of spherocylinders. Particles are colored by their x-velocity, from blue (very negative velocity) to red (very positive velocity).

Based on the required volume fraction, a number of particles were placed inside the computational domain. Shear in the domain is achieved by moving the wall at $z = 0$ in the negative x-direction and the wall at $z = h_d$ in the positive x-direction (see Figure 5.1). The no-slip boundary conditions at the walls also drive the fluid. The boundary conditions are periodic in the x and y directions. The gravitational force acting on the system is set to zero. Note that some amount of wall-induced particle ordering occurs. This influence was found to quickly decay away from the walls. The particles used in this study are smooth (frictionless), hard (large contact stiffness), and dissipative (restitution coefficient of 0.7). Campbell (2002) identified the importance of the elastic properties of particles in determining the overall rheology of dense granular flows. He studied the effect of interparticle contact stiffness on developed stresses. The results showed that the stresses scale with the stiffness saturating at sufficiently high stiffness, indicating that the stresses are generated by the particle elasticity. Therefore, in this study, the particles are assumed to be hard with large contact stiffness, frictionless with no tangential force and partly inelastic. There is however a price to pay for simulating very large contact stiffness: the timestep necessary for accurate integration of the equations of motion becomes very small. Moreover, higher values of restitution coefficient demand even smaller timesteps, making simulations extremely expensive.

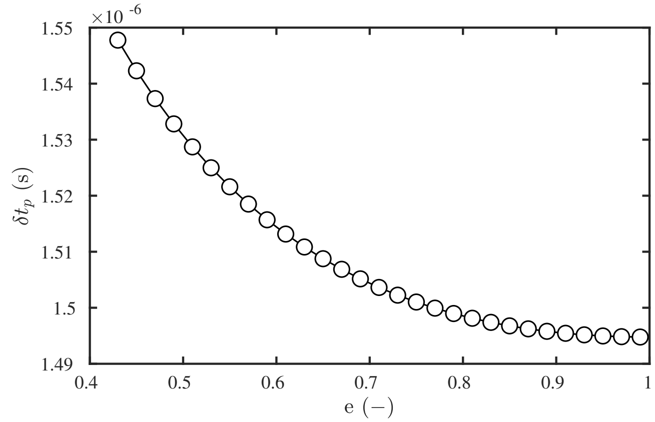

Figure 5.2: Necessary timestep δt_p for accurate integration of the equations of motion, versus coefficient of restitution e, for a stiffness value, $k_n = 6 \times 10^5$ N/m.

The simulation domain needs to be large enough to produce sufficient statistics and results which are independent of domain size, while at the same time keeping the computational cost minimal. Therefore, a comparison was done for two domain sizes: $(6,4,4) \times L_p$, and $(6,4,8) \times L_p$. The results were checked for dependence of the stress on the domain size. The two different-sized domains showed good agreement for all measured parameters: stress components, pressure and granular temperature. Therefore, the smaller domain was employed in all simulations. All simulation parameters are reported in Table 5.2.

Under a shear flow, the system achieves steady state when an equilibrium is reached between the energy supplied by the driving walls and the energy dissipated by interparticle collisions and fluid friction. For each simulation, the time required to achieve a steady state is different and is dependent on the initial configuration, volume fraction and shear rate. All quantities reported in this chapter are obtained after a steady state is achieved, typically for a shear strain of at least 10. The computing times depend pri-

Table 5.2: Simulation parameters.

Parameter		Value	Units
Particle length	L_p	12×10^{-3}	m
Particle diameter	d_p	3×10^{-3}	m
Particle density	ρ_p	1395	kg/m^3
Domain width	w_d	$6 \times L_p$	m
Domain height	h_d	$4 \times L_p$	m
Domain depth	d_d	$4 \times L_p$	m
Coefficient of friction (P-P)	μ_{pp}	0.0	-
Coefficient of rolling friction	μ_{roll}	0.0	-
Coefficient of restitution	e	0.7	-
Normal spring constant	k_n	6×10^5	N/m
Time step DEM	t_{dem}	5×10^{-7}	s
Time step CFD	t_{cfd}	5×10^{-5}	s
Air density	ρ_a	1.2	kg/m^3
Air viscosity	η_a	1.568×10^{-5}	$Pa \cdot s$
Water density	ρ_w	1000	kg/m^3
Water viscosity	η_w	1.568×10^{-3}	$Pa \cdot s$
Number of CFD cells (width)	$N_{cells,x}$	6	-
Number of CFD cells (height)	$N_{cells,z}$	4	-
Number of CFD cells (depth)	$N_{cells,y}$	4	-
Solid volume fractions	ϵ	0.1, 0.2, 0.3, 0.4, 0.5	-
No. of particles	N_p	213, 427, 640, 853, 1067	-
Shear rate	$\dot{\gamma}$	0.1-200	$1/s$

marily on the overall frequency of particle collisions which depends on volume fraction and applied shear rate. For low volume fractions and low shear rates, simulations are faster as compared to high volume fractions and high shear rates. On an average, each simulation (for each shear rate and volume fraction) took 2 days on 24 processors. The stresses and granular temperature initially increase due to initial particle collisions and then remain at a nearly constant level. Note that the steady state is independent of the initial configuration of the particles. The initial configuration only affects the shear strain within which the steady state is achieved.

Loisel et al. (2015) studied particle migration towards channel walls due to the Segré-Silberberg effect, giving rise to a non-uniform particle concentration profile in the z-direction. This phenomenon is also observed in our simulations. Therefore, the actual volume fraction is measured in the bulk region, one particle length away from the z-walls, called the measurement domain henceforth. Just like the volume fraction, the shear rate for the measurement domain is different than the apparent shear rate applied by the z-walls. The average particle velocity profile in the measurement domain was used to measure the actual shear rate. We explicitly checked and confirmed that the apparent shear rate $\dot{\gamma}$ was constant (i.e. a linear shear flow profile) across the measurement domain for all runs.

The streaming stress tensor (Eq. 5.2) can be written more explicitly as (Campbell and Gong, 1986):

$$\vec{\vec{\sigma}}_s = \rho_p \epsilon \begin{bmatrix} \left\langle \vec{v}_x^{\prime 2} \right\rangle & \left\langle \vec{v}_x^{\prime} \cdot \vec{v}_y^{\prime} \right\rangle & \left\langle \vec{v}_x^{\prime} \cdot \vec{v}_z^{\prime} \right\rangle \\ \left\langle \vec{v}_y^{\prime} \cdot \vec{v}_x^{\prime} \right\rangle & \left\langle \vec{v}_y^{\prime 2} \right\rangle & \left\langle \vec{v}_y^{\prime} \cdot \vec{v}_z^{\prime} \right\rangle \\ \left\langle \vec{v}_z^{\prime} \cdot \vec{v}_x^{\prime} \right\rangle & \left\langle \vec{v}_z^{\prime} \cdot \vec{v}_y^{\prime} \right\rangle & \left\langle \vec{v}_z^{\prime 2} \right\rangle \end{bmatrix} \tag{5.5}$$

For a sheared system as used in this study, the opposite velocities at z and $-z$ walls makes the global average velocity approximately zero. To make sure the velocity fluctuations are correctly calculated, the shear box is split into vertical bins (bins of equal height Δz). Fluctuation of the particle velocities are calculated relative to the average velocity in each bin and averaged over the measurement domain. Test simulations have been performed to find out the minimum number of bins necessary to estimate fluctuations independent of the number of bins in the domain. Based on this study, 16 bins were used to determine the granular temperature.

5.4 Model verification

In this section, the implementation of our code and stress measurements is verified by comparing shear flow simulations of smooth granular spheres against the predictions of kinetic theory. As discussed by Guo et al. (2012a) and Campbell (2002), the kinetic theory can be safely applied to dilute and moderately dense systems in which binary instantaneous collisions are dominant. However, it might fail for very dense systems where multi-particle long-lasting collisions become significant and the stresses show a dependence on the interparticle contact stiffness. For validation, our simulations are compared with kinetic theory at low volume fraction. The spherical particles have a diameter such that they have the equivalent volume as the spherocylindrical particles studied in the rest of this chapter ($d_p = 0.0053$ m).

The results are compared with the kinetic theory predictions by Lun et al. (1984). According to their theory, the steady-state shear and normal stresses for smooth, hard, and slightly dissipative spheres in the plane of shear flow is given by:

$$\sigma_{zx} = \sigma_{xz} = -\frac{5}{96} F(\epsilon, e) \rho_p (\pi T)^{0.5} d_p \dot{\gamma} \tag{5.6}$$

$$\sigma_{xx} = \sigma_{yy} = \sigma_{zz} = \rho_p T (1 + 4\alpha\epsilon g_0) \tag{5.7}$$

α is a function of the coefficient of restitution e, while g_0 is radial distribution function for spheres which depends on the solid volume fraction (ϵ) (Carnahan and Starling, 1969). The predicted steady-state granular temperature (T) is given as follows:

$$T = \frac{5\pi}{4608} \frac{F(\epsilon, e)}{\alpha (1-\alpha) \epsilon^2 g_o} d_p^2 \dot{\gamma}^2 \tag{5.8}$$

where $F(\epsilon, e)$ can be split into a collisional $F_c(\epsilon, e)$ and a streaming $F_s(\epsilon, e)$ contribution

$$F_c(\epsilon, e) = \frac{1}{\alpha (2-\alpha) g_o} \left(1 + \frac{8}{5}\alpha\epsilon g_0\right) \left[1 + \frac{8}{5}\alpha\epsilon g_0 (3\alpha - 2)\right] \tag{5.9}$$

$$F_s(\epsilon, e) = \frac{768}{25\pi} \alpha \epsilon^2 g_0 \tag{5.10}$$

The pressure in the system is a result of generated normal stresses and is measured as $1/3^{rd}$ of the trace of the total stress tensor. As can be seen in Figure 5.3, the measured granular temperature and pressure both show good agreement with the granular kinetic theory developed by Lun et al. (1984). The slight mismatch, notably the slightly lower granular temperature, can be attributed to the fact that the simulations were carried

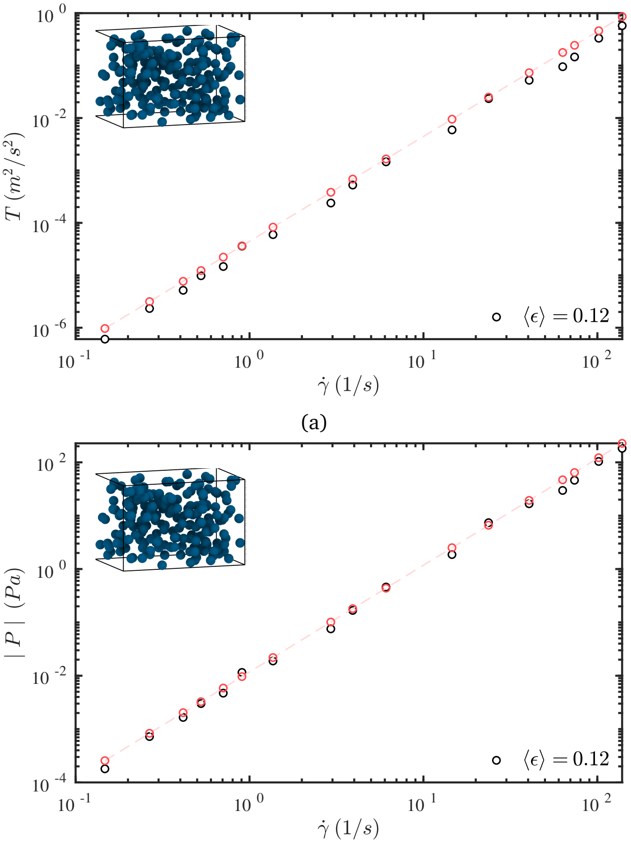

(a)

(b)

Figure 5.3: Black symbols: Particle granular temperature and pressure for dry granular shear flow of spherical particles ($e = 0.7$, $\epsilon \approx 0.12$). The red symbols indicate the predictions of kinetic theory (Lun et al., 1984).

out for particles which have somewhat dissipative collisions. As pointed out earlier, the assumption of kinetic theory is that the particle collisions are nearly elastic ($1 - e \ll 1$). The comparison for collisional and streaming stresses also show a good match with theoretical predictions, thus verifying the numerical implementation of the model and measurements.

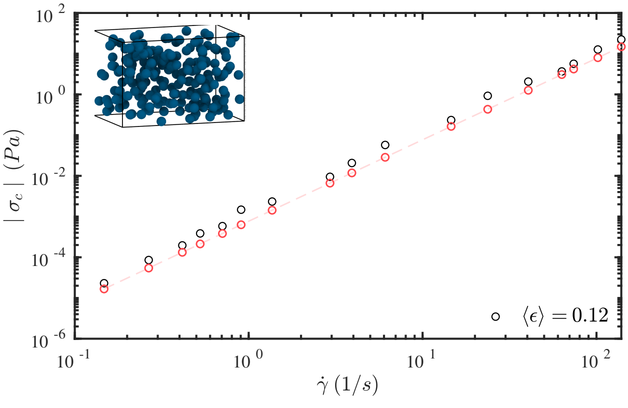

(a)

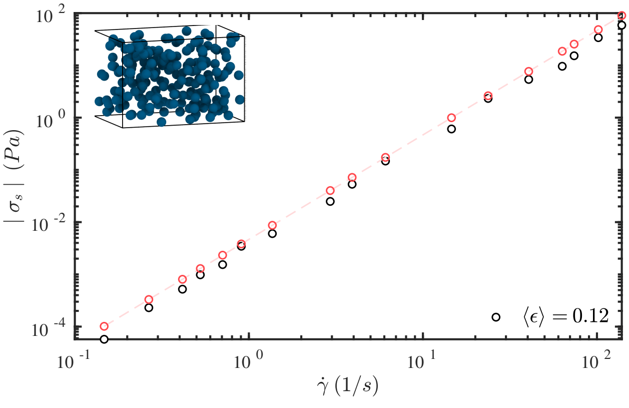

(b)

Figure 5.4: Black symbols: Particle collisional and streaming stress for dry granular shear flow of spherical particles ($e = 0.7$, $\epsilon \approx 0.12$). The red symbols indicate the predictions of kinetic theory (Lun et al., 1984).

5.5 Results and discussion

In the following sections, the behaviour of granular spherocylinder particle suspensions is investigated, looking at shear and normal stresses, pressure, granular temperature, particle orientation, apparent friction and viscosity. The results are shown for three cases: (a) dry granular shear flow (in the absence of fluid) where only particle-particle interactions shape the rheology, (b) an air suspension where elongated particles are suspended in an air-like gas and (c) water suspension where particles are suspended in a water-like fluid. For reference purpose, the predictions from granular kinetic theory (Eqs. 5.6, 5.8, 5.9 and 5.10) for volume-equivalent spheres are shown in red. Our aim by presenting these comparisons is not just to highlight the difference in the measured values against granular kinetic theory but also to highlight the similarity of the scaling with shear rate observed for rods and that predicted by kinetic theory for spheres.

5.5.1 Granular temperature and pressure

In this section, the results of granular temperature and pressure as a function of shear rate are presented for 5 volume fractions. The granular temperature is proportional to the particle fluctuating velocity squared. As the solid volume fraction increases, the collisional frequency increases, leading to more dissipation and hence lower granular temperature. This prediction is in accordance with our simulation predictions for dry granular flow (see Figure 5.5a). The granular temperatures are highest for low volume fractions since they have more space to move in between collisions. Also, the granular temperature is lower for spherocylindrical particles than for volume-equivalent spheres because their projected area in the direction of flow is smaller.

Similar behaviour is seen under the influence of air, as shown in Figure 5.6a. However, the magnitude of the granular temperature is consistently lower. Even though the particle inertia is high relative to that of air, the air still acts as a momentum sink and takes away some fluctuating energy from the particles.

Figure 5.7a shows the granular temperature under the influence of water. As expected, water strongly dampens the velocity fluctuations and therefore the resultant granular temperature. In the presence of water, the granular temperature shows the reverse behaviour as a function of solid volume fraction, when compared with the dry granular and air cases. The granular temperature is higher for higher volume fraction of the particles. Due to the higher exchange of momentum with water (as compared to the dry granular and air cases), the particles loose their fluctuating energy fast and only gain more fluctuations when they collide with other particles. In fact, when velocity fluctuations are dampened so strongly, the particles mainly collide because they are forcefully brought into contact by the shear flow. Under such conditions, a higher volume fraction leads to more frequent collisions, leading to a higher granular temperature.

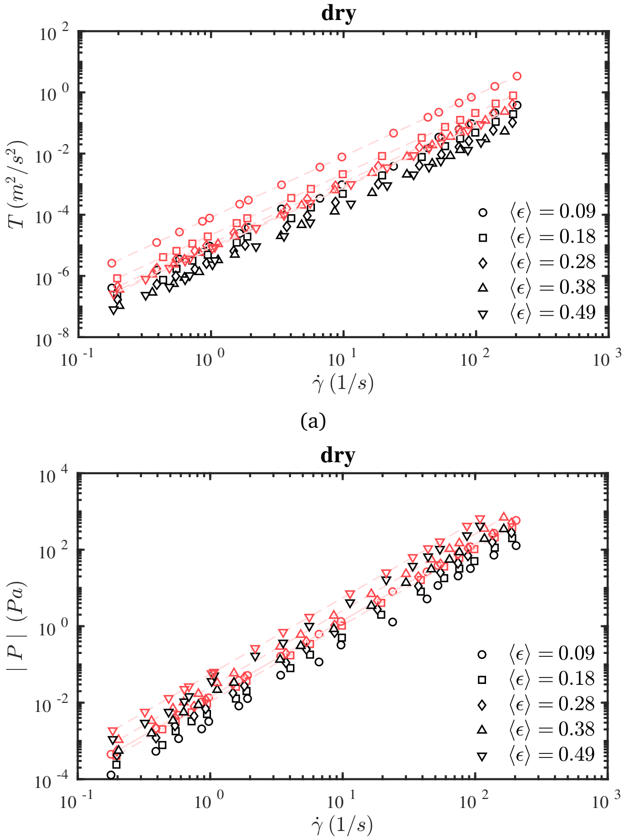

(a)

(b)

Figure 5.5: Particle granular temperature and pressure for dry granular shear flow. Black symbols: spherocylinders. Red symbols: theoretical predictions for volume equivalent spheres.

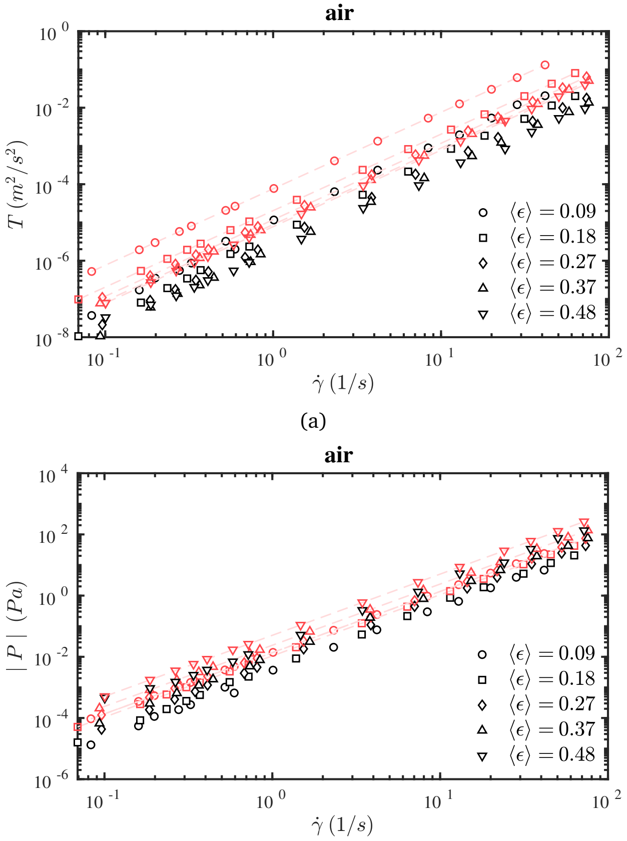

(a)

(b)

Figure 5.6: Particle granular temperature and pressure in the presence of air. Black symbols: spherocylinders. Black symbols: spherocylinders. Red symbols: theoretical predictions (without fluid effects) for volume equivalent spheres.

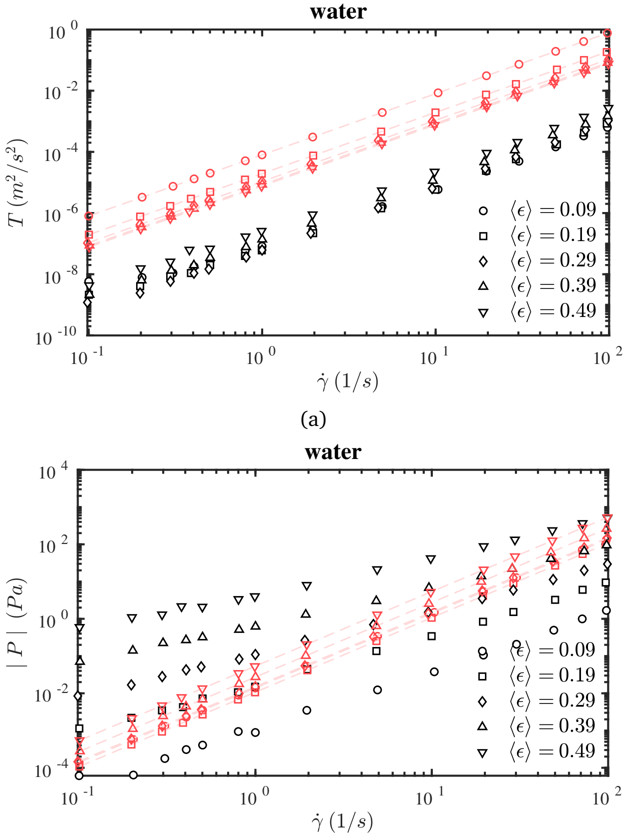

(a)

(b)

Figure 5.7: Particle granular temperature and pressure in the presense of water. Black symbols: spherocylinders. Red symbols: theoretical predictions for volume equivalent spheres.

In this study, just like the granular temperature, pressure evolves and is an emergent property of the system (at the given shear rate and solid volume fraction). The pressure shows the expected behaviour: it is increasing with the shear rate and solid volume fraction. A higher pressure at higher shear rate is a direct result of the increase in granular temperature, while a higher pressure at higher volume fraction is a direct result of more collisions per unit time. The measured pressure values are compared with the pressure predicted by kinetic theory for volume-equivalent spheres. It is found that the measured pressure for rod-like particles does not agree with kinetic theory predictions for spheres: for the dry and air cases the measured pressure is lower, while for the water case the measured pressure is lower at low volume fractions, but higher at high volume fractions. When comparing spherical and rod-like particles at volume fraction 0.1 (Figures 5.3a and 5.5a), it is clear that rod-like particles attain lower granular temperature and pressure. This effect is a result of shape of these particles and preferred alignment.

5.5.2 Collisional and streaming shear stress

Next the shear stresses for spherocylinder particles are investigated. The collisional and the streaming components of the shear stress are plotted as a function of shear rate for 5 volume fractions in Figures 5.8, 5.9 and 5.10.

Figure 5.8a shows that the kinetic theory for spherical particles agrees well with the measured collisional stress of dry spherocylinder particles at intermediate volume fractions. However, this must be a fortunate cancellation of effects, because Figure 5.5a showed that the granular temperature was underpredicted. Moreover, the deviation is large for lower and higher volume fraction. Figure 5.8b shows that the streaming stresses are lower for spherocylinder particles than predicted by kinetic theory of spherical particles. This is due to the preferential alignment of the particles, as will be shown in Section 5.5.5. The preferential alignment allows particles to avoid intense collisions. Similar behaviour was also reported by Guo et al. (2012a). When oriented in the direction of shear, the projected area of elongated particles in the direction of flow is smaller compared to volume-equivalent spherical particles. As a result, particle collisions are less probable, resulting in less fluctuations (as evidenced by the lower granular temperature in Figure 5.5a) and therefore lower stresses.

Compared to the dry granular simulations, the suspensions in a fluid medium (Figures 5.9 and 5.10) show different stress levels. A higher fluid viscosity translates to less intense collisions. Thus, the fluid medium takes away some of the fluctuating energy from the particles. The collisional stresses are slightly lower in the presence of air (Figure 5.9a) when compared to the dry granular case. However, the effect is small because

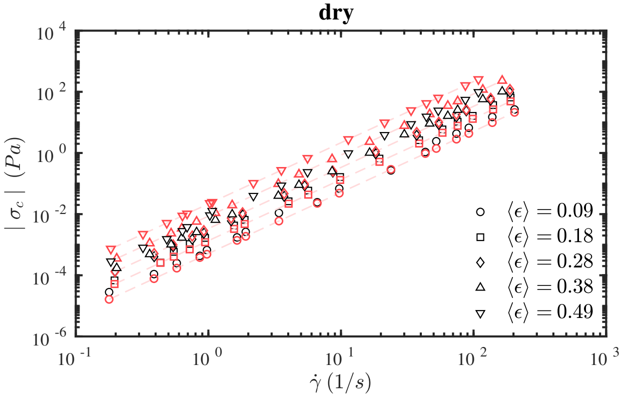

(a)

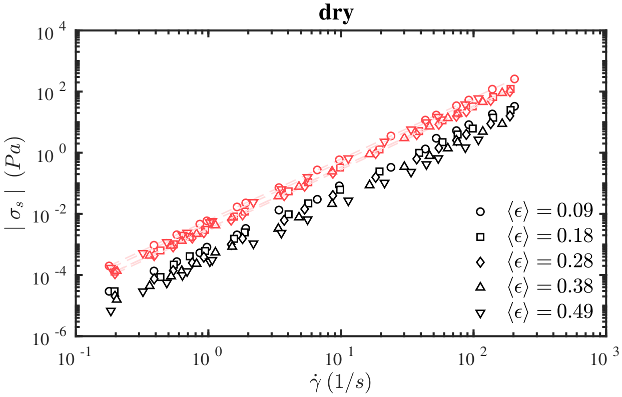

(b)

Figure 5.8: Particle collisional and streaming stress for dry granular shear flow. Black symbols: spherocylinders. Red symbols: theoretical predictions for volume equivalent spheres.

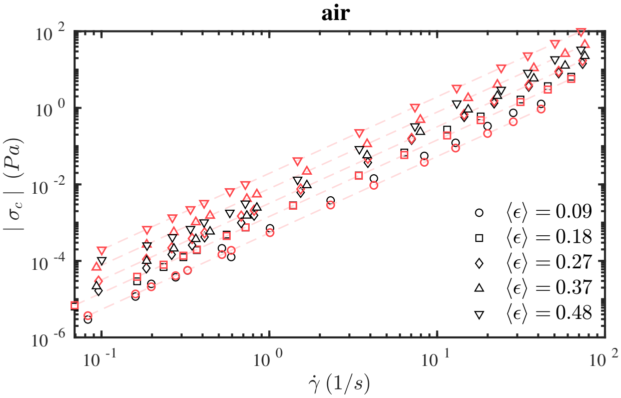

(a)

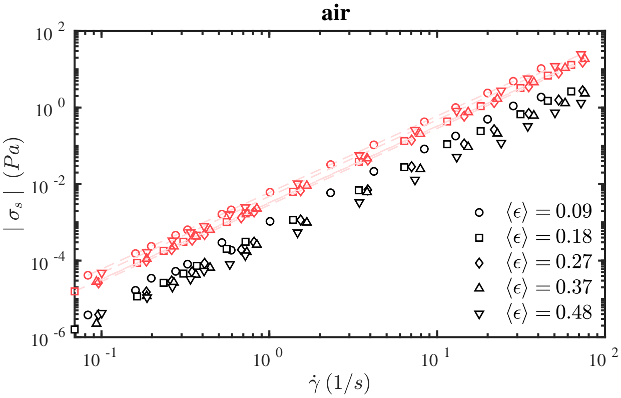

(b)

Figure 5.9: Particle collisional and streaming stress in the presence of air. Black symbols: spherocylinders. Red symbols: theoretical predictions (without fluid effects) for volume equivalent spheres.

the particles are still highly inertial. Also the streaming stresses are considerably lower in the presence of a fluid because the fluid medium reduces the velocity fluctuations and thereby acts as an additional dissipation channel.

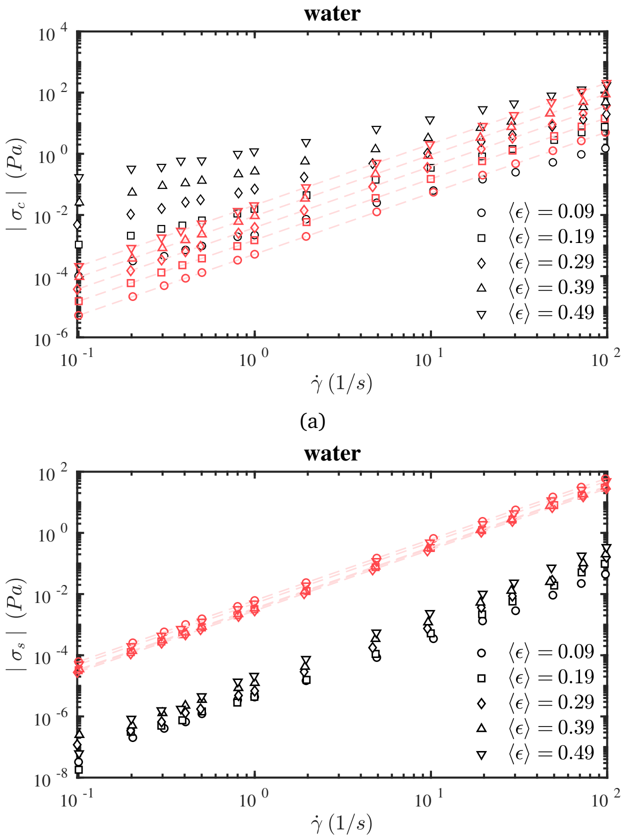

(a)

(b)

Figure 5.10: Particle collisional and streaming stress in the presence of water. Black symbols: spherocylinders. Red symbols: theoretical predictions (without fluid effects) for volume equivalent spheres.

5.5.3 Apparent friction and viscosity

The shear stress measurements can be interpreted in two different ways, either as an apparent coefficient of friction or as a quasi-Newtonian (shear rate dependent) total suspension viscosity. The apparent friction coefficient is defined as the ratio of the total particle shear stress to particle pressure ($\mu_s = |\sigma_t|/P$) where $\sigma_t = \sigma_c + \sigma_s$ is the total particle shear stress.

Figure 5.11a shows the apparent friction coefficient for dry granular shear flows at different volume fractions. Kinetic theory predicts that for spherical particles the apparent friction coefficient does not change with shear rate and has a non-monotonous dependence on volume fraction (red symbols). For spherocylinder particles, our results show that the apparent friction coefficient has a dependence on shear rate, but that this dependence is only weak, especially in view of the fact that the measured stresses and pressure vary over many orders of magnitude. Contrary to spheres, the apparent friction coefficient for spherocylinder particles displays a monotonous (and stronger) decrease with increasing volume fraction. The generally lower apparent friction coefficient for spherocylinder particles is due to the alignment of particles at higher volume fractions, leading to less resistance to the flow. Due to the absence of tangential particle-particle friction, the smooth surface allows particles to slide past each other, therefore reducing the effective (macroscopic) friction coefficient.

The fluid medium effect on the apparent friction coefficient can only be seen in the case of water (Figure 5.13a). This effect is largely caused by the wide variation in pressure with volume fraction as shown in Figure 5.7b. Comparatively, the shear stresses (Figure 5.10) do not change as much with volume fraction, resulting in considerable change in apparent friction.

The total suspension viscosity is calculated as the sum of particle viscosity and fluid viscosity:

$$\eta_s = \frac{\sigma_t}{\dot{\gamma}} + \eta_f \tag{5.11}$$

It is generally observed that non-Brownian particles suspended in a Newtonian fluid raise the viscosity of the suspension. It is also observed that such a suspension has a shear-rate dependent rheology (see e.g. Mari et al. (2014a)). The granular and air cases in Figure 5.11b and 5.12b clearly show shear thickening behaviour where the total suspension viscosity increases with increasing shear rate. This is seen for a wide range of shear rates and volume fractions. The shear thickening behaviour can be associated with the inertial nature of the particles. A number of studies have previously associated particle inertia to the existence of shear thickening behaviour in suspensions (Fall et al., 2010; Kawasaki, Ikeda, and Berthier, 2014). Particularly, for suspensions with particle Stokes number larger than 1, shear thickening due to inertia has been widely reported (Fernandez et al., 2013).

Perhaps surprisingly, for the case of water almost Newtonian behaviour is seen for

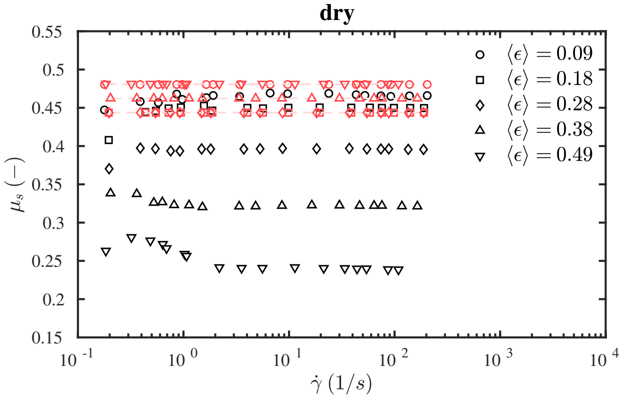

(a)

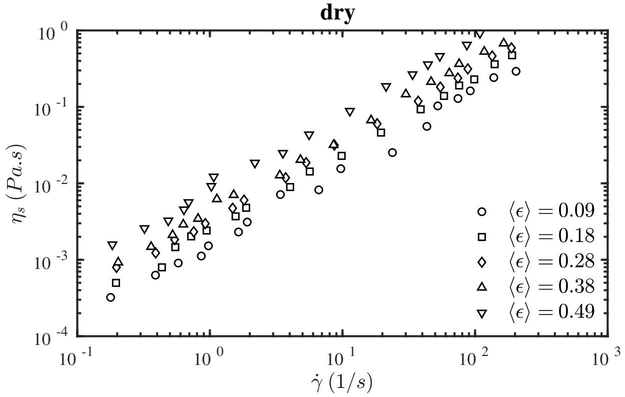

(b)

Figure 5.11: Apparent friction coefficient μ_s and total suspension viscosity η_s of the suspension for dry granular shear flow. Black symbols: spherocylinders. Red symbols: theoretical predictions for volume equivalent spheres.

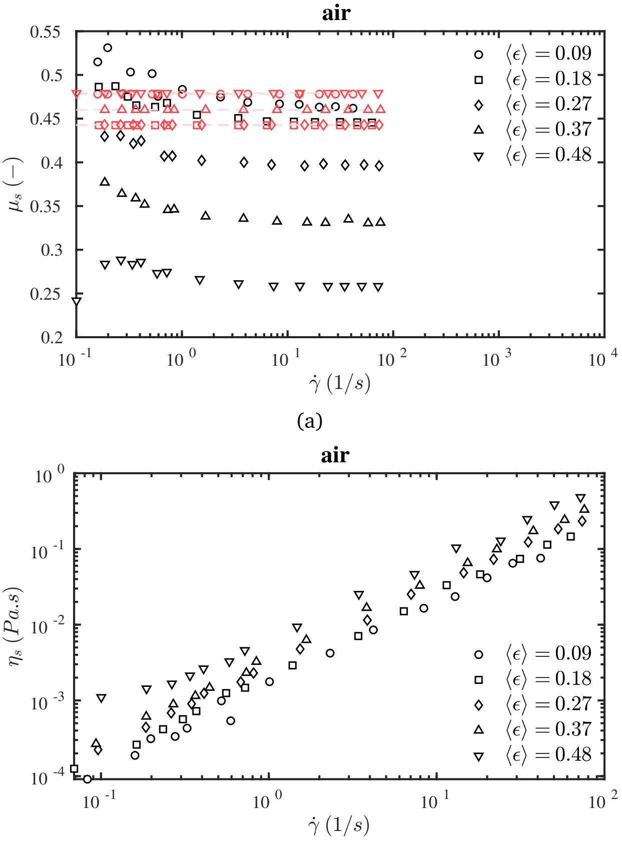

(b)

Figure 5.12: Apparent friction coefficient μ_s and total suspension viscosity η_s of the suspension in the presence of air. Black symbols: spherocylinders. Red symbols: theoretical predictions (without fluid effects) for volume equivalent spheres.

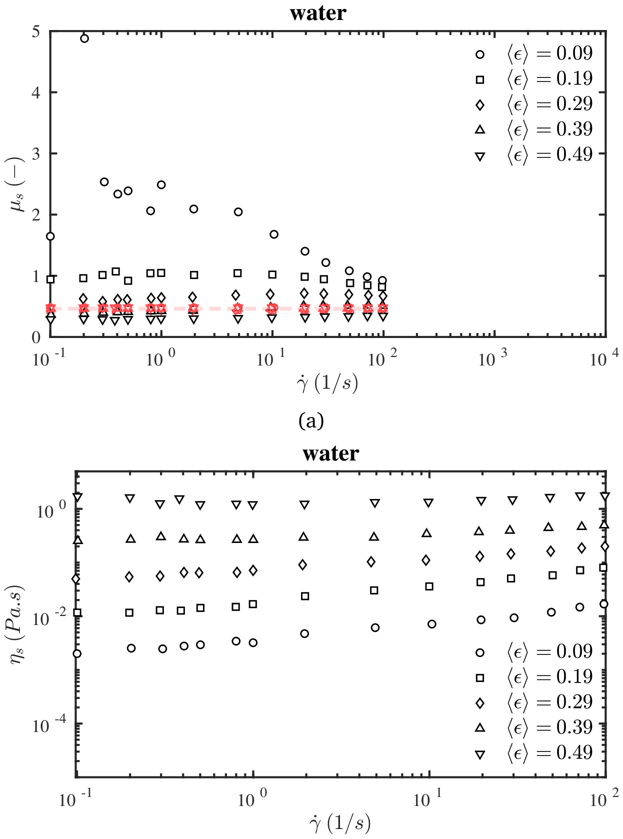

(a)

(b)

Figure 5.13: Apparent friction coefficient μ_s and total suspension viscosity η_s of suspension in the presence of water. Black symbols: spherocylinders. Red symbols: theoretical predictions (without fluid effects) for volume equivalent spheres.

high volume fractions while low volume fractions still exhibit weak shear thickening behaviour. At higher volume fraction, particles slide past each other due to preferential alignment of particles, consequently avoiding head-on types of collisions. At the same time, due to the similar densities of particles and fluid, the particles hardly affect the flow behaviour of the overall suspension. It must be noted that this behaviour is a special case and a direct result of the small density difference between fluid and particles. Another key observation here is that the viscosity is increasing with shear rate much more strongly for air than for water case. This is a direct consequence of the dominance of particle stresses shown in the previous section. The collisional particle stresses for water, shown in Figure 5.10a, vary over 3 to 4 orders of magnitude, while for air shown in Figure 5.9a, they vary over 6 orders of magnitude.

5.5.4 Normal stress

Under shear flow conditions, there are two independent normal stress differences, the so-called first and second normal stress difference. Normal stress differences are important because together with the shear stress they completely define the shear rheological behaviour of the suspension. In other words, these constitute all the rheological information that can be obtained from measuring the stress components under shear flow. Non-zero normal stress differences are generally an indicator of non-Newtonian behaviour of the suspension. For shear flow in the xz-plane (Figure 5.1), they are defined as follows:

$$N_1 = \langle \sigma_{xx} \rangle - \langle \sigma_{zz} \rangle \tag{5.12}$$

$$N_2 = \langle \sigma_{zz} \rangle - \langle \sigma_{yy} \rangle \tag{5.13}$$

Their sign and value are dependent on the particle micro-structure of the suspensions. For the case of *non-inertial* non-brownian sphere suspensions, N_2 has a negative value, and this value is increasing in the negative direction as the volume fraction of spheres increases (Zarraga, Hill, and Leighton Jr, 2000; Sierou and Brady, 2002). As for the case of N_1, there is still an intense discussion in the scientific community, especially about its sign. For example, Sierou and Brady (2002) showed that the sign of N_1 is always negative and always increases with increase of volume fraction and that hydrodynamic interactions are the main contributor to its value. Instead, Mari et al. (2014b) found that the sign of N_1 changes from negative to positive, especially at volume fractions near the maximum packing fraction. This is due to the formation of frictional contacts, and the transition from hydrodynamically dominated N_1 to frictional dominated N_1. For the case of non-spherical particles, the literature is more sparse. What is known is that for fiber and spherocylinders of sufficiently high aspect ratio, the magnitude of N_1 is greater than that of N_2. Specifically, it is predicted that $N_2 \approx -0.5N_1$. This relation is holding both for rigid fibers in the Stokes flow regime (Snook et al., 2014) and for inertial granular spherocylinders (Nagy et al., 2017), and is found to be independent of the aspect ratio upto 30 (Snook et al., 2014).

The ratio $-\frac{N_2}{N_1}$ for the three different cases of granular, air, and water is shown in Figure 5.14 for different volume fractions. For the case of pure granular flow (Figure 5.14a) our results are similar to that of Nagy et al. (2017). The main difference between Nagy et al. (2017) and our work is that for our simulations the normal stress differences have two contributions: one streaming and the other one collisional, while Nagy et al. (2017) only considered the collisional component. This shows that the requirement to get $N_2 \approx -0.5N_1$ is that the collisional stress has to be dominant. Figures 5.14b and 5.14c show that also in the presence of a fluid (air or water), the relation $N_2 \approx -0.5N_1$ still holds, which is because also under these conditions the collisional stress is the dominant one. Our results confirm that the specific relation between N_1 and N_2 holds in a regime which lies between the purely non-inertial viscous ($St \ll 1$, $Re_p \ll 1$) and purely inertial ($St \gg 1$, $Re_p \gg 1$) regimes. It will be interesting to see if the same role holds when another interparticle, force such as friction, is added.

5.5.5 Flow alignment angle

One of the well known features of granular shear flows of elongated particles is the preference in alignment with the flow direction. This alignment of the major particle axis along the flow direction allows the system to achieve a low energy state by reducing the obstruction to the flow of particles. In a non-isotropic system, like in the present study, the eigenvector belonging to the largest eigenvalue of the order tensor $\bar{\bar{S}} = \langle \vec{u}\vec{u} \rangle$ gives the preferential orientation of the particles. The angle between this eigenvector and the flow direction (x) is the flow alignment angle, which can also be expressed directly as $\vartheta = 1/2 \tan^{-1}(2S_{xz}/(S_{xx} - S_{zz}))$. Figure 5.15 shows the steady state flow alignment (also called the extinction angle) for spherocylinder particles under shear flow.

Figures 5.15a and 5.15b show that for the dry and air cases the flow alignment angle is relatively unaffected by the shear rate (within the range of shear rates studied here). The flow alignment angle decreases strongly with increasing solid volume fraction, as shown in Figure 5.15d. These observed alignment angles are in good agreement with the predictions by Nadler, Guillard, and Einav (2018). The decrease of the alignment angle with volume fraction can be explained in terms of the reduction in free volume

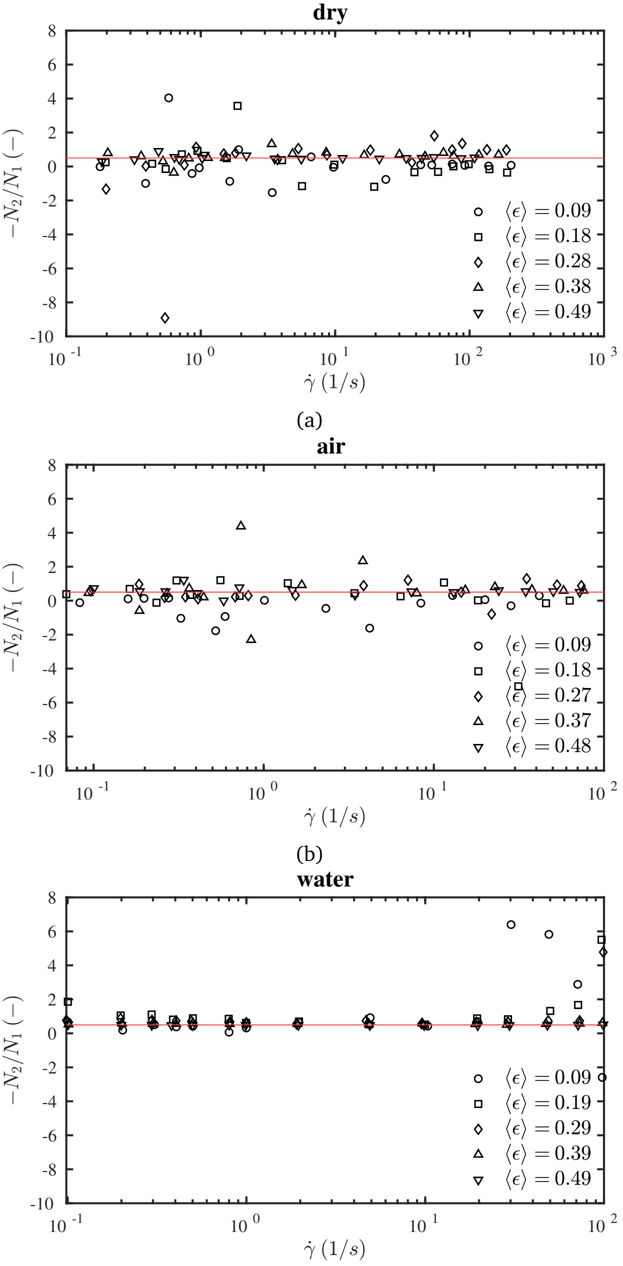

(a)

(b)

(c)

Figure 5.14: Particle normal stress ratios for (a) granular (b) air and (c) water. cases. The red line indices $N_2/N_1 = -1/2$, as observed for many other rod-like systems.

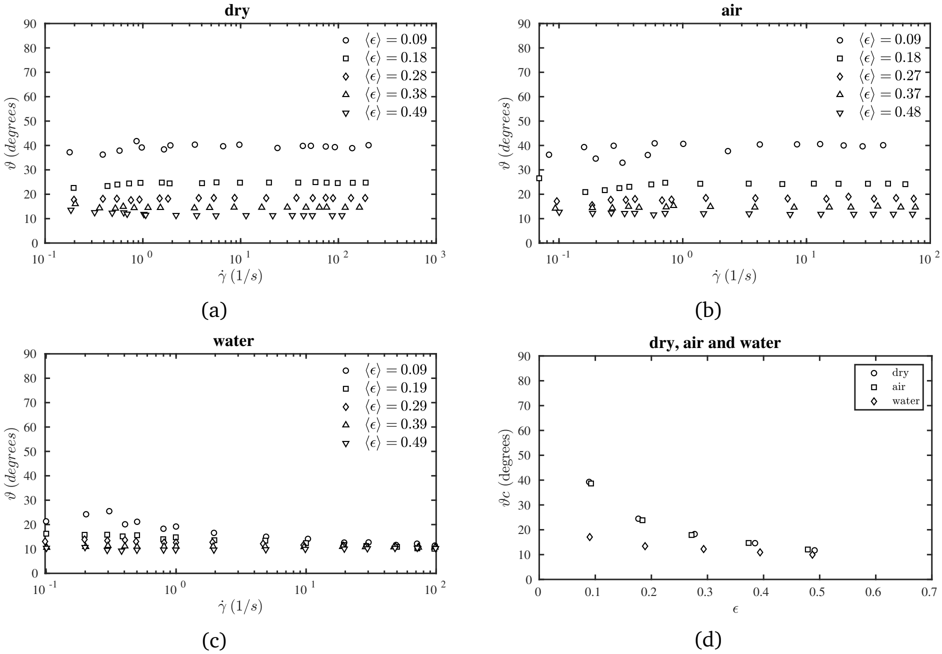

(a) (b) (c) (d)

Figure 5.15: Steady state flow alignment angle estimated from order tensor components, $\vartheta = 1/2\tan^{-1}(2S_{xz}/(S_{xx} - S_{zz}))$, versus shear rate for dry granular flow (a), in air (b), and in water (c). The limiting values at high shear rate are shown versus solid volume fraction ϵ in (d).

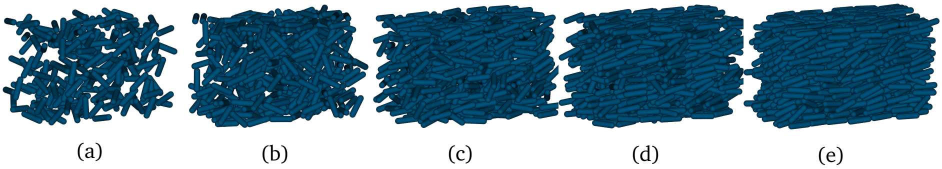

(a) (b) (c) (d) (e)

Figure 5.16: Configuration of particles at steady state for different volume fractions.

available for random reorientations, which can be appreciated from the snapshots in Figure 5.16.

Finally note that for the water case, the alignment angle is smaller than for the other 2 cases. This is a consequence of the strong damping by the fluid phase, leading to a suppression of random reorientations by fluid interactions, rather than interactions with neighbouring particles.

5.6 Conclusions and outlook

Simulations of inertial spherocylinder particles under shear flow were performed. The rheological behaviour for dry granular flow and for particles in two fluids, air and water, were studied. 3D CFD-DEM simulations were performed to measure the generated granular temperature, pressure, and stress tensor components for particles of aspect ratio 4. In this work, the effect of friction was neglected. The main contribution of this work was to demonstrate the effect of shape of the particles and fluid medium on the generated particle stresses. Compared to volume-equivalent spheres, a drastic drop in magnitudes of shear stresses for elongated particles was observed. It is evident that particle shape has an influence on the developed stresses and therefore the rheology. We demonstrated that elongated particles tend to align along the shear direction. This alignment allows the system to attain a lower energy state by avoiding intensive collisions. It was also demonstrated that the apparent (or macroscopic) friction coefficient does not change with shear rate for dry granular flows and that it decreases with increasing volume fraction.

For rod-like particles suspended in air, the results show a strikingly similar scaling as predicted by the granular kinetic theory for volume equivalent spheres, but with somewhat lower stress values. This explains the validity of previous researchers in using granular kinetic theory for simulating fluidized beds while neglecting both the effect of interstitial fluid and particle shape. Such similarity of scaling is not found for the case of water.

Note that hydrodynamic torque and lift forces were not accounted for in this chapter. While there are a few torque and lift models available in literature, the accuracy and applicability of these models to rod-like particles is questionable. We expect that for the volume fractions investigated here, the particle-particle collisional interactions are much stronger than hydrodynamic torque and lift. Additionally, once the steady state is achieved almost all particles are oriented in the direction of shear. Thus the resulting torque and lift forces are even smaller in magnitude. It should be acknowledged that these forces are probably non-negligible for the case of water. We expect a change in results for the case of water, if simulations are re-done including accurate expressions for lift and torque in multi-particle environments, when such correlations become available.

In the next chapter, we take into account the effect of particle-particle friction on the shear flow properties of granular rod-like particle suspensions. Together, these studies will help us understand the rheology of rod-like inertial particles suspension. Furthermore, they can be used to develop stress closures for use in coarse-grained models of fluidized bed biomass gasifiers, which typically contain rod-like particles.

Chapter 6

Constitutive models for collisional stress: effect of particle friction

6.1 Introduction

Granular flows are encountered in a variety of industries including agricultural, pharmaceutical, chemical, metallurgical and construction. A critical challenge is modelling these flows accurately. Industrial scale simulations of granular flows involving millions or billions of particles are possible using coarse-grained models like the two-fluid model, filtered two-fluid model and the multiphase particle-in-cell (MP-PIC) model (Yang, Padding, and Kuipers, 2016; Igci et al., 2008; Snider, 2001). These models require particle collisional stress closures to effectively account for the momentum exchange between particles. In MP-PIC and two-fluid models, the collisions are not explicitly resolved. Instead these collisions are modelled using a closure from detailed particle resolved simulations or theoretical expressions. In this chapter, a methodology for development of the required particle stress closure is demonstrated. While closures based on kinetic theory of granular flow are available, these are only well-developed for spherical particles and therefore ignore the effect of particle shape. In dense gas-solid flows, the particle-particle interactions are dominated by enduring frictional contacts as opposed to binary collisions. For instance, a packed bed of particles under the influence of gravity is known to offer resistance to change its structure, indicating the dominance of frictional contacts. Additionally, in dense regions, a single particle will make contact with multiple neighbours. This number increases as the surface area to volume ratio of the particle

---

This chapter is based on **Mahajan, V. V.**, El Hasadi Y. M. F. and Padding, J. T., *Constitutive model for inertial frictional rod-like particle flows*. Submitted.

increases. This makes it very important to study the effect of friction on the generated stresses. Kinetic theory has been extended by a number of researchers to account for inter-particle friction and pre-collisional velocity correlations, however, not directly applicable to non-spherical particles (Chialvo and Sundaresan, 2013; Yang, Padding, and Kuipers, 2016; Mitarai and Nakanishi, 2005). Therefore, there is need for accurate constitutive equations that capture the macroscopic behaviour of common granular non-spherical particles, incorporating the microscale grain-grain interaction dynamics.

The range of Stokes and Reynolds numbers of flows studied in this work are $O(10^2 - 10^5)$ and $O(10^{-1} - 10^2)$ respectively. The main motivation behind understanding the rheology for high Stokes number particle flows in the current investigation comes from the use of biomass particles as raw material in fluidized bed gasifiers. These biomass particles are often preprocessed into elongated pellets with aspect ratio ranging from 2 to 8 before being fed to gasifier (Baxter, 2005; Grammelis, 2010). As a starting point, the shape is simplified to spherocylinders and an intermediate aspect ratio 4 is chosen for this study. The pellets typically have a size of a few millimeters and are processed in the fluidized bed gasifier with an upward flow of gas. This combination of large particle size and low viscosity gas results in high Stokes numbers. More generally, fluidized beds containing high inertia particles are used in a variety of chemical, pharmaceutical and process industries and often experience the range of Stokes and Reynolds numbers studied in this chapter.

The discrete element method (DEM) developed by Cundall and Strack (1979) is used extensively for simulations of granular flows. With explicit modelling of particle-particle interaction, DEM offers the possibility to accurately study complex non-spherical interactions and poly-disperse systems (Gu et al., 2019). Considerable efforts have been made in the direction of developing continuum models based on DEM simulations of realistic particles. Campbell (2011) performed 3D simulations for ellipsoidal particles. He observed that friction forces have a stronger influence on the stresses for elongated particles than for spheres. For smooth ellipsoidal particles, smaller stresses were observed when compared to volume-equivalent spheres. Conversely, a large surface friction can lead to particle rotation which can block the flow, resulting in higher stress values than for volume-equivalent spheres. Goldshtein and Shapiro (1995) extended the granular kinetic theory for rough inelastic spherical particles. The presence of frictional forces results in energy loss due to heat and also in conversion between translational and rotational energy. Jenkins and Zhang (2002) showed that energy loss due to frictional forces can be described by means of an effective coefficient of restitution, which is a function of normal coefficient of restitution and friction coefficient: $e_{eff} = e - \frac{\pi}{2}\mu + \frac{9}{2}\mu^2$. Chialvo, Sun, and Sundaresan (2012) studied frictional particles and observed three flow regimes based on particle volume fraction and shear rate. They observed a separation of scales in the developed pressure at low scaled shear rate below a critical volume fraction (ϵ_{cr}). A number of rheological models for dense granular flows use the so-called $\mu(I)$ rheology which successfully describes dense flows and achieves a collapse of all stress measurements over a range of volume fractions and shear rates (Jop, Forterre, and Pouliquen, 2006; Da Cruz et al., 2005; Boyer, Guazzelli, and Pouliquen, 2011). This approach has shown that the constitutive equations for a complete rheological description of dense flows can be formalized in terms of the inertial number $I = \dot{\gamma} d_v \sqrt{\rho_p / P}$, where $\dot{\gamma}$ is the shear rate, P is the particle pressure, d_v is the volume equivalent diameter, and ρ_p is the density of the particles. Efforts have also been made to understand the rheology of flow of dry granular particles on an inclined planes (Hidalgo et al., 2018). However, such studies cannot be directly used in the field of fluidized beds where a wide range of volume fractions is encountered and not just the densest case. Recently, Gu et al. (2019) studied granular flow of particles belonging to the Geldart A group for a range of void fractions. They proposed closures from CFD-DEM simulations based on a study of a fluidized bed of spherical particles. The closures are obtained through simple modifications to the kinetic theory of granular materials.

As described above, considerable efforts have been made to extend the kinetic theory for smooth spheres to the dense regime. Also it has been extended to frictional spheres where the form of equations already become very complicated (Yang, Padding, and Kuipers, 2016). Guo and Curtis (2015) and Guo et al. (2013) extensively studied non-spherical particles with and without friction. They investigated the effect of a number of parameters on the flow and solid phase stresses. However, a methodology to extend kinetic theory to such particles is missing. It has not been shown in literature how kinetic theory of granular flows can be extended for frictional highly dissipative non-spherical particles, as studied in this work. In the dense regimes, friction and dissipative particle collisions dominate the rheology. A model that combines and takes advantage of the accuracy of the available theories in their respective limits needs to be developed. However, it is rather unclear as to how available theories should be combined to develop collisional stress closures for large granular particles without neglecting the effect of the surrounding fluid medium. The interactions between the particles and the interstitial fluid cannot be completely neglected, especially in the dilute regime (Guazzelli and Pouliquen, 2018; Mahajan et al., 2019). Only at high particle concentrations ($\epsilon > 0.3$), these interactions become less significant because in that case the mean time between particle collisions is much shorter than the particle-fluid relaxation time. Although in reality granular particles are usually surrounded by a fluid, the influence of the latter on the dynamic properties of the solid particles is generally neglected in most theoretical and computational works (Garzó et al., 2012). To stay close to the real application, we take into account the interstitial fluid (air).

In this chapter, CFD-DEM simulations for frictional rod-like particles under the influence of shear are performed. The particles can be characterized by the Geldart D classification. First the modelling framework and the simulation setup is described. Later the measurements are described in brief. The effect of friction on the generated particle phase stresses is demonstrated. Understanding the physics behind the rheology of such flows in detail is not our primary intention and is beyond the scope of this thesis. Rather, we focus on describing the observed rheology for use in coarse-grained models. A constitutive model is proposed for collisional interaction of solids in gas-particle flows, applicable to a wide range of solid fractions by using an interpolation of stresses in the dilute and dense regimes. In the dilute regime, the stresses generated are dominated by binary collisions and are described by functional forms based on kinetic theory of granular flow, fitted on stress measurements while taking into account the effect of fluid. In the dense regime, the generated stresses are described by functional forms based on $\mu(I)$ rheology fitted on our stress measurements.

6.2 Simulation setup

The modelling done in this chapter is performed using a combined CFD-DEM method described in chapter 3. The details about the stress measurement are described in section 5.3. The particles used in this study are hard (large contact stiffness) and dissipative (restitution coefficient of 0.43), with varying values of tangential friction. Prior to performing controlled simulations for stress measurements, typical shear rates experienced in fluidized beds need to be estimated. A full fluidized bed is simulated for a number of superficial inlet gas velocities. The gas velocity is supplied in the z-direction. The x and the y directions represent the width and depth of the bed. For more information about these simulations, the reader is referred to chapter 4. The average velocity of the particle phase in each CFD cell is calculated and then from the differences between adjacent cells the solid phase shear rate is estimated. Cells with no particles are excluded from the calculation.

Figure 6.1 shows the probability distribution function of shear rate for single gas inlet velocity. Here XZ represents shear on the x-plane in z direction. It is evident that local shear rates vary from 0 to 25/s. Although the maximum shear rate encountered in the fluidized bed is 25/s, values up to 100/s are simulated to study the rheology of these particles. The solids volume fraction in a fluidized bed varies from 0.1 to 0.5. To understand the effect of friction, simulations for three different friction coefficients are performed (see Table 6.1). Note that the restitution coefficient $e = 0.43$ and one of the friction coefficient values, $\mu_{pp} = 0.46$, have been chosen equal to the value for our

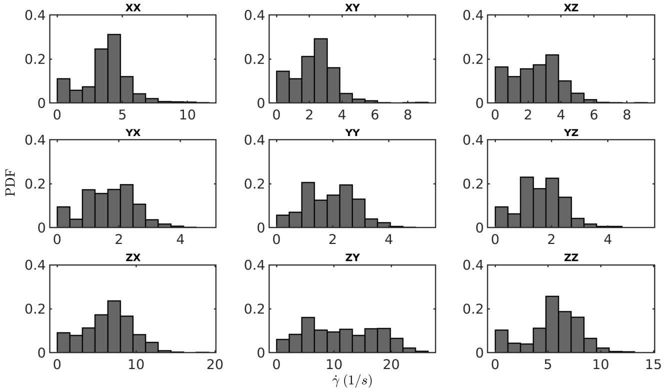

Figure 6.1: Probability distribution function (PDF) of shear rate components for fluidized bed simulation with $U_0 = 3.0$ m/s.

experimental particles (Mahajan et al., 2018b) to allow for future validation of coarse-grained simulations of fluidized beds containing these particles.

Table 6.1: Simulation parameters.

Parameter		Value	Units
Particle length	L_p	12×10^{-3}	m
Particle diameter	d_p	3×10^{-3}	m
Volume equivalent sphere diameter	d_v	5.3×10^{-3}	m
Particle density	ρ_p	1395	kg/m^3
Domain width	w_d	$6 \times L_p$	m
Domain height	h_d	$4 \times L_p$	m
Domain depth	d_d	$4 \times L_p$	m
Coefficient of friction (P-P)	μ_{pp}	0.0, 0.1, 0.46	-
Coefficient of rolling friction	μ_{roll}	0.0	-
Coefficient of restitution	e	0.43	-
Normal spring constant	k_n	6×10^5	N/m
Time step DEM	t_{dem}	5×10^{-7}	s
Time step CFD	t_{cfd}	5×10^{-5}	s
Air density	ρ_a	1.2	kg/m^3
Air viscosity	η_a	1.568×10^{-5}	Pa · s
Number of CFD cells (width)	$N_{cells,x}$	6	-
Number of CFD cells (height)	$N_{cells,z}$	4	-
Number of CFD cells (depth)	$N_{cells,y}$	4	-
Solid volume fractions	ϵ	0.1, 0.2, 0.3, 0.4, 0.5	-
No. of particles	N_p	213, 427, 640, 853, 1067	-
Shear rate	$\dot{\gamma}$	1-100	$1/s$

6.3 Results and discussion

In the following sections, we investigate the collective behaviour of spherocylinder particle suspensions by looking at shear stresses, pressure, granular temperature and particle orientation.

6.3.1 Granular temperature and pressure

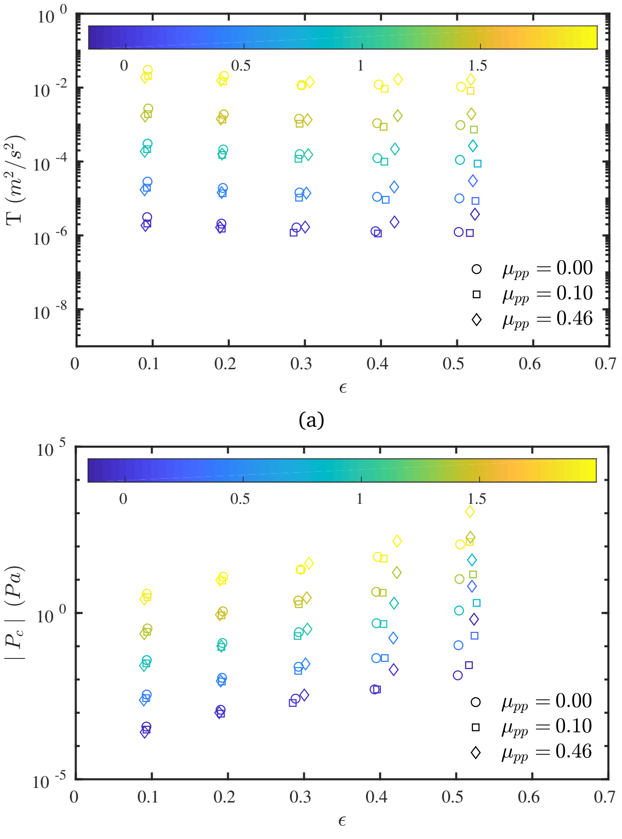

(a)

(b)

Figure 6.2: Granular temperature (a) and collisional pressure (b) as a function of solids volume fraction for different coefficient of friction values: 0.0 (circles), 0.1 (squares) and 0.46 (diamonds). The colors represent the 10-log of the applied shear rate.

Figure 6.2a shows the calculated granular temperature for different particle-particle friction coefficients. Granular temperature remains nearly the same for μ_{pp} = 0.0, 0.1

and 0.46. For $\mu_{pp} = 0.46$, granular temperature is larger at high volume fraction. This is largely because particles slide past each other at low values of friction however, at the higher value the surrounding particles are dragged along leading to higher velocity fluctuations and therefore higher granular temperature.

The pressure is given as $1/3^{rd}$ of the trace of the stress tensor. Figure 6.2b shows the collisional pressure (P_c) profile at different shear rates and volume fractions. At high volume fractions, an increase in coefficient of friction clearly shows an increase in pressure. Guo et al. (2013) studied shear flow of rod-like particles for frictional particles and observed similar behaviour.

Chialvo, Sun, and Sundaresan (2012) identified the importance of a critical volume fraction ϵ_{cr} in governing the rheology of spheres and therefore the necessity to determine it accurately for each case of μ. It has been demonstrated with experiments as well as simulations for frictionless spheres that stress data can be collapsed onto a single curve for ϵ below ϵ_{cr} upon scaling the stresses and shear rates by powers of $|\epsilon - \epsilon_{cr}|$, which is the distance to jamming (Chialvo, Sun, and Sundaresan, 2012). Based on this approach, we determine a_1, b_1 and ϵ_{cr} in Eqs. 6.1 and 6.2, for which such a collapse of data can be achieved. Figure 6.3 shows the scaled dimensionless pressure $P^* d/k_n$ versus the scaled shear rate $\dot{\gamma}^* d_v/\sqrt{k_n/(\rho_p d_v)}$ where

$$P^* = P_c/|\epsilon - \epsilon_{cr}|^{a_1} \tag{6.1}$$

$$\dot{\gamma}^* = \dot{\gamma}/|\epsilon - \epsilon_{cr}|^{b_1} \tag{6.2}$$

We found that values of the exponents $a_1 = 2/3$, $b_1 = 7/3$ are best suited for rod-like particles (for all friction values studied). The corresponding values for spherical particles are reported as $a_1 = 2/3$, $b_1 = 4/3$ (Chialvo, Sun, and Sundaresan, 2012). Clearly, a_1 and b_1 values are a function of particle aspect ratio. While the functional forms (Eqs. 6.1 and 6.2) are expected to remain the same, simulations need to be performed for other aspect ratios to determine the dependence of a_1 and b_1 on the aspect ratio. The ϵ_{cr} for frictionless rod particles was found to be 0.65. This value is in agreement with Zhao et al. (2012), who found that the maximum random packing fraction of frictionless spherocylinders of aspect ratio 4 is 0.65. For higher coefficient of friction values, as expected, the ϵ_{cr} values are lower, 0.63 and 0.59 for $\mu_{pp} = 0.1$ and 0.46, respectively. Also note that in the dilute limit the collapsed data have a slope of 2 on a double-logarithmic scale, as shown in Figure 6.3. This indicates that in this limit the pressure scales with the square of the shear rate and that the results are independent of the stiffness value (k_n), as expected for sufficiently hard particles for which kinetic theory applies.

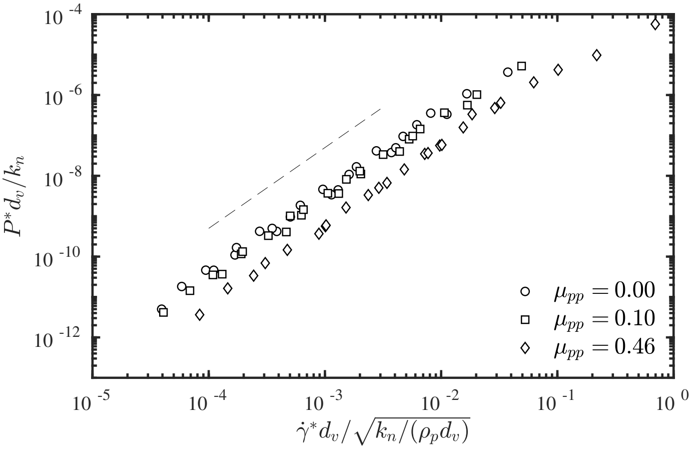

Figure 6.3: Dimensionless pressure for different coefficient of friction values: 0.0, 0.1 and 0.46. The critical volume fraction for corresponding coefficient of friction values are 0.65, 0.63 and 0.59. Dashed line indicates a slope of 2.

6.3.2 Collisional stress

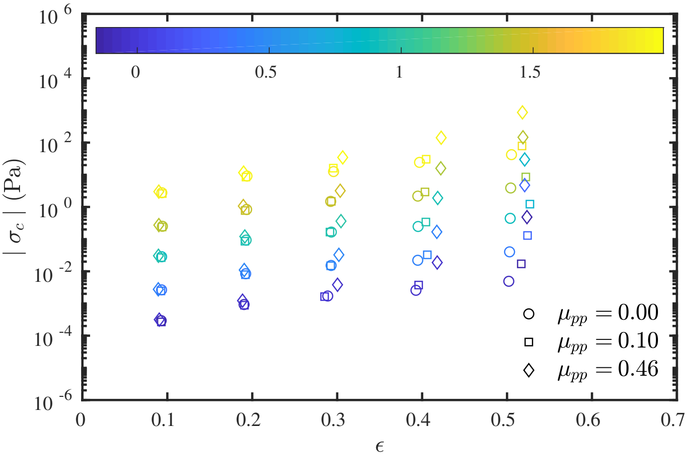

Figure 6.4: Collisional stress as a function of solids volume fraction for different coefficient of friction values: 0.0 (circles), 0.1 (squares) and 0.46 (diamonds). The colors represent the 10-log of the applied shear rate.

Figure 6.4 shows the effect of friction and volume fraction on the measured collisional stress. The magnitude of collisional stress increases as we move from low to high solid volume fraction. As expected, the magnitude of collisional stress also increases as we move from frictionless to higher coefficient of friction. At low volume fraction, the coefficient of friction does not have any effect on the magnitude of stress. However, the effect of coefficient of friction is very noticeable in the dense regime.

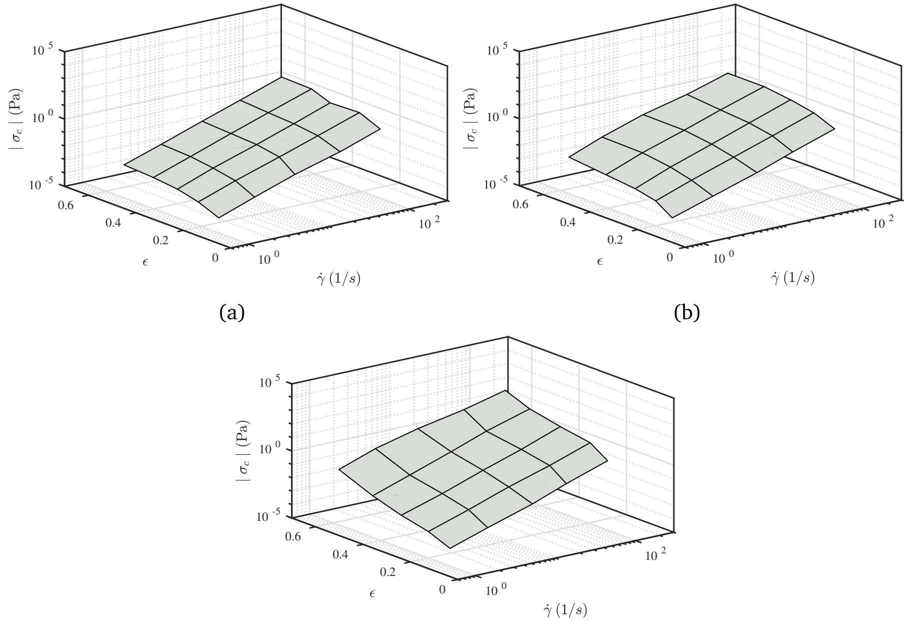

(a)

(b)

(c)

Figure 6.5: Collisional stress for different coefficient of friction values: (a) 0.0, (b) 0.1 and (c) 0.46.

Note that it was not always possible to achieve exactly the same shear rates for different values of the coefficient of friction. Therefore, Figure 6.5 shows our results in the form of 3D plots of collisional stress against shear rate and volume fraction. This is the data that we will try to capture through a constitutive equation in the next section.

6.3.3 Formulation of constitutive equations

A constitutive (rheological) model describing the pressure and stress due to collisional interaction of solids in gas-particle flow is proposed, using a simple interpolative combination of two models. For the low solid phase volume fractions, a model based on granular kinetic theory which is known to be accurate in the dilute regime is employed, while in the dense limit, $\mu(I)$ rheology which has been developed for dense granular flows is used (Jop, Forterre, and Pouliquen, 2006; Da Cruz et al., 2005).

For the sake of brevity, the constitutive model development for particles with a friction coefficient of 0.46 is demonstrated. The same approach can applied for determining constitutive laws for other friction coefficients. Additional simulations were performed to investigate the steep increase in stress in the dense regime. Mahajan et al. (2018a) previously performed experiments on particles with the same coefficient of friction. We intend to compare the predictions of MP-PIC simulations after incorporating the proposed closures with results from experiments performed for these particles (Mahajan et al., 2018b).

While developing the constitutive equations, we carefully studied several relevant independent variables for scaling in order to ensure data collapse from simulations done for a number of shear rates and volume fractions and thereby generalizing the applicability of the proposed model. The reader should note that the values of shear stress and pressure vary over several orders of magnitude for volume fractions and shear rates in this study. Fitting an equation directly on these values might result in poor fits at low volume fractions and shear rates. Fitting dimensionless and scaled quantities varying over narrower ranges helps achieving more accurate fits.

Dense regime

We start with a proposing a constitutive model for the collisional pressure. When particles are not perfectly rigid, and instead have a finite stiffness (or softness), the binary collision time is nonzero and hence presents an additional timescale, which is ignored in the standard inertial number phenomenology (Singh et al., 2015). A dimensionless number signifying the finite softness of the particles is the dimensionless pressure $P^{**} = P^* d_v / k_n$, which is needed to describe the flow behavior (Shi et al., 2017). Using the values of $\epsilon_{cr} = 0.59$, $a_1 = 2/3, b_1 = 7/3$ for Eqs. 6.1 and 6.2, it was possible to obtain a collapse of all data on to a single line as demonstrated in Figure 6.6. The best fit for dimensionless scaled pressure was found to be

$$P^{**} = \left(\frac{\dot{\gamma}^{**}}{a_2 \dot{\gamma}^{**} + b_2} \right)^2 \tag{6.3}$$

where $a_2 = 39.56$, $b_2 = 82.64$ and $\dot{\gamma}^{**} = \dot{\gamma}^* d_v / \sqrt{k_n / (\rho_p d_v)}$ is the dimensionless shear rate. Using a logarithmic scaling for $P^* d_v / k_n$, as show in Figure 6.6, we avoid fitting an equation over data which varies over many orders of magnitude as seen in Figure 6.2b and 6.3.

In Figure 6.7, we plot the stress to pressure ratio $\mu_c = \sigma_c / P_c$ against the inertial num-

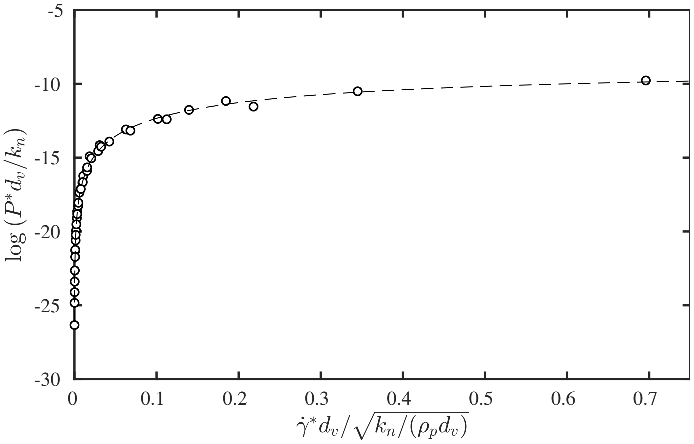

Figure 6.6: Fit for scaled pressure versus scaled shear rate for friction coefficient 0.46. The pressure is as $P^* = P_c/|\epsilon - \epsilon_{cr}|^{a_1}$ and the shear rate is as $\dot{\gamma}^* = \dot{\gamma}/|\epsilon - \epsilon_{cr}|^{b_1}$. The black circles show the data for which fit is made.

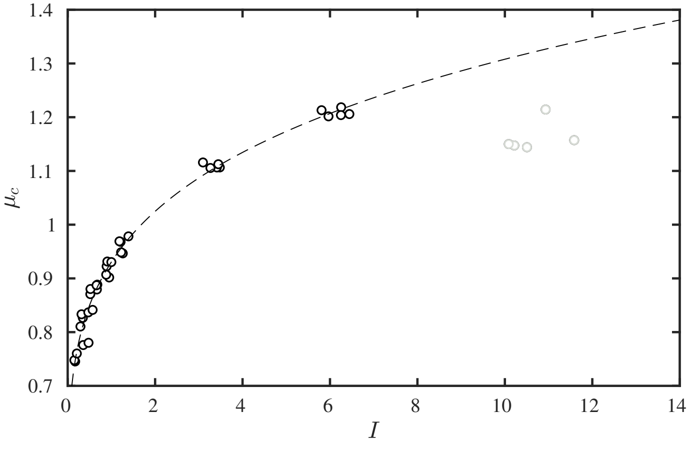

Figure 6.7: Fit for apparent friction coefficient versus inertial number for friction coefficient 0.46. The black circles show the data for which fit is made (volume fractions 0.2 and higher). The gray circles represent the data for low volume fraction 0.1, where $\mu(I)$ rheology does not apply.

ber $I = \dot{\gamma} d_v \sqrt{\rho_p / P}$. The black circles represent the data from the simulations. For low inertial numbers, which correspond to the densest systems, we see a steady increase in apparent friction with increasing inertial number. The inertial number around 6 corresponds to a volume fraction of 0.2 while the inertial number around 10 and above corresponds to a volume fraction of 0.1. For low volume fractions, the $\mu(I)$ rheology is know to deviate, as is clear from poor collapse of data at 0.1 volume fraction. We therefore fit the equation for apparent friction coefficient for inertial numbers upto 6 without much compromise in the quality of fit and ignore the gray circles representing low volume fractions. Similar to DeGiuli et al. (2015) and Nagy et al. (2017), we model this curve as

$$\mu_c = a_3 \, I^{b_3} + c_3 \tag{6.4}$$

where $a_3 = 0.57, b_3 = 0.22$ and $c_3 = 0.36$

The values of parameters are adjusted to obtain the best fit. Nagy et al. (2017) found a similar value of exponent, $b_3 = 0.4$ for 3D simulations of frictionless spherocylinders of aspect ratios ranging from 1 to 3. We do not investigate shear stress very close to the jamming packing fraction. It is important to note here that according to Eq. 6.4, at extremely low values of inertial number ($I \rightarrow 0$), μ_c tends to a value of 0.36. This is an artefact because this equation has been derived for shear flows at volume fractions sufficiently distant from the jamming fraction. It is expected that for shear flows of very dense systems (approaching the jamming fraction) the μ_c achieves an asymptotic value (Chialvo, Sun, and Sundaresan, 2012). However, its difficult to guess the value of quasi-static friction for these particles based on the results shown in Figure 6.7.

Dilute regime

We now focus on rheology in the kinetic regime (low volume fractions), which is difficult to predict with $\mu(I)$ rheology (see Figure 6.7). It is possible to obtain a collapse of data in single curve by introducing a new scaling law for low volume fractions. Figure 6.8 shows the dimensionless collisional shear viscosity versus different volume fractions. For low volume fractions, the dimensionless viscosity scales exponentially with volume fraction. Based on this scaling, we found that the shear viscosity in the low volume fraction limit can be captured well as,

$$\eta_c = a_4 \exp(b_4 \epsilon) \, \rho_s d_v \sqrt{T} \tag{6.5}$$

where exp is the exponential function, $a_4 = 0.011$ and $b_4 = 12.15$.

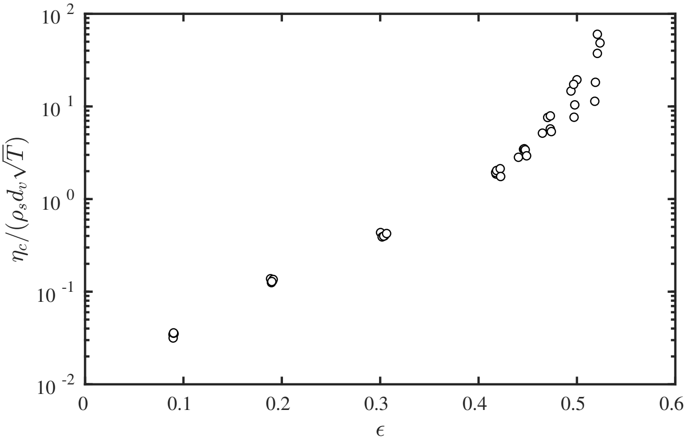

Figure 6.8: Dimensionless collisional shear viscosity versus volume fractions for friction coefficient 0.46. For volume fractions upto 0.4, the dimensionless viscosity scales exponentially with volume fraction.

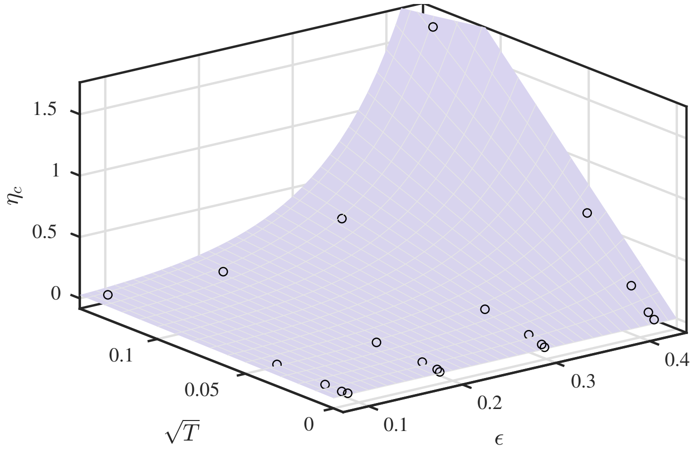

Figure 6.9: Fit for collisional viscosity versus square root of granular temperature and volume fraction for friction coefficient 0.46. The black circles show the data used for the fit.

Figure 6.9 shows the fit for collisional viscosity for the low volume fractions extending upto 0.42. For volume fractions above 0.42, the collisional stress increases steeply, making it difficult to fit all the data with a reasonably simple expression. There is a danger of over fitting when including all the data for collisional viscosity into a single fit expression. Therefore, we propose an approach of splitting the data into a dense and dilute region. Since the granular temperature measurements for elongated frictional particles are not the same as predicted by granular kinetic theory developed for spherical particles, we also propose an equation for the granular temperature in the dilute regime. A constitutive law for granular temperature can be generated by fitting the data to a polynomial quadratic in volume fraction as shown in Figure 6.10.

$$\sqrt{T} = (a_5\epsilon^2 + b_5)\dot{\gamma}\, d_v/\epsilon \tag{6.6}$$

where $a_5 = 0.624$ and $b_5 = 0.021$.

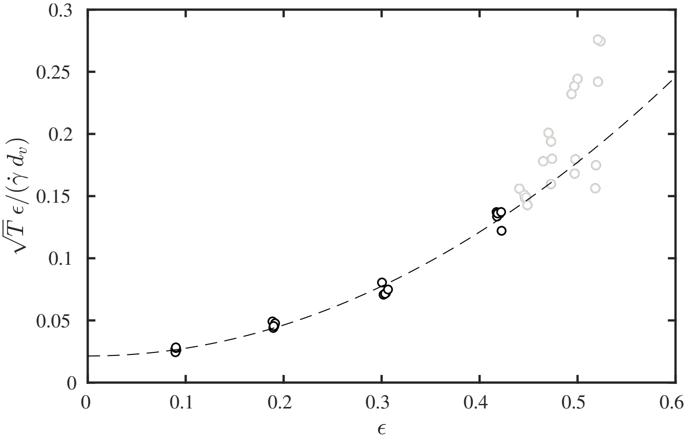

Figure 6.10: Fit for scaled dimensionless granular temperature versus volume fraction for friction coefficient 0.46. The black circles show the data for which fit is made. The gray circles represent the data for volume fraction above 0.425.

Collisional stress model

From the equations for apparent friction (Eq. 6.4) and collisional viscosity (Eq. 6.5), we can determine the collisional stress in their respective regimes as follows:

$$\sigma_{c,dilute} = \eta_c \dot{\gamma} \tag{6.7}$$

It can be seen from Eqs. 6.7, 6.5 and 6.6, that in the dilute regime this system of rod-like particles follows the so called "Bagnold scaling" which basically states that the stresses are proportional to the square of the shear rate (Bagnold, 1954). On the other hand, when the system is very dense, its response is governed by the enduring contacts among grains, which are involved in force chains.

$$\sigma_{c,dense} = \mu_c P_c \tag{6.8}$$

We bridge the two equations developed in the dense and the dilute regimes via

$$\sigma_c = S\sigma_{c,dilute} + (1-S)\,\sigma_{c,dense} \tag{6.9}$$

where S is a switch function described as follows:

$$S = 0.5\left(1 - \tanh\left(\frac{\epsilon - \epsilon_r}{\kappa}\right)\right) \tag{6.10}$$

where ϵ_r is parameter that defines the location of the switch between two regimes on the scale of volume fraction and κ determines the steepness of the switch function. For granular rods studied in this chapter, suitable values are $\epsilon_r = 0.25$ and $\kappa = 0.03$.

The switch function S ensures that the granular temperature (kinetic theory) based model has weight 1 at volume fraction 0.1 while the $\mu(I)$ rheology model completely dominates at high volume fractions. We notice that in a quite large range of volume fractions (0.2 to 0.4), both approaches apply well. Its not surprising that there is a large overlap between the two approaches, as pointed out by Berzi and Vescovi (2015). Figure 6.11 shows the predictions of the Eq. 6.9 against the measured values. The lines represent the prediction from the proposed constitutive equations plotted for eight averaged volume fractions along with 0.54 and 0.55 (top two lines). It can be seen that the predictions from the proposed correlations are in good agreement with the measured values from CFD-DEM simulations. The predictions for 0.54 and 0.55 volume fractions approaching critical volume fraction shows the behaviour of the closure outside the limits studied in this work.

Particle alignment

Granular elongated particles are known to display preference in alignment with the shear flow direction. This alignment of the major particle axis along the flow direction allows the system to achieve a low energy state by reducing the obstruction to the flow of particles. In a non-isotropic system of elongated particles, like in the present study, the eigenvector belonging to the largest eigenvalue of the nematic order tensor $S_{\alpha\beta} = \left\langle u_\alpha u_\beta \right\rangle$ gives the preferential orientation of the particles. The angle between this

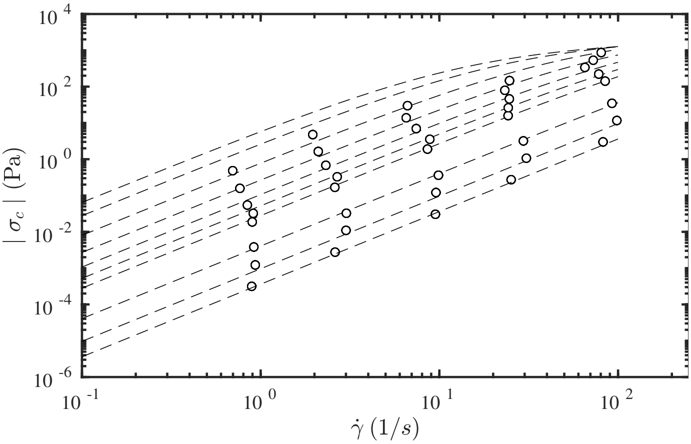

Figure 6.11: Collisional stress predicted by Eq. 6.9 for different volume fractions (ϵ = 0.09, 0.19, 0.3, 0.42, 0.45, 0.47, 0.5, 0.52, increasing from bottom to top) and friction coefficient 0.46. The circles represent the data measured from the simulations. The dashed lines represent the predictions from the proposed closures for different volume fractions. The two topmost lines show the predicted stress for volume fractions 0.54 and 0.55, showing the model constitutive behaviour outside the limits investigated in this work.

eigenvector and the flow direction (x) is the flow alignment angle, which for our setup is given by: $\vartheta = 1/2\tan^{-1}(2S_{xz}/(S_{xx}-S_{zz}))$.

Figures 6.12a, 6.12b and 6.12c show the steady state flow alignment for coefficient of friction values of 0.0, 0.1 and 0.46. These observed alignment angles are in good agreement with the predictions by Nadler, Guillard, and Einav (2018) and Börzsönyi et al. (2012).

The reader may have noticed that the orientation of particles did not play an explicit role in determining the closure for these particles. In other words, the constitutive equations are not a function of particle orientation. While at first thought, this may appear wrong, it is due to the strong preferential alignment of these particles. Irrespective of the average orientation of the particles, at a given friction coefficient, volume fraction and shear rate, we see a collapse of the data (as shown in Figures 6.6 and 6.9).

As can be seen in Figure 6.12, at steady state, the particles have an almost similar alignment angle between 10 and 30 degrees, irrespective of the applied shear rate. Because of the similar strong alignment of the elongated particles, the steady state shear stress is no longer an explicit function of the particle alignment. Note that for transient states (e.g. during the transition from the initial to the steady state), the particles are not so well-aligned, and the shear stress will depend explicitly on the order tensor. A constitutive model for the shear stress would then require the formulation of a separate

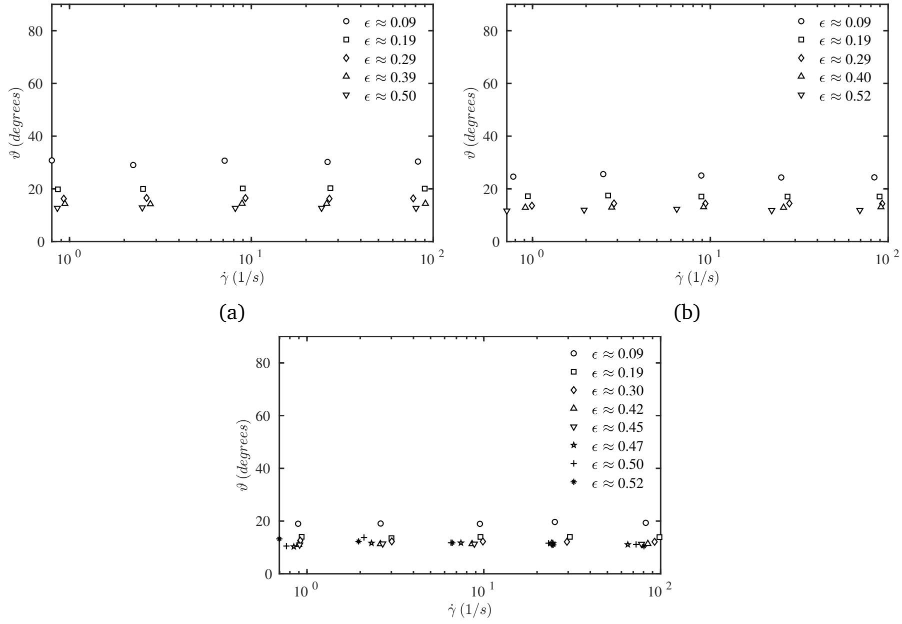

(a)

(b)

(c)

Figure 6.12: Particle orientation for different coefficient of friction values: (a) 0.0, (b) 0.1 and (c) 0.46.

(constitutive or evolution) equation describing how the order tensor depends on the applied shear rate (Nadler, Guillard, and Einav, 2018). This goes beyond the goal of this work, but will be an interesting avenue to explore in future work.

6.4 Conclusions and outlook

In this chapter, we performed simulations for of steady shear of granular frictional rod-like particles. We studied the rheological behaviour for rods under the influence of air for different friction coefficients. We performed 3D CFD-DEM simulations to measure the generated stress tensor for particles of aspect ratio 4. In chapter 5, we have demonstrated the validity of our approach by showing the consistency with kinetic theory of granular flows analytically derived for sheared flows of spherical particles at low volume fractions (Mahajan et al., 2019). We demonstrate the significant effect of friction of the particles on the generated particle stresses. As previously demonstrated, elongated particles tend to orient along the shear direction. This orientation allows the system to attain a low energy state by avoiding intense collisions.

The main contribution of this work is in a novel closure for collisional pressure and collisional shear stress for rods. More generally, we have presented a methodology to develop constitutive equations for non-spherical particles of a specific shape under the effect of fluid for which a modification of kinetic granular theory is not the correct way to proceed or very difficult to solve. We demonstrate that the functional forms, as used for the spherical particles can be extended to elongated particles of any aspect ratio.

The effect of drag model on the results presented in this chapter needs to be explored further. However, Gu et al. (2019) demonstrated that changing the drag law does not have any effect on generated particle phase stresses in systems with highly inertial particles. Simply put, when considering the particle-particle interaction, as is the case for determining the pressure and stress, the fluid drag only acts as an energy source and sink and thereby sustaining the fluctuating motion of particles.

It has to be noted that the results presented in this work are strongly affected by the tendency of the rods to orient in the direction of shear. A combination of transient shear flow simulations along with transient extensional flow and homogeneous cooling system simulations can provide a foundation of results which are more explicitly dependent on the amount of mutual particle orientation. Thus the most accurate form of stress closure for elongated particles should be a function of local order tensor along with local particle volume fraction and shear rate. Furthermore, the effect of walls on the generated stresses, granular temperature and pressure should also be investigated for further improvement in the direction of simulating fluidized bed accurately with the coarse-grained models.

The current status of multi-phase particle-in-cell (MP-PIC) type models is that they are fast and they work but there is a question on the accuracy of their predictions. These predictions depend largely on the developed collisional pressure and stress correlations. With this work, we take an important first step in this direction. While this work is done specifically for particles of aspect ratio 4, the same approach can be extended to develop stress closures for other aspect ratios. These pressure and stress closures can be used in coarse-grained modelling of fluidized bed gasifiers which typically contain rod-like particles. With this approach the coarse Euler-Lagrangian methods can avoid kinetic-theoretical approximations for the solid stress, but rather use correlations obtained from more detailed discrete particle simulations specific to the shape and micro-mechanical properties of the respective particles.

Chapter 7

Conclusion and outlook

The work in this thesis has been presented in three main topics, namely the lab-scale experiments of rod-like particles in pseudo-2D fluidized bed, the development and validation of a CFD-DEM model for dealing with fluidization of these particles, and lastly using the model to understand the rheology of these particles to develop constitutive equations. This work first aims towards gaining better insights into the hydrodynamics and behaviour of fluidized beds containing elongated particles by using experiments and numerical simulations. Later the study aims to demonstrate a methodology for multi-scale modelling by developing pressure and stress closures based on CFD-DEM simulations. With such closures, the CFD-CPM (Computational Fluid Dynamics - Collision Particle Model) can skip the expensive step of resolving the particle-particle collisions and thus can be scaled to simulations of industrial scale reactors. Figure 7.1 shows the flowchart of research road-map followed in this work. The main conclusions and recommendations based on the work in this thesis are given below.

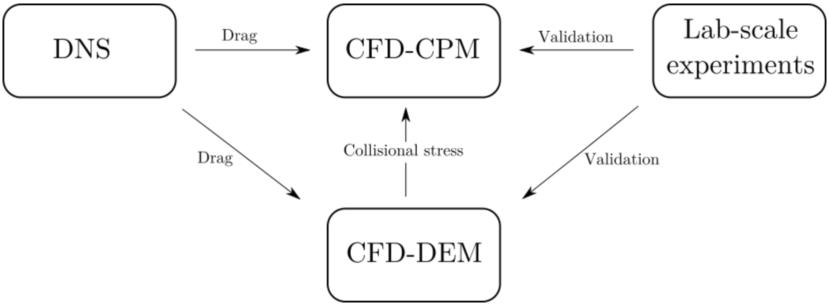

Figure 7.1: The research road-map followed in this thesis.

In chapter 2, we experimentally studied the fluidized bed of rod-like particles on a lab scale. Pressure drop and bed height measurements in two different sized set-ups for elongated particles have shown that, based on gas velocity, different regimes can be defined: packed bed, channelling and bubbling fluidization regime. Even at the highest flow rates, particles show interlocking behaviour, moving in large packed groups. It was demonstrated with experiments of two different sizes of rod-like particles and spherical particles that the behaviour described above is entirely an effect of particle shape, rather than particle size or material. It was shown with Digital Image Analysis that at low gas velocity, particles prefer to lie down horizontally, while at high flow rate the particles align themselves along the flow direction. A spatial autocorrelation analysis showed that the orientation correlation length was shown to be in the order of 3-5 particle lengths. Particle Image Velocimetry (PIV) has been applied to study the solid phase velocity and mass flux in the bed. A void fraction calculation algorithm based on CFD-DEM simulation data is used to obtain 3D void fractions. At sufficiently high flow rates, a circulation pattern similar to what is commonly observed for spherical particles is found. By analysing the number of nearest neighbours (coordination number) for each particle via Particle Tracking Velocimetry (PTV), it was shown that particles tend to move up slowly in densely packed groups and rain down faster in dilute regions.

Results on particle orientation and co-ordination numbers from this experimental study can have significant implications for both particle-scale and laboratory-scale numerical studies. Experiments can be used to dictate the choice of particle arrangements to ensure that simulations consider arrangements that are representative of real fluidized systems. Further experiments can be performed to measure rotational velocities of the non-spherical particles with the help of techniques like magnetic particle tracking.

In biomass gasifiers, to improve fluidization, a second solid material, typically an inert material like silica sand, alumina or calcite, may be used to facilitate fluidization of the biomass particles. The current study can be extended in this direction to different proportions of a mixture of inert material and non-spherical particles. This can be further extended to particles of different aspect ratio.

In chapter 4, we validated predictions of the numerical model with the experimental measurements. The comparison of experimental and numerical pressure drop and bed height results show good qualitative agreement. However, when compared quantitatively, the results show that the particle drag force is not correctly predicted. For more accurate results (also in the channelling regime), a multi-particle drag closure is needed. This drag closure should be derived from direct numerical simulations of same particle shape and size, in this case, we chose spherocylinder particles of aspect ratio 4 (Sanjeevi, Kuipers, and Padding, 2018). More importantly, such simulations should consider voidage, relative particle spacing, mutual particle orientation and particle Reynolds number as parameters.

In literature, the hydrodynamic torque is generally regarded as of very little influence, as the gas viscosity is low and the mean free path between particle collisions is very short. However, our results suggest that the incorporation of hydrodynamic torque is necessary for accurate modelling of non-spherical particles. The effects of lift forces and hydrodynamic torque are excluded in this work. The recent work by Mema et al. (2019) has shown that these forces cannot be neglected for rod-like particles. Inclusion of these additional forces should be considered for better prediction of non-spherical fluidized bed hydrodynamics. More realistic simulation of fluidized beds containing mixtures of different sized particles can be performed. The current DEM contact model for such mono-dispersed spherocylindrical particles can be extended to a mixture of poly-dispersed spherocylindrical particles. The most challenging aspect of such a simulation will be an accurate estimation of the fluid-solid interaction forces.

In chapter 5, the rheological behaviour for dry granular flow and for particles in two fluids, air and water is studied. The motivation of this work is to demonstrate the effect of shape of the particles and fluid medium on the generated particle stresses. A drastic drop in magnitudes of stresses for elongated particles compared to volume equivalent spheres is observed. Significant changes were observed in the rheological behaviour when water is used as the interstitial fluid. It is evident that shape does have an influence on the developed stresses and therefore the rheology. The elongated particles tend to orient along the shear direction. This orientation allows system to attain a low energy state by avoiding intense collisions. The macroscopic friction or the apparent friction does not change with shear rate for dry granular flows and that with increasing volume fraction, the apparent friction coefficient decreases. The validity of our approach is demonstrated by showing the consistency with kinetic theory of granular flows analytically derived for sheared flows of spherical particles at low volume fractions.

In chapter 6, simulations for steady shear of granular frictional rod-like particles are performed. The rheological behaviour for rods with different friction coefficients, while suspended in air is studied. We performed 3D CFD-DEM simulations to measure the generated stress tensor for particles of aspect ratio 4. Their is a significant effect of friction between the particles on the generated particle stresses.

We have presented a methodology to develop constitutive equations for non-spherical particles in a fluid medium for which a modification of kinetic granular theory is very difficult to solve. With this work, we take an important first step in the direction of developing accurate stress closures. The collisional pressure and collisional stress closures are essential input for coarse-grained models of fluidized bed gasifiers which typically contain rod-like particles. This work yields new insights that support a new kinetic theory for non-spherical particles.

The most accurate form of stress closure for elongated particles should be a function of the local order tensor, along with local particle volume fraction and shear rate. Furthermore, the effect of walls on the generated stresses, granular temperature and pressure should also be investigated for further improvement in the direction of simulating fluidized bed accurately with coarse-grained models.

This work can be the seed of an extended research programme, looking into momentum, mass and heat transfer in gas-solid flows of non-spherical particles and the effects of mixtures of different sized and different shaped particles.

References

Adrian, Ronald J. and Jerry Westerweel. *Particle Image Velocimetry*. 1st ed. CAMBRIDGE: Cambridge University Press, 2011. ISBN: 978-0-521-44008-0.

Allen, K G, T. W. von Backstrom, and D. G. Kroger. “Packed bed pressure drop dependence on particle shape, size distribution, packing arrangement and roughness”. In: *Powder Technology* 246 (2013), pp. 590–600.

Bagnold, Ralph Alger. “Experiments on a gravity-free dispersion of large solid spheres in a Newtonian fluid under shear”. In: *Proceedings of the Royal Society of London. Series A. Mathematical and Physical Sciences* 225.1160 (1954), pp. 49–63.

Baosheng, JIN, TAO He, and Wenqi Zhong. “Flow behaviors of non-spherical granules in rectangular hopper”. In: *Chinese Journal of Chemical Engineering* 18.6 (2010), pp. 931–939.

Baxter, Larry. “Biomass-coal co-combustion: opportunity for affordable renewable energy”. In: *Fuel* 84.10 (2005), pp. 1295–1302.

Bernard, Manuel, Eric Climent, and Anthony Wachs. “Controlling the quality of two-way Euler/Lagrange numerical modeling of bubbling and spouted fluidized beds dynamics”. In: *Industrial & Engineering Chemistry Research* 56.1 (2016), pp. 368–386.

Berzi, Diego and Dalila Vescovi. “Different singularities in the functions of extended kinetic theory at the origin of the yield stress in granular flows”. In: *Physics of fluids* 27.1 (2015), p. 013302.

Börzsönyi, Tamás et al. “Orientational order and alignment of elongated particles induced by shear”. In: *Physical review letters* 108.22 (2012), p. 228302.

Boyce, C. M. et al. “Magnetic resonance characterization of coupled gas and particle dynamics in a bubbling fluidized bed”. In: *Physical Review Fluids* 1.7 (2016), p. 074201.

Boyer, François, Élisabeth Guazzelli, and Olivier Pouliquen. “Unifying suspension and granular rheology”. In: *Physical Review Letters* 107.18 (2011), p. 188301.

Buijtenen, Maureen S. van et al. “An experimental study of the effect of collision properties on spout fluidized bed dynamics”. In: *Powder Technology* 206.1-2 (2011), pp. 139–148.

Buist, Kay A. et al. “Improved magnetic particle tracking technique in dense gas fluidized beds”. In: *AIChE Journal* 60.9 (2014), pp. 3133–3142.

Busciglio, Antonio et al. “Analysis of the bubbling behaviour of 2D gas solid fluidized beds. Part I. Digital image analysis technique”. In: *Chemical Engineering Journal* 140.1-3 (2008), pp. 398–413.

Cai, Jie, Qihe Li, and Zhulin Yuan. “Orientation of cylindrical particles in gas-solid circulating fluidized bed”. In: *Particuology* 10.1 (2012), pp. 89–96.

Campbell, Charles S. “Elastic granular flows of ellipsoidal particles”. In: *Physics of Fluids* 23.1 (2011), p. 013306.

— “Granular shear flows at the elastic limit”. In: *Journal of fluid mechanics* 465 (2002), pp. 261–291.

— “The stress tensor for simple shear flows of a granular material”. In: *Journal of Fluid Mechanics* 203 (1989), pp. 449–473.

Campbell, Charles S and Ailing Gong. “The stress tensor in a two-dimensional granular shear flow”. In: *Journal of Fluid Mechanics* 164 (1986), pp. 107–125.

Carnahan, Norman F and Kenneth E Starling. “Equation of state for nonattracting rigid spheres”. In: *The Journal of Chemical Physics* 51.2 (1969), pp. 635–636.

Chamorro, Moisés G., Francisco Vega Reyes, and Vicente Garzó. “Non-Newtonian hydrodynamics for a dilute granular suspension under uniform shear flow”. In: *Physical Review E - Statistical, Nonlinear, and Soft Matter Physics* 92.5 (2015).

Chaouki, Jamal, Faical Larachi, and Milorad P Duduković. “Noninvasive tomographic and velocimetric monitoring of multiphase flows”. In: *Industrial & engineering chemistry research* 36.11 (1997), pp. 4476–4503.

Chapman, Sydney and Thomas George Cowling. *The mathematical theory of non-uniform gases: an account of the kinetic theory of viscosity, thermal conduction and diffusion in gases*. Cambridge university press, 1970.

Cheng, Nian-Sheng. “Wall effect on pressure drop in packed beds”. In: *Powder Technology* 210.3 (2011), pp. 261–266.

Chialvo, Sebastian, Jin Sun, and Sankaran Sundaresan. “Bridging the rheology of granular flows in three regimes”. In: *Physical Review E - Statistical, Nonlinear, and Soft Matter Physics* 85.2 (2012), pp. 1–8.

Chialvo, Sebastian and Sankaran Sundaresan. “A modified kinetic theory for frictional granular flows in dense and dilute regimes”. In: *Physics of Fluids* 25.7 (2013), p. 070603.

Cleary, Paul W. “The effect of particle shape on simple shear flows”. In: *Powder Technology* 179.3 (2008), pp. 144–163.

Cleary, Paul W and Mark L Sawley. “DEM modelling of industrial granular flows: 3D case studies and the effect of particle shape on hopper discharge”. In: *Applied Mathematical Modelling* 26.2 (2002), pp. 89–111.

Constatin, Doru. *Mass moment of inertia of a spherocylinder*. 2014. URL: `blitiri.blogspot.nl` (visited on 04/05/2017).

Cundall, PA and ODL Strack. “A discrete numerical model for granular assemblies.” In: *Geotechnique* 29.1 (1979), pp. 47–65.

Da Cruz, Frédéric et al. “Rheophysics of dense granular materials: Discrete simulation of plane shear flows”. In: *Physical Review E* 72.2 (2005), p. 021309.

De Jong, J. F. et al. “Development and validation of a novel Digital Image Analysis method for fluidized bed Particle Image Velocimetry”. In: *Powder Technology* 230 (2012), pp. 193–202.

Deen, NG et al. “Review of discrete particle modeling of fluidized beds”. In: *Chemical engineering science* 62.1 (2007), pp. 28–44.

DeGiuli, E et al. “Unified theory of inertial granular flows and non-Brownian suspensions”. In: *Physical Review E* 91.6 (2015), p. 062206.

Delaney, G. W. and P. W. Cleary. “The packing properties of superellipsoids”. In: *EPL (Europhysics Letters)* 89.3 (2010), p. 34002.

Di Felice, R. “The voidage function for fluid-particle interaction systems”. In: *International Journal of Multiphase Flow* 20.I (1994), pp. 153–159.

Duda, R O and P E Hart. “Use of the {H}ough transform to detect lines and cures in pictures”. In: *Communications of the Association Computing Machinery* 15.1 (1972), pp. 11–15.

Eisfeld, B. and K. Schnitzlein. “The influence of confining walls on the pressure drop in packed beds”. In: *Chemical Engineering Science* 56.14 (2001), pp. 4321–4329.

Ergun, S. “Fluid flow through packed columns”. In: *Chem. Eng. Prog.* 48 (1952), pp. 89–94.

Ericson, Christer. *Real Time Collision Detection*. San Fransisco: Morgan Kaufmann Publishers, 2005. ISBN: 1558607323.

Escudie, R et al. “Effect of particle shape on liquid-fluidized beds of binary (and ternary) solids mixtures: segregation vs. mixing”. In: *Chemical engineering science* 61.5 (2006), pp. 1528–1539.

Fall, Abdoulaye et al. “Dry granular flows: Rheological measurements of the μ (I)-rheology”. In: *Journal of rheology* 59.4 (2015), pp. 1065–1080.

Fall, Abdoulaye et al. “Shear thickening and migration in granular suspensions”. In: *Physical review letters* 105.26 (2010), p. 268303.

Fan, Liang-Shih. “Multiphase flow and fluidization: Continuum and kinetic theory descriptions. By Dimitri Gidaspow, Academic Press, New York, 1994, 467 pp.” In: *AIChE Journal* 42.4 (1996), pp. 1197–1198.

Fernandez, Nicolas et al. “Microscopic mechanism for shear thickening of non-Brownian suspensions”. In: *Physical review letters* 111.10 (2013), p. 108301.

Forterre, Yoël and Olivier Pouliquen. “Flows of dense granular media”. In: *Annu. Rev. Fluid Mech.* 40 (2008), pp. 1–24.

Foumeny, E.A. et al. “Correlations of pressure drop in packed beds taking into account the effect of confining wall”. In: *International Journal of Heat and Mass Transfer* 36.2 (1993), pp. 536–540.

Gabitto, Jorge and Costas Tsouris. “Drag coefficient and settling velocity for particles of cylindrical shape”. In: *Powder Technology* 183.2 (2008), pp. 314–322.

Gan, Jieqing, Zongyan Zhou, and Aibing Yu. “CFD–DEM modeling of gas fluidization of fine ellipsoidal particles”. In: *AIChE Journal* 62.1 (2016), pp. 62–77.

Garzó, V and JW Dufty. “Dense fluid transport for inelastic hard spheres”. In: *Physical Review E* 59.5 (1999), p. 5895.

Garzó, V. et al. “Enskog kinetic theory for monodisperse gas-solid flows”. In: *Journal of Fluid Mechanics* 712 (2012), pp. 129–168.

Geldart, D. *Gas Fluidization Technology*. 1st. New York: John Wiley & Sons Ltd., 1986.

— “Types of gas fluidization”. In: *Powder Technology* 7.5 (1973), pp. 285–292.

Gibilaro, L G. *Fluidization-dynamics : the formulation and applications of a predictive theory for the fluidized state*. 1st ed. Oxford: Butterworth-Heinemann, 2001. ISBN: 0750650036.

Gidaspow, Dimitri. *Multiphase Flow and Fluidization: Continuum and Kinetic Theory Descriptions*. London: Academic Press Inc., 1994. ISBN: 0-12-282470-9.

Goldschmidt, M. J V, J. A M Kuipers, and W. P M Van Swaaij. “Hydrodynamic modelling of dense gas-fluidised beds using the kinetic theory of granular flow: Effect of coefficient of restitution on bed dynamics”. In: *Chemical Engineering Science* 56.2 (2001), pp. 571–578.

Goldschmidt, M. J V et al. “Digital image analysis measurements of bed expansion and segregation dynamics in dense gas-fluidised beds”. In: *Powder Technology* 138.2-3 (2003), pp. 135–159.

Goldshtein, Alexander and Michael Shapiro. “Mechanics of collisional motion of granular materials. Part 1. General hydrodynamic equations”. In: *Journal of Fluid Mechanics* 282 (1995), pp. 75–114.

Goniva, Christoph et al. “An open source CFD-DEM perspective”. In: (2010), pp. 22–24.

Goniva, Christoph et al. “Influence of rolling friction on single spout fluidized bed simulation”. In: *Particuology* 10.5 (2012), pp. 582–591.

Grammelis, Panagiotis. *Solid biofuels for energy*. Springer, 2010.

Gu, Yile et al. “Computationally generated constitutive models for particle phase rheology in gas-fluidized suspensions”. In: *Journal of Fluid Mechanics* 860 (2019), pp. 318–349.

Guazzelli, Élisabeth and Olivier Pouliquen. “Rheology of dense granular suspensions”. In: *Journal of Fluid Mechanics* 852 (Aug. 2018).

Guo, Y. et al. “A numerical study of granular shear flows of rod-like particles using the discrete element method”. In: *Journal of Fluid Mechanics* 713 (2012), pp. 1–26.

Guo, Y. et al. “Granular shear flows of flat disks and elongated rods without and with friction”. In: *Physics of Fluids* 25.6 (2013).

Guo, Yu and Jennifer Sinclair Curtis. “Discrete Element Method Simulations for Complex Granular Flows”. In: *Annual Review of Fluid Mechanics* 47.1 (2015), pp. 21–46.

Guo, Yu et al. “A numerical study of granular shear flows of rod-like particles using the discrete element method”. In: *Journal of fluid Mechanics* 713 (2012), pp. 1–26.

Hatano, Takahiro. “Power-law friction in closely packed granular materials”. In: *Physical Review E* 75.6 (2007), p. 060301.

Hidalgo, R. C. et al. “Rheological response of nonspherical granular flows down an incline”. In: *Physical Review Fluids* 7.3 (2018), pp. 1–15.

Hilton, J. E., L. R. Mason, and P. W. Cleary. “Dynamics of gas-solid fluidised beds with non-spherical particle geometry”. In: *Chemical Engineering Science* 65.5 (2010), pp. 1584–1596.

Hilton, J.E. and P.W. Cleary. “The influence of particle shape on flow modes in pneumatic conveying”. In: *Chemical Engineering Science* 66.3 (2011), pp. 231 –240.

Hölzer, Andreas and Martin Sommerfeld. “New simple correlation formula for the drag coefficient of non-spherical particles”. In: *Powder Technology* 184.3 (2008), pp. 361 –365.

Houlsby, G. T. “Potential particles: a method for modelling non-circular particles in DEM”. In: *Computers and Geotechnics* 36.6 (2009), pp. 953–959.

Howard, J.R. *Fluidized Beds Combustion and Application*. 1st. Barking, England: Applied Science Publishers LTD, 1983.

Igci, Yesim et al. “Filtered two-fluid models for fluidized gas-particle suspensions”. In: *AIChE Journal* 54.6 (2008), pp. 1431–1448.

Indiamart. *www.indiamart.com*. 2019. URL: `https://www.indiamart.com/proddetail/sawdust-biomass-pellets-17843022662.html` (visited on 03/12/2019).

Jenkins, James T. “Dense inclined flows of inelastic spheres”. In: *Granular matter* 10.1 (2007), pp. 47–52.

— “Dense shearing flows of inelastic disks”. In: *Physics of Fluids* 18.10 (2006), p. 103307.

Jenkins, James T and Diego Berzi. “Dense inclined flows of inelastic spheres: tests of an extension of kinetic theory”. In: *Granular Matter* 12.2 (2010), pp. 151–158.

Jenkins, James T and Stuart B Savage. “A theory for the rapid flow of identical, smooth, nearly elastic, spherical particles”. In: *Journal of fluid mechanics* 130 (1983), pp. 187–202.

Jenkins, James T and Chao Zhang. “Kinetic theory for identical, frictional, nearly elastic spheres”. In: *Physics of Fluids* 14.3 (2002), pp. 1228–1235.

Jin, Feng et al. “Probability-based contact algorithm for non-spherical particles in DEM”. In: *Powder Technology* 212.1 (2011), pp. 134–144.

Jong, J F De et al. “Development and validation of a novel Digital Image Analysis method for fl uidized bed Particle Image Velocimetry”. In: *Powder Technology* 230 (2012), pp. 193–202.

Jop, Pierre, Yoël Forterre, and Olivier Pouliquen. “A constitutive law for dense granular flows”. In: *Nature* 441.7094 (2006), pp. 727–730.

— “Crucial role of sidewalls in granular surface flows: consequences for the rheology”. In: *Journal of Fluid Mechanics* 541 (2005), pp. 167–192.

Kawasaki, Takeshi, Atsushi Ikeda, and Ludovic Berthier. “Thinning or thickening? Multiple rheological regimes in dense suspensions of soft particles”. In: *Epl* 107.2 (2014), pp. 1–6.

Kharaz, A. H., D. A. Gorham, and A. D. Salman. “An experimental study of the elastic rebound of spheres”. In: *Powder Technology* 120.3 (2001), pp. 281–291.

Kidokoro, Tohru, Ryohei Arai, and Masato Saeki. “Investigation of dynamics simulation of granular particles using spherocylinder model”. In: *Granular Matter* 17.6 (2015), pp. 743–751.

Kloss, Christoph et al. “Models, algorithms and validation for opensource DEM and CFD–DEM”. In: *Progress in Computational Fluid Dynamics, an International Journal* 12.2-3 (2012), pp. 140–152.

Kodam, Madhusudhan et al. “Cylindrical object contact detection for use in discrete element method simulations. Part I Contact detection algorithms”. In: *Chemical Engineering Science* 65.22 (2010), pp. 5852–5862.

Kruggel-Emden, H and K Vollmari. “Flow-regime transitions in fluidized beds of non-spherical particles”. In: *Particuology* 29 (2016), pp. 1–15.

Kruggel-Emden, H. et al. “A study on the validity of the multi-sphere Discrete Element Method”. In: *Powder Technology* 188.2 (2008), pp. 153–165.

Kumar, Rohit et al. “Influence of normal contact force model on simulations of spherocylindrical particles”. In: *AIChE Journal* 64.6 (2018), pp. 1986–2001.

Kunii, Daizo and Octave Levenspiel. *Fluidization Engineering*. Second. Butterworth-Heinemann, a division of Reed Publishing (USA) Inc., 1991, pp. xvii–xviii. ISBN: 9780080506647.

Langston, Paul A. et al. “Distinct element modelling of non-spherical frictionless particle flow”. In: *Chemical Engineering Science* 59.2 (2004), pp. 425–435.

Li, Jie and JAM Kuipers. “Gas-particle interactions in dense gas-fluidized beds”. In: *Chemical Engineering Science* 58.3-6 (2003), pp. 711–718.

Li, Jintang et al. “Flow of sphero-disc particles in rectangular hoppersa DEM and experimental comparison in 3D”. In: *Chemical Engineering Science* 59.24 (2004), pp. 5917–5929.

Li, Tingwen et al. “Numerical investigation of gas mixing in gas-solid fluidized beds”. In: *AIChE Journal* 56.9 (2010), pp. 2280–2296.

Liu, Baiqian et al. “Fluidization of non-spherical particles: Sphericity, Zingg factor and other fluidization parameters”. In: *Particuology* 6.2 (2008), pp. 125–129.

Liu, LX and JD Litster. “The effect of particle shape on the spouting properties of non-spherical particles”. In: *Powder technology* 66.1 (1991), pp. 59–67.

Liu, Shijie and Jacob H. Masliyah. “Single fluid flow in porous media”. In: *Chemical Engineering Communications* 148-150.1 (1996), pp. 653–732.

Loisel, Vincent et al. “Inertia-driven particle migration and mixing in a wall-bounded laminar suspension flow”. In: *Physics of Fluids* 27.12 (2015), p. 123304.

Lu, G., J. R. Third, and C. R. Müller. “Discrete element models for non-spherical particle systems: From theoretical developments to applications”. In: *Chemical Engineering Science* 127 (2015), pp. 425–465.

Lun, CKK et al. “Kinetic theories for granular flow: inelastic particles in Couette flow and slightly inelastic particles in a general flowfield”. In: *Journal of fluid mechanics* 140 (1984), pp. 223–256.

Ma, Huaqing, Lei Xu, and Yongzhi Zhao. “CFD-DEM simulation of fluidization of rod-like particles in a fluidized bed”. In: *Powder technology* 314 (2017), pp. 355–366.

Mahajan, Vinay V et al. “Fluid medium effect on stresses in suspensions of high-inertia rod-like particles”. In: *Chemical Engineering Science: X* 3 (2019), p. 100030.

Mahajan, Vinay V et al. “Non-spherical particles in a pseudo-2D fluidised bed: Modelling study”. In: *Chemical Engineering Science* 192 (2018), pp. 1105–1123.

Mahajan, Vinay V et al. “Nonspherical particles in a pseudo-2D fluidized bed: Experimental study”. In: *AIChE Journal* 64.5 (2018), pp. 1573–1590.

Mahmood, AA and M Elektorowicz. “A Review of Discrete Element Method Research on Particulate Systems”. In: *IOP Conference Series: Materials Science and Engineering*. Vol. 136. 1. IOP Publishing. 2016, p. 012034.

Marhadi, Kun S. and Vikram K. Kinra. “Particle impact damping: Effect of mass ratio, material, and shape”. In: *Journal of Sound and Vibration* 283.1-2 (2005), pp. 433–448.

Mari, Romain et al. “Shear thickening, frictionless and frictional rheologies in non-Brownian suspensions”. In: *Journal of Rheology* 58.6 (2014), pp. 1693–1724.

Mari, Romain et al. “Shear thickening, frictionless and frictional rheologies in non-Brownian suspensions”. In: 1693.2014 (2014). ISSN: 0148-6055. arXiv: `1403.6793`.

McLaughlin, Robert a. “Randomized Hough Transform: Improved ellipse detection with comparison”. In: *Pattern Recognition Letters* 19.3-4 (1998), pp. 299–305.

Mema, Ivan et al. “Effect of lift force and hydrodynamic torque on fluidisation of non-spherical particles”. In: *Chemical Engineering Science* 195 (2019), pp. 642–656.

Mema, Ivan et al. “Effect of lift force on dense gas-fluidized beds of non-spherical particles”. In: *12th Internatial Conference on CFD in Oil & Gas, Metallurgical and Process Industries*. 2017.

Metha, Devendra and Martin C. Hawley. “Wall effect in packed columns”. In: *Industrial & Engineering Chemistry Process Design and Development* 8.2 (1969), pp. 280–282.

MiDi, GDR. “On dense granular flows”. In: *The European Physical Journal E* 14.4 (2004), pp. 341–365.

Mitarai, Namiko and Hiizu Nakanishi. “Bagnold scaling, density plateau, and kinetic theory analysis of dense granular flow”. In: *Physical review letters* 94.12 (2005), p. 128001.

Montillet, A, E Akkari, and J Comiti. “About a correlating equation for predicting pressure drops through packed beds of spheres in a large range of Reynolds numbers”. In: *Chemical Engineering and Processing: Process Intensification* 46.4 (2007), pp. 329–333.

Nadler, B, F Guillard, and I Einav. “Kinematic model of transient shape-induced anisotropy in dense granular flow”. In: *Physical Review Letters* 120.19 (2018), p. 198003.

Nagy, Dániel B et al. “Rheology of dense granular flows for elongated particles”. In: *Physical Review E* 96.6 (2017), p. 062903.

Nan, Wenguang, Yueshe Wang, and Jianzhong Wang. “Numerical analysis on the fluidization dynamics of rodlike particles”. In: *Advanced Powder Technology* 27.5 (2016), pp. 2265–2276.

Nemec, Damjan and Janez Levec. “Flow through packed bed reactors: 1. Single-phase flow”. In: *Chemical Engineering Science* 60.24 (2005), pp. 6947–6957.

Olaofe, O. O. et al. “Improved digital image analysis technique for the evaluation of segregation in pseudo-2D beds”. In: *Powder Technology* 244 (2013), pp. 61–74.

OpenCFD. *www.OpenFoam.com*. 2004. URL: `www.openfoam.com` (visited on 03/12/2019).

Oschmann, T., J. Hold, and H. Kruggel-Emden. “Numerical investigation of mixing and orientation of non-spherical particles in a model type fluidized bed”. In: *Powder Technology* 258 (2014), pp. 304–323.

Pena, AA, R Garcia-Rojo, and Hans Jürgen Herrmann. “Influence of particle shape on sheared dense granular media”. In: *Granular matter* 9.3-4 (2007), pp. 279–291.

Podlozhnyuk, Alexander, Stefan Pirker, and Christoph Kloss. “Efficient implementation of superquadric particles in Discrete Element Method within an open-source framework”. In: *Computational Particle Mechanics* 4.1 (2017), pp. 101–118.

Pournin, L. et al. “Three-dimensional distinct element simulation of spherocylinder crystallization”. In: *Granular Matter* 7.2-3 (2005), pp. 119–126.

Radl, Stefan, Matthew Girardi, and Sankaran Sundaresan. “Effective drag law for parcel-based approaches - What can we learn from CFD-DEM?” In: *European Congress on Computational Methods in Applied Sciences and Engineering (ECCOMAS 2012)*. 2012, pp. 1225–1239. ISBN: 9783950353709.

Raichura, R. C. “Pressure Drop and Heat Transfer in Packed Beds With Small Tube-To-Particle Diameter Ratio”. In: *Experimental Heat Transfer* 12.4 (1999), pp. 309–327.

Reddy, K Anki, V Kumaran, and J Talbot. “Orientational ordering in sheared inelastic dumbbells”. In: *Physical Review E* 80.3 (2009), p. 031304.

Reddy, K Anki, J Talbot, and V Kumaran. “Dynamics of sheared inelastic dumbbells”. In: *Journal of Fluid Mechanics* 660 (2010), pp. 475–498.

Reichelt, Wolfgang. “Zur Berechnung des Druckverlustes einphasig durchströmter Kugel- und Zylinderschüttungen”. In: *Chemie Ingenieur Technik* 44.18 (1972), pp. 1068–1071.

Ren, Bing et al. “Numerical simulation of spouting of cylindroid particles in a spouted bed”. In: *Canadian Journal of Chemical Engineering* 92.5 (2014), pp. 928–934.

Reuge, N. et al. “Multifluid Eulerian modeling of dense gas-solids fluidized bed hydrodynamics: Influence of the dissipation parameters”. In: *Chemical Engineering Science* 63.22 (2008), pp. 5540–5551.

Rong, LW, KJ Dong, and AB Yu. “Lattice-Boltzmann simulation of fluid flow through packed beds of uniform spheres: Effect of porosity”. In: *Chemical Engineering Science* 99 (2013), pp. 44–58.

Sanjeevi, Sathish KP, JAM Kuipers, and Johan T Padding. “Drag, lift and torque correlations for non-spherical particles from Stokes limit to high Reynolds numbers”. In: *International Journal of Multiphase Flow* 106 (2018), pp. 325–337.

Sanjeevi, Sathish KP and Johan T Padding. “On the orientational dependence of drag experienced by spheroids”. In: *Journal of Fluid Mechanics* 820 (2017), R1.

Schwager, Thomas and Thorsten Pöschel. “Coefficient of restitution and linear-dashpot model revisited”. In: *Granular Matter* 9.6 (2007), pp. 465–469.

Shao, Yingjuan et al. “Experimental flow behaviors of irregular particles with silica sand in solid waste fluidized bed”. In: *Powder technology* 234 (2013), pp. 67–75.

Shen, Laihong, Filip Johnsson, and Bo Leckner. “Digital image analysis of hydrodynamics two-dimensional bubbling fluidized beds”. In: *Chemical Engineering Science* 59.13 (2004), pp. 2607–2617.

Shi, Hao et al. “Granular Flow: From Dilute to Jammed States”. In: *Granular Materials*. Ed. by Michael Sakellariou. Rijeka: IntechOpen, 2017. Chap. 3.

Sierou, A and JF Brady. “Rheology and microstructure in concentrated noncolloidal suspensions”. In: *Journal of Rheology* 46.5 (2002), pp. 1031–1056.

Singh, Abhinendra et al. “The role of gravity or pressure and contact stiffness in granular rheology”. In: *New journal of physics* 17.4 (2015), p. 043028.

Singh, Ranjit, R. P. Saini, and J. S. Saini. “Nusselt number and friction factor correlations for packed bed solar energy storage system having large sized elements of different shapes”. In: *Solar Energy* 80.7 (2006), pp. 760–771.

Snider, DM. “An incompressible three-dimensional multiphase particle-in-cell model for dense particle flows”. In: *Journal of computational physics* 170.2 (2001), pp. 523–549.

Snook, Braden et al. “Normal stress differences in suspensions of rigid fibres”. In: *Journal of Fluid Mechanics* 758 (2014), pp. 486–507.

Stukowski, Alexander. “Visualization and analysis of atomistic simulation data with OVI-TOthe Open Visualization Tool”. In: *Modelling Simul. Mater. Sci. Eng.* 18.1 (2009), p. 015012.

Tang, Yali et al. “A new drag correlation from fully resolved simulations of flow past monodisperse static arrays of spheres”. In: *AIChE journal* 61.2 (2015), pp. 688–698.

Tenneti, S., R. Garg, and S. Subramaniam. “Drag law for monodisperse gas-solid systems using particle-resolved direct numerical simulation of flow past fixed assemblies of spheres”. In: *International Journal of Multiphase Flow* 37.9 (2011), pp. 1072–1092.

Trnka, O et al. “Identification of the state of a fluidized bed by pressure fluctuations”. In: *AIChE journal* 46.3 (2000), pp. 509–514.

Tsuji, Y., T. Kawaguchi, and T. Tanaka. “Discrete particle simulation of two-dimensional fluidized bed”. In: *Powder Technology* 77.1 (1993), pp. 79 –87.

Vega, Carlos and Santiago Lago. “A Fast Algorithm To Evaluate the Shortest Distance Between Rods”. In: *Computers Chem* 18.1 (1994), pp. 55–59.

Versteeg, H.K: and W. Malalasekera. *An Introduction to Computational Fluid Dynamics - The Finite Volume Method*. 1995.

Vollmari, K., R. Jasevičius, and H. Kruggel-Emden. “Experimental and numerical study of fluidization and pressure drop of spherical and non-spherical particles in a model scale fluidized bed”. In: *Powder Technology* 291 (2016), pp. 506–521.

Vollmari, K et al. “Pressure drop investigations in packings of arbitrary shaped particles”. In: *Powder Technology* 271 (2015), pp. 109–124.

Wachem, B. G M van and a. E. Almstedt. “Methods for multiphase computational fluid dynamics”. In: *Chemical Engineering Journal* 96 (2003), pp. 81–98.

Wachs, Anthony et al. “Grains3D, a flexible DEM approach for particles of arbitrary convex shape Part I: Numerical model and validations”. In: *Powder Technology* 224 (2012), pp. 374–389.

Wang, Zhaolin, Mooson Kwauk, and Hongzhong Li. “Fluidization of fine particles”. In: *Chemical Engineering Science* 53.3 (1998), pp. 377–395.

Warr, Stephen, George T H Jacques, and Jonathan M. Huntley. “Tracking the translational and rotational motion of granular particles: Use of high-speed photography and image processing”. In: *Powder Technology* 81.1 (1994), pp. 41–56.

Wensrich, C M and A Katterfeld. “Rolling friction as a technique for modelling particle shape in DEM”. In: *Powder Technology* 217 (2012), pp. 409–417.

Williams, John R and Ruaidhri OConnor. “A linear complexity intersection algorithm for discrete element simulation of arbitrary geometries”. In: *Engineering computations* 12.2 (1995), pp. 185–201.

Xu, Y et al. “Detailed numerical simulation of an intruder impacting on a granular bed using a hybrid discrete particle and immersed boundary (DP-IB) method”. In: *Chemical engineering science* 104 (2013), pp. 201–207.

Yang, L Lei, JT Johan Padding, and JAM Hans Kuipers. “Modification of kinetic theory of granular flow for frictional spheres, part I: two-fluid model derivation and numerical implementation”. In: *Chemical Engineering Science* 152 (2016), pp. 767–782.

Yang, Z et al. “Improved multiple-particle tracking for studying flows in multiphase systems”. In: *AIChE journal* 53.8 (2007), pp. 1941–1951.

Ye, M., M. A. Van Der Hoef, and J. A M Kuipers. “The effects of particle and gas properties on the fluidization of Geldart a particles”. In: *Chemical Engineering Science* 60.16 (2005), pp. 4567–4580.

Zarraga, Isidro E, Davide A Hill, and David T Leighton Jr. “The characterization of the total stress of concentrated suspensions of noncolloidal spheres in Newtonian fluids”. In: *Journal of Rheology* 44.2 (2000), pp. 185–220.

Zastawny, Marian et al. “Derivation of drag and lift force and torque coefficients for non-spherical particles in flows”. In: *International Journal of Multiphase Flow* 39 (2012), pp. 227–239.

Zhao, Jian et al. “Dense random packings of spherocylinders”. In: *Soft Matter* 8.4 (2012), p. 1003.

Zhong, W.-Q. et al. “Discrete Element Method Simulation of Cylinder-Shaped Particle Flow in a Gas-Solid Fluidized Bed”. In: *Chemical Engineering & Technology* 32.3 (2009), pp. 386–391.

Zhong, Wenqi et al. “DEM/CFD-DEM modelling of non-spherical particulate systems: theoretical developments and applications”. In: *Powder Technology* 302 (2016), pp. 108–152.

Zhou, Z. Y. et al. “Discrete particle simulation of gas fluidization of ellipsoidal particles”. In: *Chemical Engineering Science* 66.23 (2011), pp. 6128–6145.

Zhou, Zong-Yan et al. “Dynamic simulation of the packing of ellipsoidal particles”. In: *Industrial & Engineering Chemistry Research* 50.16 (2011), pp. 9787–9798.

Zhu, H. P. et al. “Discrete particle simulation of particulate systems: A review of major applications and findings”. In: *Chemical Engineering Science* 63.23 (2008), pp. 5728–5770.

List of Publications

Journal Publications

Mahajan, V. V., El Hasadi Y. M. F. and Padding, J. T., *Constitutive model for inertial frictional rod-like particle flows*. Submitted.

Mahajan, V. V., Mehmood J., El Hasadi Y. M. F. and Padding, J. T., *Fluid medium effect on stresses in suspension of high-inertia rod-like particles*, Chemical Engg. Science X **3**, 100030 (2019).

Fitzgerald B. W., Zarghami A., **Mahajan, V. V.**, Sanjeevi S. K. P., Mema I., Verma V., El Hasadi Y. M. F. and Padding, J. T., *Multiscale Simulation of Elongated Particles in Fluidised Beds*, Chemical Engg. Science X **17**, 891 (2019).

Mema I., **Mahajan, V. V.**, Fitzgerald B. W. and Padding, J. T., *Effect of lift force and hydrodynamic torque on fluidisation of non-spherical particles*, Chemical Engg. Science **195**, 642-656 (2019).

Mahajan, V. V., Nijssen, T. M., Kuipers, J. A. M. and Padding, J. T., *Non-spherical particles in a pseudo-2D fluidized bed: Modelling study*, Chemical Engg. Science **192**, 1105-1123 (2018).

Mahajan, V. V., Padding, J. T., Nijssen, T. M., Buist, K. A. and Kuipers, J. A. M., *Non-spherical particles in a pseudo-2D fluidized bed: Experimental study*, AIChE Journal **64.5**, 1573-1590 (2018).

Conference Proceedings and Presentations

Mahajan, V. V., Nijssen, T. M., Fitzgerald B. W., Kuipers, J. A. M. and Padding, J. T., *Computational and experimental study of spherocylinder particles in fluidized beds*, APS Annual Meeting (DFD), Portland, USA (2016).

Mahajan, V. V., Nijssen, T. M., Fitzgerald B. W., Kuipers, J. A. M. and Padding, J. T., *Experimental study of rod-like particles in fluidized bed*, AERC, Copenhagen, Denmark (2017).

Mahajan, V. V., Nijssen, T. M., Fitzgerald B. W., Kuipers, J. A. M. and Padding, J. T., *The* *peculiar behavior of elongated particles in fluidized beds : experiments vs simulations*, CFD2017, Trondheim, Norway (2017).

Mahajan, V. V., Nijssen, T. M., Fitzgerald B. W., Kuipers, J. A. M. and Padding, J. T., *Fluidization of spherocylinder particles*, Powders and Grains, Montpellier, France (2017).

Mahajan, V. V., Nijssen, T. M., Kuipers, J. A. M. and Padding, J. T., *CFD-DEM simulations of rod-like particles in pseudo-2D fluidized beds*, CHAINS, Veldhoven, Netherlands (2017).

Mahajan, V. V., Mehmood, J., El Hasadi Y. M. F. and Padding, J. T., *Rheology of rod-like granular particle suspensions*, AERC, Sorrento, Italy (2018).

Mahajan, V. V., Mehmood, J., El Hasadi Y. M. F. and Padding, J. T., *Rheological behavior of rod-like granular particle suspensions : effect of fluid medium*, CFD2018, Melbourne, Australia (2018).

Acknowledgements

At last, to wrap up this journey as a PhD, some final words of my thesis. A lot of emotions flow through my mind as I write this. It has been a memorable, joyful and humbling experience. There were highs and there were lows. All of them taught me lessons that I shall remember forever. I have learnt to laugh at problems and to channel my energy in the right direction. I would like to thank everyone - my mentors, peers, friends and family, who have been a part of this journey, without whom this would not have been possible. Some of them I should mention explicitly.

First, I would like to thank my daily supervisor and promotor, Johan for giving me an opportunity to pursue this doctoral research. I vividly remember the day I had an informal-meeting-turned-into-interview with Johan before I embarked on this journey. The quality and speed with which he helped was always high. He gave me enough freedom to try things at my own pace. I will miss those long hours of intriguing discussions, trying to make sense out of then incomprehensible graphs and of course the excellent times we had in conferences. Johan knows everything about everything - academics, research, life, music, movies, TV shows, you name it. I find myself lucky to have had the opportunity to absorb some of it during our lunches.

I would like to thank Hans for his guidance in the first half of my PhD. I had dreamt about working with him ever since my Bachelor graduation project in India. His inputs on code development and the experiments were like that of a fortune teller. His wide academic experience saw things much in advance.

I am also very thankful to Burak, who has kindly accepted to act as my second promotor, despite the late stage of my PhD. I would like to thank Kay, for the discussions on non-spherical fluidization experiments. Ada and Leslie, thank you for handling and arranging all the formalities.

During my PhD, I supervised two students, Tim and Junaid, whom I want to thank for all the hard work. Their contributions are an important part of this thesis. I would

also like to thank Jeroen for introducing me to the ethics of coding and for helping tackle initial challenges with LIGGGHTS, CFDEM and OpenFOAM.

Aditya and Rohit have been the closest to me during these four years. I could always count on them, open up and be comfortable about discussing everything. We have laughed together at the worst jokes, travelled, cooked, played PS for countless hours, the list is endless. The memories I have with them are too many and too precious. A simple thank you won't do justice to how much I have learnt from you two.

My initial time at SMR group in Eindhoven was nothing short of a two and half year party. Be it during the work hours or outside, everyone there made sure we had fun all the time. I would like to thank all of my SMR colleagues. Satish, Vishak, Adnan, Harshil, Aniruddha, Shauvik, Saurish, many other Indian colleagues who made my stay warm with Indian food and Desi parties. Ale, Solomon, Milan, Ramon, Luuk, Lei, Alvaro together made an explosive cocktail. Special thanks to Giulia, who was like a family member away from home, always welcoming and cheerful. My thanks also extend to Maxim, Gaopan, Haryo, Sushil, Deepak, Krushna, Yali.

My time in Delft was mostly spent working unlike in Eindhoven (no sarcasm intended). I had great time with the new officemates: Vikrant, Barry, Stefan and for a brief period Ahad. I made some new lifelong friends: Rong, Elyas, Lalit. Sathish, what a guy! Delft would have been totally boring without him. Thank you for the all the craziness. Ivan, the CFD-DEM buddy, thank you for the collaboration and taking me to the great barrier reef. Yousef, want to thank you for the interesting discussions (academic and otherwise). Rumen, thank you for showing me around in Bulgaria.

I would like to thank my mentor, Dr. Vivek Ranade for his guidance during early days as a researcher at NCL, Pune. He has been a source of encouragement and inspiration ever since. Special thanks to Balkrishna, with whom I embarked on the journey in the Netherlands.

I would like to thank Shreya for standing by me through the toughest times. Thanks for patiently bearing with me and proof-reading the thesis.

At last, I would like to thank my parents for their immense love and understanding. They have sacrificed a lot so I could be where I am today. Without their support nothing of this would have been possible. I would also like to thank my sister Rasika and Mandar, for their constant words of encouragement and support.

Vinay
Delft, 2019

Curriculum Vitae

Vinay Vilas Mahajan was born on 11^{th} May, 1988 in Nagpur. He completed his schooling in Nagpur. Later, he decided to pursue B.Tech in Chemical Engineering from National Institute of Technology, Rourkela with first class distinction. During Bachelors, he did an internship at Indian Oil Corporation Ltd, Panipat refinery. From January 2011, he worked with dr. Vivek Ranade at National Chemical Laboratory, Pune where he investigated gas-disengagement phenomenon in fluidized bed.

In August 2012, Vinay moved to Netherlands to pursue Masters in Chemical Engineering with specialization in Process Engineering at Technical University Eindhoven. During an internship at Research and Development department, Tata Steel, IJmuiden he worked on ’Deadman position in Blast Furnace - cause and effect’. Vinay did his graduation project with prof. Hans Kuipers on ’Granular flow down inclined rotating chute - experimental and modelling study’.

In November 2014, Vinay began his doctoral research in Multiphase Reactor Group, Chemical Engineering and Chemistry Department at Technical University Eindhoven under the guidance of prof. Hans Kuipers and prof. Johan Padding. From July 2017, he continued his PhD at department of Process and Energy, Faculty of Mechanical, Maritime and Materials Engineering, Technical University Delft under the guidance of prof. Johan Padding. The results of his research are presented in this dissertation. After his doctoral research, Vinay started working as a computational scientist at Simreka in Utrecht, the Netherlands.